
High-redshift infrared galaxies: mid-infrared properties and evolutionary models

Elisabetta Valiante



München 2008

High-redshift infrared galaxies: mid-infrared properties and evolutionary models

Elisabetta Valiante

Dissertation
an der Fakultät für Physik
der Ludwig–Maximilians–Universität
München

vorgelegt von
Elisabetta Valiante
aus Notaresco(TE), Italien

München, den 10. September 2008

Erstgutachter: Prof. Dr. Reinhard Genzel
Zweitgutachter: Prof. Dr. Andreas M. Burkert
Tag der mündlichen Prüfung: 17. Oktober 2008

Contents

Zusammenfassung (Summary in German)	3
Summary	5
1 Introduction	7
1.1 Framework	7
1.1.1 Cosmological background	7
1.1.2 Galaxy formation and evolution	9
1.1.3 Observations of galaxies at high redshift: the role of submillimeter galaxies	10
1.1.4 Simulations of hierarchical galaxy formation	11
1.2 The role of technology	14
1.2.1 The <i>Spitzer</i> Space Telescope and IRS	14
1.2.2 The <i>Herschel</i> Space Observatory and PACS	16
2 The first observed mid-infrared spectra of submillimeter galaxies	19
2.1 Introduction	20
2.2 Observations and Data Reduction	21
2.3 Spectral Classification and Redshifts	21
2.4 ULIRG-like rest frame mid- to far-infrared SEDs	24
2.5 AGN content	25
2.6 Discussion	26
3 SMGs: redshifts and other properties from mid-IR spectroscopy	29
3.1 Introduction	30
3.2 Sample Selection	34
3.3 Observations and Data Analysis	34
3.4 Results	35
3.5 Discussion	45
3.5.1 The redshift distribution has a median of $z \sim 2.8$	45
3.5.2 SMGs have ULIRG-like SEDs and are largely starburst-powered . .	46
3.6 Conclusions	51

Contents

4	A backward evolution model for infrared surveys	53
4.1	Introduction	54
4.2	The AGN contribution in local ULIRGs and LIRGs	57
4.2.1	Sample selection and data reduction	58
4.2.2	Comparison to X-ray measurements	67
4.2.3	Distribution of the AGN contribution	70
4.2.4	Simulating the distribution of the AGN contribution	72
4.2.5	Evolution with redshift	74
4.2.6	Discussion and conclusions	79
4.3	The model: number counts and redshift distributions of infrared sources	81
4.3.1	The strong evolution of infrared galaxies: observational evidence	81
4.3.2	SEDs	82
4.3.3	Model parameters	86
4.4	Results and comparisons with available surveys	88
4.4.1	Pure starbursts SEDs	89
4.4.2	Adding the AGN contribution	91
4.5	Star formation history	96
4.6	AGN contribution to infrared emission	97
4.7	Open issues	100
4.8	Prediction for multiband <i>Herschel</i> surveys	101
4.9	Conclusions	102
5	Conclusions	105
	References	106

Zusammenfassung

Gegenstand dieser Dissertation sind die Eigenschaften und die Entwicklung von stark rotverschobenen leuchtstarken Infrarotgalaxien. Dazu verwende ich spektroskopische Beobachtungen im mittleren Infrarot und entwickle ein rückwärts gerichtetes Evolutionsmodell. Dieses Modell reproduziert aktuelle Beobachtungsgrößen wie die Anzahl von Galaxien und die Verteilungen in Rotverschiebung für verschiedene ausgewählte Galaxienpopulationen. Es trifft Vorhersagen für zukünftige Infrarotbeobachtungen.

In Kapitel 1 beschreibe ich den Stand der Forschung im Bereich der Galaxienentwicklung, sowohl von der Seite der Beobachtung als auch von der Seite der Theorie aus. Ich gebe auch einen kurzen Überblick über die beiden für die vorliegende Arbeit bedeutsamen Instrumente: den Infrarotspektrographen (IRS) an Bord des Weltraumteleskopes *Spitzer* und die Photodetector Array Camera and Spectrometer (PACS) des Weltraumteleskopes *Herschel*. IRS hat erstmalig Spektren von leuchtstarken $z \sim 2.5$ Infrarotgalaxien im mittleren Infrarot gewonnen. PACS wird 2009 gestartet und ist für die Untersuchung von Galaxienentwicklung im fernen Infraroten – dem Bereich, in dem viele Galaxien überwiegend strahlen – optimiert worden.

In den Kapiteln 2 und 3 diskutiere ich spektroskopische Beobachtungen von Submillimeter-Galaxien, deren Strahlung in ihrem jeweiligen Ruhesystem im mittleren Infrarot ausgesandt wird. Diese Objekte entsprechen wahrscheinlich einer entscheidenden Phase in der Bildung massereicher Galaxien. Sie stellen eine Herausforderung für unser Verständnis der Galaxienentwicklung sowie der parallelen Bildung von Sternsystemen und zentralen schwarzen Löchern dar. Kapitel 2 diskutiert die ersten beiden beobachteten derartigen Galaxien. SMMJ02399-0136 bei $z = 2.81$ zeigt eine Überlagerung von PAH-Emission mit einem Kontinuum im mittleren Infrarot. Dies deutet auf signifikante und etwa gleich starke Beiträge zur bolometrischen Helligkeit durch Sternentstehung und einen optisch dicken AGN hin. Ich errechne eine neue Rotverschiebung von $z = 2.80$ für MMJ154127+6616 aus einem IRS-Spektrum und schliesse dass dieses Objekt durch von Sternentstehung ausgelöster PAH-Emission dominiert wird. In Kapitel 3 stelle ich die gesamte Stichprobe aus 13 Submillimeter-Galaxien vor. Die Auswahl enthält ausschliesslich helle Objekte aus leeren Feldern und Gravitationslinsen-Suchgebieten mit genauen, interferometrisch bestimmten Positionen. Die Spektren werden mehrheitlich gut durch Modellspektren mit massiver Sternentstehung oder einer Kombination von PAH-Emission mit einem schwachen Infrarot-Kontinuum beschrieben; letzteres weist auf aktive Galaxienkerne (einschliesslich optisch dicker Kerne) hin. Ich bestimme im mittleren Infrarot die spektroskopischen Rotverschie-

bungen für alle neun mit IRS entdeckten Quellen; für drei dieser Quellen waren die Rotverschiebungen bisher unbekannt. Der Median der Verteilung der Rotverschiebungen liegt bei $z \sim 2.8$ unter der Annahme dass die mit IRS nicht entdeckten Quellen hoch-rotverschoben sind. Ohne diese Annahme liegt der Median bei $z \sim 2.7$ und somit etwas höher als der Median der Rotverschiebungen früherer, im Optischen durchgeführter Untersuchungen. Wären die mit IRS nicht detektierten Quellen bei ähnlichen Rotverschiebungen lokalisiert, würde dies eine höhere Extinktion im mittleren Infrarot erfordern als in lokalen ULIRGs beobachtet. Die Spektren im mittleren Infrarot (im Ruhesystem) und die spektrale Energieverteilung im mittleren bis fernen Infrarot entsprechen denen lokaler ultraleuchtkräftiger Infrarotgalaxien, zeigen allerdings höhere Flüsse. Im mittleren Infrarot bestätigen die Spektren den Eindruck früherer Beobachtungen: Submillimeter-Galaxien sind dominiert durch die Emission starker Sternentstehung und weniger durch die Emission des AGN.

In Kapitel 4 stelle ich ein empirisches “rückwärts gerichtetes” Galaxienentwicklungsmodell für helle Infrarotgalaxien vor, wobei dessen Randbedingungen durch Infrarotbeobachtungen in mehreren Wellenlängenbändern festgelegt werden. Zu diesem Zweck entwickle ich einen neuartigen Monte-Carlo-Algorithmus. Dieser Algorithmus berücksichtigt und variiert Verteilungsfunktionen der Ferninfrarot-SEDs und des AGN-Beitrags. Er errechnet für jede Quelle eine entsprechende Modell-SED und ermöglicht auf diese Weise den Vergleich mit verschiedenen Beobachtungen in zahlreichen Wellenlängenbereichen. Zum ersten Mal berücksichtigen die verwendeten SEDs Beiträge zu L_{TIR} sowohl von Sternentstehungsausbrüchen als auch von AGN. Diese – von L_{TIR} abhängigen – Beiträge werden unter Verwendung einer großen Stichprobe von LIRGs und ULIRGs für welche MIR-Spektren im *Spitzer*-Archiv zur Verfügung stehen quantifiziert. Die relative Beiträge ändern sich signifikant bei hohen z . Unter Verwendung von Literaturdaten folgt für Infrarotgalaxien aus unserem bestem Modell eine starke Leuchtkraft- ($[L = L_0(1+z)^{3.4}]$ bis $z = 2$) und Dichteevolution ($[\rho = \rho_0(1+z)]$ bis $z = 1$). Für höhere z nehmen die Entwicklungsraten mit $(1+z)^{-1}$ und $(1+z)^{-1.5}$ ab. Um sowohl die Anzahlen als auch die Verteilung der Rotverschiebungen vom MIR bis zum sub-mm-Bereich zu reproduzieren, muss sowohl eine Evolution der AGN-Beiträge als auch der $L - T$ -Beziehung eingeführt werden. Hinweise auf solche Entwicklungen wurden in aktuellen photometrischen und spektroskopischen Untersuchungen von sub-mm-Galaxien bereits gefunden. Unser Modell wird verwendet um erste Vorhersagen für künftige Infrarotbeobachtungen mit der Photodetector Array Camera and Spectrometer (PACS) auf *Herschel* zu treffen.

Teile dieser Dissertation wurden bereits zur Veröffentlichung angenommen (Lutz et al. 2005a - Kapitel 2; Valiante et al. 2007 - Kapitel 3).

Summary

In this thesis I study properties and evolution of high redshift luminous infrared galaxies, using mid-infrared spectroscopic observations and developing a backward evolution model. This model is able to reproduce current measurements like number counts and redshift distributions of different selected galaxy populations and can make predictions for future infrared surveys.

In Chapter 1 I describe the current framework of galaxy evolution, both from the point of view of observations and simulations. I also briefly describe the two instruments tightly related to this thesis: the Infrared Spectrograph (IRS) on board of the *Spitzer* Space Telescope and the Photodetector Array Camera and Spectrometer (PACS) mounted on the *Herschel* Space Observatory. The first has provided for the first time mid-infrared spectra of $z \sim 2.5$ luminous infrared galaxies. The second will be launched in 2009 and has been optimized to study galaxy evolution directly in the far-infrared wavebands that dominate the emission of many galaxies.

In Chapter 2 and 3 I present rest frame mid-infrared spectroscopy of submillimeter galaxies. These objects likely represent a key step in the formation of massive galaxies and pose a crucial challenge for our understanding of galaxies formation and of the co-evolution of spheroids and central black holes. Chapter 2 describes the first two galaxies observed. SMMJ02399-0136 at $z = 2.81$ shows a superposition of PAH emission features and a mid-infrared continuum, indicating significant and roughly equal contributions to its bolometric luminosity from star formation and from a Compton-thick AGN. I derive a new redshift of $z = 2.80$ for MMJ154127+6616 from the IRS spectrum and find this object is dominated by starburst PAH emission. In Chapter 3 the whole sample of 13 submillimeter galaxies is presented. The sample includes exclusively bright objects from blank fields and cluster lens assisted surveys that have accurate interferometric positions. I find that the majority of spectra are well fitted by a starburst template or by the superposition of PAH emission features and a weak mid-infrared continuum, the latter a tracer of Active Galactic Nuclei (including Compton-thick ones). I obtain mid-infrared spectroscopic redshifts for all nine sources detected with IRS. For three of them the redshifts were previously unknown. The median value of the redshift distribution is $z \sim 2.8$ if I assume that the four IRS non-detections are at high redshift. The median for the IRS detections alone is $z \sim 2.7$, slightly higher than the median redshift obtained by previous optical surveys. Placing the IRS non-detections at similar redshift would require rest frame mid-IR obscuration larger than is seen in local ULIRGs. The rest frame mid-infrared spectra and mid- to far-infrared spectral energy distributions are

Summary

consistent with those of local ultraluminous infrared galaxies, but scaled-up further in luminosity. The mid-infrared spectra of the entire sample confirm what the first observed objects had already shown: submillimeter galaxies are sites of extreme star formation, rather than X-ray-obscured AGN.

In Chapter 4 I present an empirical “backward” galaxy evolution model for infrared bright galaxies, constrained using multi-band infrared surveys. I develop a new Monte-Carlo algorithm for this task, implementing luminosity dependent distribution functions for the galaxies’ far-IR SED shape and for the AGN contribution and allowing for evolution of these quantities. A local far-IR luminosity function is adopted and evolved using power law parametrizations for possible luminosity and density evolutions. By attaching an appropriate SED to every source predicted by the model, the algorithm enables simultaneous comparisons with multiple surveys in a wide range of wave bands. The SEDs used take into account, for the first time, both the contributions of starbursts and AGN to the L_{TIR} . The quantification of this contribution, varying with the L_{TIR} , is made locally using a large sample of LIRGs and ULIRGs for which the mid-IR spectra are available in the *Spitzer* archive. This relation shows significant changes at high z . Constrained by data from the literature, our best-fit model adopts a very strong luminosity evolution, [$L = L_0(1+z)^{3.4}$], up to $z = 2$ and a density evolution, [$\rho = \rho_0(1+z)$], up to $z = 1$, for the population of infrared galaxies. At higher z , the evolution rates drop as $(1+z)^{-1}$ and $(1+z)^{-1.5}$ respectively. In order to reproduce both number counts and redshift distributions from mid-IR to submillimeter wavelengths, it is necessary to introduce both an evolution in the AGN contribution and an evolution in the $L - T$ relation: clues of such evolutions have been already shown in recent photometric and spectroscopic studies of submillimeter galaxies. The model developed is used to make the first predictions for future infrared surveys carried out with the Photodetector Array Camera and Spectrometer (PACS), mounted on *Herschel*.

Parts of this thesis have already been accepted for publication (Lutz et al. 2005a - Chapter 2; Valiante et al. 2007 - Chapter 3).

1

Introduction

1.1 Framework

In the last years, the focus of physical cosmology research is no more only centred on determining the values of the basic cosmological parameters, but is also starting to attack the problem of galaxy formation. A combination of factors is responsible for this change in emphasis. Firstly, the cold dark matter cosmological model has been placed on a much firmer footing by recent measurements of the cosmic microwave background radiation and galaxy clustering. Many of the fundamental cosmological parameters are known to an uncertainty of around 10%. Secondly, the increase in readily available computing power coupled with the development of powerful new techniques, such as the semi-analytical or hydrodynamical modelling of galaxy formation, means that we are in a position to generate strict predictions for the properties of galaxies in hierarchical cosmologies. Finally, and this will be the main subject of this thesis, the 1990s saw the first detections of sizeable populations of galaxies at high redshifts, allowing evolutionary trends to be established. Given these favourable conditions, there is now a genuine chance of making real progress in the advancement of our understanding of the process of galaxy formation and evolution.

1.1.1 Cosmological background

The cold dark matter (CDM) model has steadily gained acceptance since it was first mooted in the early 1980s (Peebles 1982; Blumenthal et al. 1984; Davis et al. 1985). The adoption of CDM as the theorist's model of choice can be attributed to three features. Firstly, there are many candidates for the cold dark matter particle predicted by extensions to the standard

1 Introduction

model of particle physics. Secondly, the model has tremendous predictive power. The state of the art in numerical N-body simulations of the growth of structure in a CDM cosmology allows incredibly detailed predictions to be made for a wide range of properties of the dark matter at all epochs. Thirdly, and most importantly, many of these predictions have turned out to be impressively successful.

Perhaps the most convincing support for the CDM model comes from the measurement of temperature anisotropies in the cosmic microwave background (CMB) radiation. The pattern of hot and cold spots in the radiation can be related to density fluctuations present in the Universe when the radiation and baryon fluids stopped interacting with one another at the epoch of recombination. Since the initial detection of these anisotropies on large angular scales by the *COsmic Background Explorer* (COBE) satellite in 1992 (Smoot et al. 1992), the power spectrum of the fluctuations has been gradually uncovered, culminating in the clear detection of three Doppler peaks due to acoustic oscillations in the photon-baryon fluid at the last scattering surface (de Bernardis et al. 2000; Hanany et al. 2000; Hinshaw et al. 2003; Jones et al. 2006; Hinshaw et al. 2007).

Further compelling support for the CDM model has come from two galaxy surveys which have revolutionized our view of the local Universe: the two-degree Field Galaxy Redshift Survey (2dFGRS; Colless et al. 2001) and the Sloan Digital Sky Survey (SDSS; York et al. 2000). The unprecedented size of these maps of the galaxy distribution has permitted the most accurate measurements to date of the power spectrum of galaxy clustering (Percival et al. 2001; Tegmark et al. 2004; Pope et al. 2004; Cole et al. 2005; Tegmark et al. 2006; Padmanabhan et al. 2007; Percival et al. 2007). For the first time, many of the basic cosmological parameters can be constrained with accuracies approaching or better than 10%.

Despite the burgeoning circumstantial evidence in support of the CDM model, it should be borne in mind that candidate particles for the non-baryonic dark matter have yet to be detected in the laboratory (Bergstrom 2000). In the current best fit CDM model, the universe is close to being spatially flat (e.g. Sanchez et al. 2006). However, less than 30% of the critical density required for this geometry is contributed by matter. The remainder is thought to be in some form of “dark energy”, one limiting case of which is the cosmological constant (Carroll 2004). Compelling support for a dark energy component came from the deduction that the expansion of the universe is accelerating, based on the Hubble diagram of distant type-Ia supernovae (Riess et al. 1998, 2004; Perlmutter et al. 1999). Even so, some authors considered also alternative models without any form of dark energy, as for example a modification to the law of gravity at large scales (Deffayet, Dvali & Gabadadze 2002; Carroll 2006).

The conclusion is that, within the context of the CDM model, there is now a very good idea of the values of most of the fundamental cosmological parameters. Thanks to the much narrower range of current cosmologies, galaxy evolution studies are now more focussed.

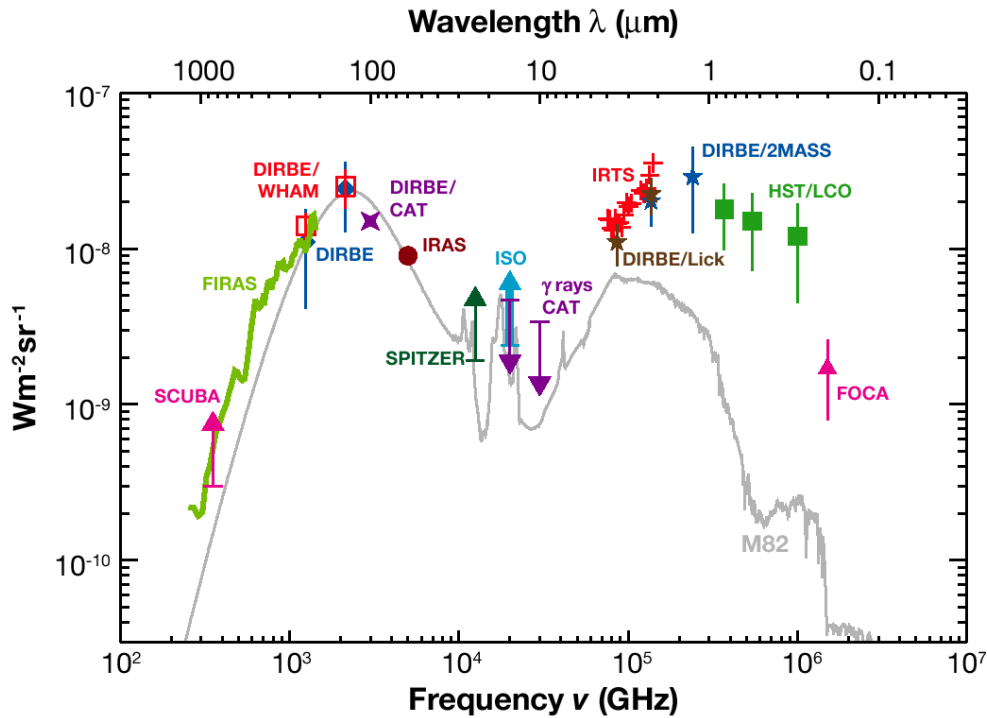


Figure 1.1: Spectral energy distribution of the extragalactic background, demonstrating that the total power output in the Universe at infrared wavelengths is comparable to the output at optical wavelengths (Lagache et al. 2005). The grey curve shows the spectrum for one representative $z \simeq 0$ starburst galaxy, M82, normalized to the peak of the background at $140\mu\text{m}$.

1.1.2 Galaxy formation and evolution

It came as a surprise when COBE found that the extragalactic background light at infrared (IR) was roughly equal to that at optical wavelengths (e.g. Puget et al. 1996; Hauser & Dwek 2001; see Fig. 1.1). In the local Universe, the volume density of infrared galaxies is such that there are not enough dusty, IR-luminous galaxies to account for this background, therefore the density of such systems must evolve strongly with redshift and must be important to the build-up of galaxies in the Universe (see e.g. Lagache et al. 2005 for a review). In fact, imaging observations with the *Spitzer* Space Telescope have shown that about 70% of the comoving star formation rate density (SFRD) at $0.5 < z < 3$ is obscured by dust (Le Flocc'h et al. 2005).

In the local Universe, these dusty galaxies are referred to as luminous infrared galaxies (LIRGs, $10^{11} \leq L_{\text{IR}} < 10^{12} L_{\odot}$) and ultraluminous infrared galaxies (ULIRGs, $L_{\text{IR}} \geq 10^{12} L_{\odot}$, see Sanders & Mirabel 1996 for a review), for which the IRAS mission has provided a

1 Introduction

comprehensive view. However, at high redshift, different selection functions from the observed submillimeter and from the observed mid-IR, in various combinations with ancillary multi-wavelength data, have led to a somewhat disjoint picture of the infrared luminous galaxy population. Dusty galaxies are detected in surveys at different wavelengths, with only partial overlap between the samples (Daddi et al. 2005; Lutz et al. 2005b; Yan et al. 2005; Pope et al. 2006). Clearly, we are learning that the current samples of infrared luminous galaxies at high redshift are probing a diverse population in different ways.

1.1.3 Observations of galaxies at high redshift: the role of submillimeter galaxies

The second key advance that makes progress in understanding galaxy formation possible is the unveiling of the galaxies in the high redshift universe in the second part of the 1990s. Observations of galaxies over a range of redshifts allow us to compare their properties at different epochs in the history of the universe. Such a comparison can be used to shed light on the formation and evolution of galaxies, and in particular can be used to establish whether galaxy formation is a steady process or if it took place much more vigorously at some earlier epoch. Perhaps the first major breakthrough in characterizing the high redshift universe was the Hubble Deep Field (Williams et al. 1996; Ferguson, Dickinson & Williams 2000). The unprecedented faint imaging of galaxies, combined with the Lyman-break dropout technique to isolate high redshift ($z > 2$) galaxies (Steidel et al. 1996) was essential in making possible the first determination of the cosmic star formation history over more than 80% of the age of the universe (Madau et al. 1996; Ellis 1997; Steidel et al. 1999). This approach uses measurements of the rest frame ultra-violet flux from a galaxy to infer the instantaneous star formation rate. The UV flux is dominated by stars with masses in excess of several times the mass of the sun; these stars are also short lived, producing the UV flux for timescales on the order of 10 Myr. One problem with conducting such a census at these wavelengths is that the rest-frame ultra-violet can be strongly attenuated by dust extinction.

The most enigmatic members of the high redshift population are the submillimeter galaxies (SMGs). These galaxies were discovered in abundance starting in the late 1990s with the *Submillimeter Common User Bolometer Array* (SCUBA, Holland et al. 1999) on the James Clerk Telescope (JCMT) and then later with the *Max-Planck Millimeter BOlometer* (MAMBO) camera on the Institut de Radio Astronomie Millimetrique (IRAM) 30-m telescope (see Blain et al. 2002 for a review). Due to the poor spatial resolution of current submillimeter telescopes and their faintness at all other wavelengths, these dusty galaxies have proven to be extremely difficult to study. However, since the dust enshrouded star formation phase is the dominant source of star formation at high redshift, the importance of SMGs as the most prominent examples of dusty galaxy evolution has motivated a great deal of challenging follow-up work. It has been found that SMGs are very massive systems (Genzel et al. 2003; Swinbank et al. 2004; Borys et al. 2005; Greve et al. 2005; Tacconi et al. 2006) at $z \sim 2$ (Chapman et al. 2005; Aretxaga et al. 2007) with disturbed morphologies

(Conselice et al. 2003; Chapman et al. 2003c; Pope et al. 2005) and number densities comparable to local massive elliptical galaxies. Fig. 1.2 shows the contribution from a subsample of SMGs to the global SFRD compared to that of UV-selected star-forming galaxies. The comoving space density of UV-selected galaxies at $z \sim 2$ is roughly 300 times that of bright SMGs (Chapman et al. 2003a; Adelberger et al. 2005). While SMGs are much less numerous than UV-selected galaxies, their contribution to the SFRD is comparable. For these reasons, SMGs have been thought to be connected to the present day massive galaxies via an evolutionary sequence (e.g. Lilly et al. 1999), and dynamical studies are beginning to flash out this evolutionary path (Tacconi et al. 2006, 2008).

The intense emission arising from SMGs might be associated not only to starburst activity, but also to radiation from an active galactic nucleus (AGN) that is absorbed by dust and re-radiated at longer wavelengths. The presence and relative importance of an AGN can be constrained by combining sub-millimeter observations with X-ray imaging. Alexander et al. (2005a) report that practically all objects with sub-millimeter emission contain an AGN, but that their large luminosities result primarily from high star formation rates. Nevertheless, this result assumes that SMGs are not highly obscured at X-ray wavelengths, and that there is no significant number of fully Compton-thick AGN, that are hard to detect in X-rays. Mid-IR spectroscopy is a powerful tool to discover the presence of an AGN even if its emission is absorbed in X-ray wavelengths, and to put limits to its contribution to the total infrared luminosity (Lutz et al. 2005a or Chapter 2, Menéndez-Delmestre et al. 2007, Valiante et al. 2007 or Chapter 3, Pope et al. 2008). The main source powering SMGs and how it can drive the subsequent evolution is one of the principle topics of this thesis.

An evolutionary scenario for massive galaxies was proposed by Sanders et al. (1988) in which massive galaxies undergo several stages before becoming a massive elliptical galaxy. The process starts with an infrared luminous phase, most likely triggered by a massive merger. During this stage of intense star formation, the AGN is also growing. As the AGN becomes larger it begins to feed back on the galaxy, eventually quenching the star formation completely by blowing off all the remaining dust and gas. Thus begins the QSO phase, where the AGN is free to dominate the emission. After exhausting its fuel, eventually the QSO settles down and we end up with a quiescent massive elliptical galaxy. While this scenario is widely accepted, important elements such as timescales are not completely understood. In particular, how long is the infrared luminous phase, how long does it take the AGN to develop and can there be multiple episodes of ULIRG and QSO activity?

1.1.4 Simulations of hierarchical galaxy formation

Not only observational technology has improved in the last decade, but also the precision of computer simulations which set the theoretical framework to deduce the formation of cosmic structures from first principles. They describe the build-up of cosmic filaments and galaxy clusters down to the scale of massive individual galaxies for different evolutionary scenarios.

In a picture of a hierarchically forming Universe, where small structures merge to form the

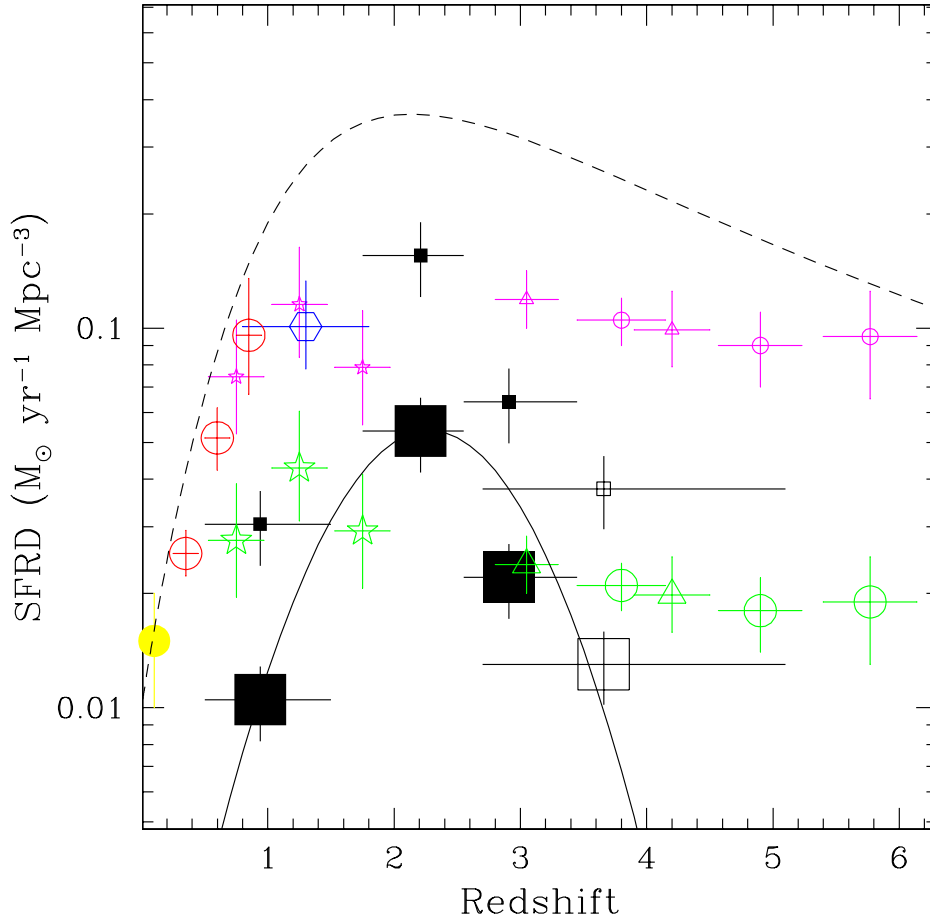


Figure 1.2: Evolution of the star formation rate density (SFRD) in the Universe (Chapman et al. 2005). The large solid squares show a sub-sample of radio-selected spectroscopically-identified SMGs and the large open square is their estimate of where the radio-undetected SMGs lie. The solid curve is a Gaussian fit to the 4 large squares. The smaller squares are the same SMG points corrected for completeness down to an $850\mu\text{m}$ flux of 1 mJy. The smaller open symbols are from UV (high- z circles, triangles), optical (stars, hexagon), mid-IR (low- z circles) and radio (solid circle) surveys (see Chapman et al. 2005 for a full list of references). Symbols which are smaller and shifted above slightly larger symbols have been corrected for dust extinction. The dashed line is the prediction from the model in Blain et al. (2002). Also due to the adopted completeness correction, the SMGs contribution to the SFRD looks comparable to the UV-selected galaxies one.

big mass concentrations observed today, dark matter “halos” are the main kinematic drivers of the mass assembly, and only on size scales of individual galaxies and below, baryons have an impact on structure formation.

The hierarchical model is a non-linear description of mass assembly, and it is therefore counter-intuitive in some respects. One example is the apparent “anti-hierarchical” growth of the most massive galaxies. The most massive galaxies at low redshift appear “old, red and dead”: they are dominated by old ($\sim 10^{10}$ yrs) stellar populations, have little gas content and form stars at very low rate. The age of the stellar populations indicates that their formation redshifts must be $z \gtrsim 1 - 2$. They have high metallicities, which indicates that they must have been evolving rapidly at high redshift. The tight correlation between the mass and the metallicity of galaxies has been confirmed by Tremonti et al. (2004) based on galaxies from the SLOAN survey.

However, the “anti-hierarchical growth” is only in contradiction to the hierarchical model, if the model is understood as a pure “bottom-up” assembly. This static view however neglects that the density perturbations during the recombination era were scale-free. The shorter collapse times of bigger overdensities will make the most massive objects evolve quickest. Smaller clumps will evolve at a slower pace. Since their number density will be depleted by accretion onto higher mass systems, and replenished by growth of smaller structures, overall the hierarchical model predicts a scenario, where the mass spectrum at a given redshift depends on a dynamical equilibrium between mass scales rather than a naive “bottom-up” assembly of structure. However, this implies that a galaxy of given mass observed in the local Universe will have a different evolution than a galaxy with equal mass observed at higher redshift.

The investigation of mass assembly is seriously hindered by the fact that the underlying driver, the dark matter, is not directly observable at high redshift. Dynamical mass estimates are difficult to obtain for large galaxy samples, due to the observational limitations of high-redshift studies. Only in recent times the measurement of dynamical masses with some accuracy became possible.

Dynamical and gas phase metallicity studies indicate that SMGs have high baryonic masses, approaching $10^{11} M_{\odot}$ (Genzel et al. 2003; Neri et al. 2003; Tecza et al. 2004; Swinbank et al. 2004; Greve et al. 2005; Tacconi et al. 2006). In order to reproduce the observed large space density of massive galaxies at $z = 2 - 3$, which are perhaps forming in rapid and efficient starbursts fed by galaxy mergers, previous models of hierarchical galaxy formation (Kauffmann et al. 1999; Baugh et al. 2003) need to be modified. Revised models must not only account for the number of massive dark halos needed to reproduce observations, but also for the speed and mechanism of the assembly of the associated baryons into massive galaxies (Tecza et al. 2004).

Using a model invoking a top-heavy stellar initial mass function (IMF), Baugh et al. (2005) were able to reproduce the observed submillimeter number counts. Comparison of the SMG population with the modelled number density of high redshift massive galaxies is still ongoing, also in view of new implementations of semi-analytical models taking into account

1 Introduction

feedback due to AGN. Using such models, Bower et al. (2006) have been able to predict a substantial population of massive galaxies out to $z \sim 5$, offering a promising route for a detailed comparison with the SMG population. In terms of chemical enrichment, the introduction of feedback from AGN in the model or the use of a top-heavy IMF are equivalent and both consistent with the observed metallicity in elliptical galaxies (Nagashima et al. 2005a,b). Extreme objects, such as the SMGs, can trace the formation of the $10^{11}M_{\odot}$ galaxies already fully assembled at redshifts of $z = 1.6 - 1.9$ (Cimatti et al. 2004). SMGs may also meet the constraint on rapid formation of low redshift massive ellipticals inferred from measurements of the α/Fe element abundance ratios (Thomas et al. 2005). A local census of the distribution of the baryonic mass reveals, albeit with large uncertainties, that the majority of the baryons presently locked in stars resides in spheroids (Persic & Salucci 1992; Fukugita, Hogan & Peebles 1998). A key question is then when and how all the baryons have come to reside in spheroids. If the connection between spheroid formation and the submillimeter population turns out to be well-founded, then determining the redshifts, bolometric luminosities and spectral properties of a significant number of sources would enhance our understanding of how spheroids formed and which mechanisms most strongly influenced their formation.

1.2 The role of technology

Most of the work of this thesis has been done using observations made with the Infrared Spectrograph (IRS, Houck et al. 2004) on board of the *Spitzer Space Telescope* on high redshift (see Chapter 2 and Chapter 3) and local (see § 4.2) targets. The modeling part (see § 4.3) is instead focused on the capabilities of an upcoming instrument, the Photodetector Array Camera and Spectrometer (PACS, Poglitsch et al. 2006) mounted on the *Herschel Space Observatory*. A short description of these instruments is given below.

1.2.1 The Spitzer Space Telescope and IRS

On August 25th, 2003, 1:35:39 EST, the *Spitzer Space Telescope* (Werner et al. 2004), formerly known as the *Space Infrared Telescope Facility* (SIRTF), was launched on a Delta 7920H from the Cape Canaveral Air Force Station in Florida, USA, into an Earth-trailing heliocentric orbit (see Fig. 1.3). It is the fourth and final element in NASA's family of Great Observatories and represents an important scientific and technical bridge to NASA's Astronomical Search for Origins program.

The *Spitzer* key science objectives can be summarized in four main topics: (i) search for and study of brown dwarfs and super planets; (ii) discovery and study of protoplanetary and planetary debris disks; (iii) study of ultraluminous galaxies and AGN; (iv) study of the early Universe. *Spitzer* is an ideal platform from which to extend and follow up on many of the results from the *Infrared Space Observatory* ISO. It is so much more sensitive than any

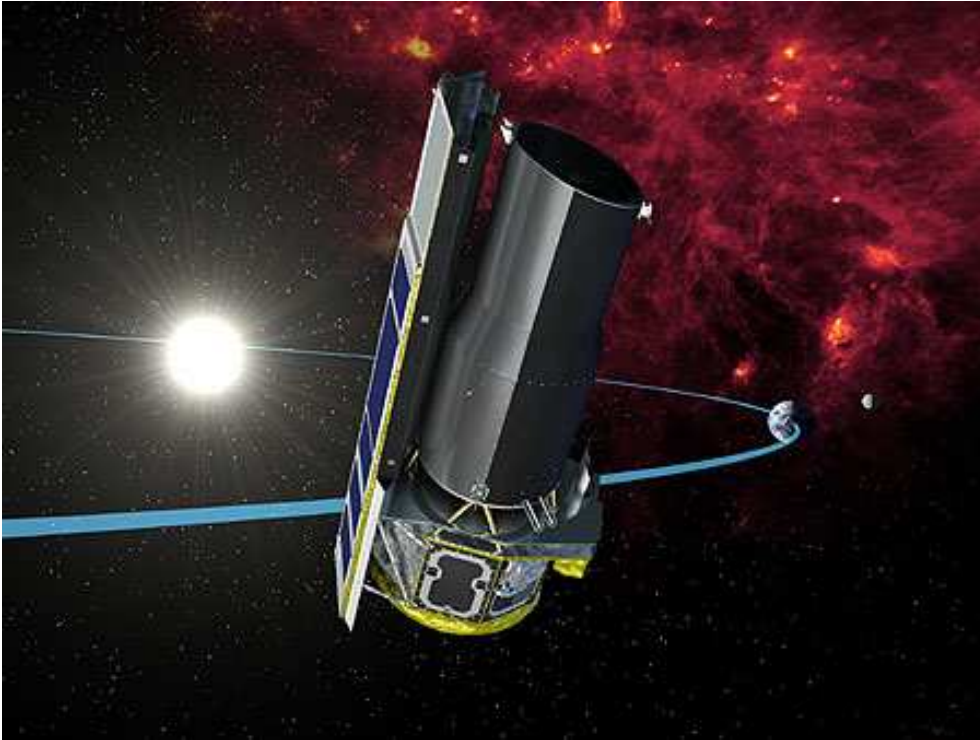


Figure 1.3: *Spitzer* in its heliocentric orbit (artist's conception).

Table 1.1. Properties of the IRS modules

Module	Array	Pixel Scale (")	Order	λ (μm)	$\lambda/\Delta\lambda$
Short-Low	Si:As	1.8	SL2	5.2–7.7 ^a	80–128
			SL1	7.4–14.5	64–128
			“blue” peak-up	13.3–18.7 ^b	~ 3
			“red” peak-up	18.5–26.0 ^b	~ 3
Long-Low	Si:Sb	5.1	LL2	14.0–21.3 ^a	80–128
			LL1	19.5–38.0	64–128
Short-High	Si:As	2.3	11–20	9.9–19.6	~ 600
Long-High	Si:Sb	4.5	11–20	18.7–37.2	~ 600

^aThe bonus orders cover 7.3 – 8.7 μm (SL) and 19.4 – 21.7 μm (LL).

^bThis is the full width at half maximum of the filter.

1 Introduction

preceding or contemporary infrared facility that observations from *Spitzer* itself are the best means of following up on many *Spitzer*'s scientific results.

Spitzer is composed of a spacecraft bus, a telescope, a cryostat, and three instruments: the *Infrared Array Camera* (IRAC), the *Multiband Imaging Photometer for Spitzer* (MIPS) and the *InfraRed Spectrograph* (IRS). The telescope is a Ritchey-Chrétien design, with a 85 cm primary mirror. It is the largest infrared telescope launched into space so far. With a field of view of $5' \times 5'$ (in most bands), diffraction limited detectors down to $\sim 5.5\mu\text{m}$ and sensitivities measured in μJy to mJy, it offers orders of magnitude improvements in capability over previous facilities. The cryogenic system is based on a 1.4 K liquid helium bath which cools the instruments, while the helium vapor produced by the dissipated instrument power is used to cool the telescope to its operating temperature of $\approx 5.5\text{ K}$. The three instruments are housed in the Multiple Instrument Chamber (MIC). All of them make extensive use of the large-format infrared detector array technology now available in the scientific community, covering a wavelength range between 2.6 and $160\mu\text{m}$.

The IRS is one of the three science instruments on the *Spitzer Space Telescope*. The instrument comprises four separate spectrograph modules covering the wavelength range from 5.3 to $38\mu\text{m}$ with low and moderate spectral resolutions, $R = \lambda/\Delta\lambda \approx 90$ and 600. In addition to its spectrographs, the IRS contains two peak-up imaging fields having bandpasses centered at $16\mu\text{m}$ (“blue”) and $22\mu\text{m}$ (“red”). The basic characteristics of the modules are summarized in Table 1.1. The primary objective in the design of the IRS was to take maximal advantage of the very low background conditions provided by the space environment. The low-resolution modules very nearly achieve the full background limited benefit of the space environment, while the high-resolution modules are detector noise limited.

1.2.2 The Herschel Space Observatory and PACS

The *Herschel Space Observatory* (see Fig. 1.4), or simply *Herschel*, is an astronomy observatory mission that targets approximately the 57 – $670\mu\text{m}$ wavelength range in the far-IR and submillimeter part of the electromagnetic spectrum, providing observation opportunities for the entire scientific community. *Herschel* is the fourth cornerstone mission in the European Space Agency (ESA) Horizon 2000 science program and will be launched in early 2009.

Herschel is the only space facility dedicated to this part of the submillimeter and far-IR range. Its vantage point in space provides several decisive advantages. The telescope will be passively cooled, which, together with a low emissivity and the total absence of atmospheric emission, offers a low and stable background enabling very sensitive photometric observations. Furthermore, the absence of even residual atmospheric absorption gives full access to the entire range of this elusive part of the spectrum, which offers the capability to perform completely uninterrupted spectral surveys.

Herschel is designed to observe the “cool universe”. It has the potential of discovering the earliest epoch proto-galaxies, revealing the cosmologically evolving AGN-starburst symbiosis, and unravelling the mechanisms involved in the formation of stars and planetary systems

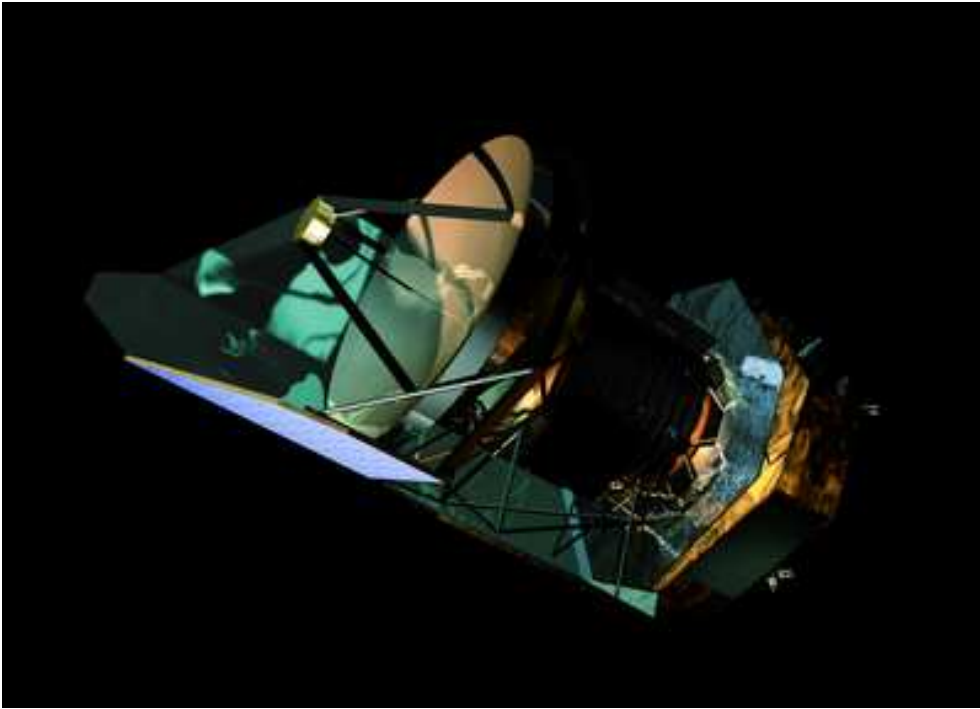


Figure 1.4: Artist's impression of *Herschel* .

bodies.

Black-bodies with temperatures between 5 and 50K peak in the *Herschel* wavelength range, and gases with temperatures between 10 and a few hundred K emit their brightest molecular and atomic emission lines here. Broadband thermal radiation from small dust grains - typically re-radiating absorbed shorter wavelength radiation - is the most common continuum emission process in these bands. This is the situation, for example, at “stellar” level in starforming molecular clouds, and at “galactic” level for active (starburst or AGN powered) galaxies. Because of its large primary mirror and small diffraction limited beam, *Herschel* will reach its far-IR confusion limit at fluxes much fainter than the small cryogenic telescopes of *ISO* or *Spitzer*. *Herschel* has been optimized to study galaxy evolution directly in the energetically dominant rest-frame far-IR, without the uncertainties involved in extrapolations from other wavelengths.

The key science objectives emphasize specifically the formation of stars and galaxies, and the interrelation between the two. The guaranteed time programs span topics related to solar system, interstellar matter, stars, galaxies and AGN and cosmology. In particular, the two main guaranteed time cosmological surveys are the *Herschel Multi-tiered Extragalactic Survey* (HERMES) and the *PACS Evolutionary Probe* (PEP).

The Photodetector Array Camera and Spectrometer (PACS) is one of the three science

1 Introduction

instruments for *Herschel*, together with the Spectral and Photometric Imaging Receiver (SPIRE) and the Heterodyne Instrument for the Far Infrared (HIFI). It covers the shortest wavelength band, $60 - 210\mu\text{m}$ and provides both photometric and spectroscopic observing modes suited to address the key scientific topics of the *Herschel* mission.

Photometric color diagnostics require spectral bands with a relative bandwidth $\Delta\lambda/\lambda < 1/2$. In coordination with the SPIRE bands, the PACS photometric bands have been defined as $60 - 85\mu\text{m}$, $85 - 130\mu\text{m}$ and $130 - 210\mu\text{m}$. A major fraction of the *Herschel* observing time will go to deep and/or large scale photometric surveys, like PEP and HERMES.

PEP is a *Herschel* guaranteed time key programme survey of the extragalactic sky, aimed to study the rest frame far-IR emission of galaxies up to redshift ~ 3 , as a function of environment. The survey will shed new light on the constituents of the cosmic infrared background and their nature, as well as on the co-evolution of AGN and starbursts. The PEP survey is driven by science goals addressing a number of key open topics in galaxy evolution: (i) resolve the Cosmic Infrared Background and determine the nature of its constituents; (ii) determine the cosmic evolution of dusty star formation and of the infrared luminosity function; (iii) elucidate the relation of far-IR emission and environment, and determine clustering properties; (iv) determine the contribution of AGN; (v) determine the infrared emission and energetics of known galaxy populations. PEP is coordinated with SPIRE observations of the same fields in the external HERMES program.

HERMES consists of a nested set of fields that will bring unprecedented depth and breadth to the study of infrared galaxies. HERMES will be used to measure the bolometric emission of infrared galaxies, study the evolution of the luminosity function, measure their clustering properties, and probe populations of galaxies below the confusion limit through lensing and statistical techniques. HERMES is closely coordinated with the PEP survey and will provide a rich data set legacy for the greater astronomical community to mine for years to come.

2

The first observed mid-infrared spectra of submillimeter galaxies

...or... Mid-Infrared Spectroscopy of Two Luminous Submillimeter Galaxies at $z \sim 2.8$

D. Lutz, E. Valiante, E. Sturm, R. Genzel, L. J. Tacconi, M. D. Lehnert, A. Sternberg, A. J. Baker 2005, ApJ, 625, 83L

Abstract

Using the Infrared Spectrograph (IRS) on board the Spitzer Space Telescope, we have obtained rest frame mid-infrared spectroscopy of two bright submillimeter galaxies. SMMJ02399-0136 at $z=2.81$ shows a superposition of PAH emission features and a mid-infrared continuum, indicating significant and roughly equal contributions to its bolometric luminosity from star formation and from a Compton-thick AGN. We derive a new redshift of $z=2.80$ for MMJ154127+6616 from the IRS spectrum and find this object is dominated by starburst PAH emission. The rest frame mid- to far-infrared spectral energy distributions are consistent with these submillimeter galaxies being scaled up versions of local ultraluminous infrared galaxies. The mid-infrared spectra support the scenario that submillimeter galaxies are sites of extreme star formation and represent a key phase in the formation of massive galaxies.

2.1 Introduction

Deep submm and mm surveys using SCUBA and MAMBO have changed our view of the early universe by resolving a significant fraction of the cosmic submm background into individual sources (Smail et al. (1997); Hughes et al. (1998); see also review by Blain et al. (2002) and references therein). A detailed characterization of these luminous (sub)millimeter galaxies (SMGs) is only slowly accumulating because of their faintness at all short wavelengths and the difficulty of counterpart identification. Photometric estimates of a median redshift of 2.5-3 for the SMG population (e.g. Carilli & Yun 2000) are consistent with the recent determination of a median redshift of $z \sim 2.2$ for the $\lesssim 50\%$ of the population accessible to optical spectroscopy (Chapman et al. 2005). The detection of SMGs and the implied star formation rates and space densities immediately motivated speculation that they may trace the formation of massive spheroids. Their central role in the assembly of massive galaxies is now becoming clearer through dynamical and through gas phase metallicity studies (Genzel et al. 2003; Neri et al. 2003; Tecza et al. 2004; Swinbank et al. 2004; Greve et al. 2005). Quantifying AGN in submillimeter galaxies is of immediate relevance for determining their source of luminosity. It is of further importance in the context of understanding the evolution of the black hole mass to spheroid relation during one of the key phases of massive galaxy formation, characterized by high star formation rates and gas content.

Rest frame mid-IR spectroscopy can further our understanding of SMGs in two ways. First, it can determine redshifts for SMGs that have up to now eluded optical redshift measurements. Mid-IR spectral features, in particular the narrow aromatic 'PAH' features, if present, allow reasonably accurate redshift measurements even for targets that are extremely faint at optical wavelengths. Like the radio continuum commonly employed to locate these galaxies (e.g. Ivison et al. 2002), mid-IR emission is closely linked to the bulk of the source luminosity that is emitted in the far-IR, and in addition contains spectral features. The risk of erroneous redshift assignment due to misidentification is thus reduced. CO line emission shares this property, however with existing instrumentation mid-IR spectroscopy has the advantage of larger fractional bandwidth coverage than mm spectroscopy. Second, low resolution mid-IR spectroscopy can be used to constrain the energy sources and physical conditions of infrared luminous galaxies, by decomposition into an AGN continuum and a starburst component that is dominated by PAH emission features. This technique has been successfully applied to the local infrared galaxy population during the ISO mission (e.g. Genzel et al. 1998; Laurent et al. 2000). With the sensitivity of IRS on the Spitzer Space Telescope it is now possible to extend this method to high redshift infrared populations such as the SMGs. Identifying the mid-IR AGN continuum by such spectral decomposition is possible even in the presence of significant obscuration, equivalent to tens of magnitudes in the rest frame optical and more in the rest frame ultraviolet. With appropriate signal-to-noise, relatively faint continua can be identified that do not yet strongly affect the broadband infrared colors that are another indicator of AGN. An application of the infrared methods further constraining AGN properties is in combination with rest frame hard X-ray emission

at levels signalling AGN activity, in particular for cases where the X-ray photon statistics is too limited to be able to fully constrain the X-ray obscuring column and thus the intrinsic X-ray luminosity.

We are pursuing a program of Spitzer rest frame mid-IR spectroscopy of a dozen bright and well studied SMGs. All have accurate interferometric positions that are the necessary prerequisite for such a study. In this letter, we present first results for two bright SMGs, SMMJ02399-0136, the brightest source found in the $850\mu\text{m}$ SCUBA Cluster Lens Survey (Smail et al. 1997, 2002), and MMJ154127+6616 detected near Abell 2125 in the MAMBO 1.2mm survey (Bertoldi et al. 2000). We adopt $\Omega_m = 0.3$, $\Omega_\Lambda = 0.7$ and $H_0 = 70 \text{ km s}^{-1} \text{ Mpc}^{-1}$.

2.2 Observations and Data Reduction

Low resolution long slit spectra were obtained using Spitzer-IRS (Houck et al. 2004) in the staring mode. SMMJ02399-0136 was observed in the LL1 $19.5\text{--}38.0\mu\text{m}$ module for 30 cycles of 120sec ramp duration. The total on-source integration time was 2 hours from addition of the independent spectra created by the telescope nod along the slit. MMJ154127+6616, without an available optical redshift, was observed in the same way in the LL1 module, and also for 15 cycles of 120sec ramp duration in the LL2 $14.0\text{--}21.3\mu\text{m}$ module. We replaced deviant pixels in the individual differences of the two nod positions of the pipeline 11.0.2 basic calibrated data frames by values representative of their spectral neighborhoods, and averaged the set of resulting 2-dimensional frames clipping deviant values for the individual pixel fluxes. After subtracting residual background emission, we used the SMART package (Higdon et al. 2004) to extract calibrated 1-dimensional spectra for the positive and negative beams; these were averaged into the final spectra. Figs. 2.1 and 2.2 show the extracted LL1 spectra of SMMJ02399-0136 and MMJ154127+6616 as well as parts of the corresponding 2-dimensional frames. The shorter wavelength LL2 spectrum of MMJ154127+6616 does not show significant continuum or feature emission at the target position, consistent with the tentative photometric fluxes of 0.05mJy and 0.07mJy at $16\mu\text{m}$ and $22\mu\text{m}$ reported by Charmandaris et al. (2004).

2.3 Spectral Classification and Redshifts

The spectrum of SMMJ02399-0136 shows well detected $6.2\mu\text{m}$ and $7.7\mu\text{m}$ aromatic ‘PAH’ emission features superposed on a strong continuum. It is well fitted by the superposition of a scaled and redshifted starburst spectrum (M82, Sturm et al. 2000) and a linearly rising, unabsorbed or little-absorbed continuum (Fig. 2.1). This spectrum is similar to those of local universe infrared luminous galaxies having significant contributions from both star formation and powerful AGN to their bolometric luminosities (e.g. Mrk 273, Genzel et al. 1998). The global fit shown in Fig. 2.1 corresponds to a redshift of 2.83. The $6.2\mu\text{m}$ feature

2 The first observed mid-infrared spectra of submillimeter galaxies

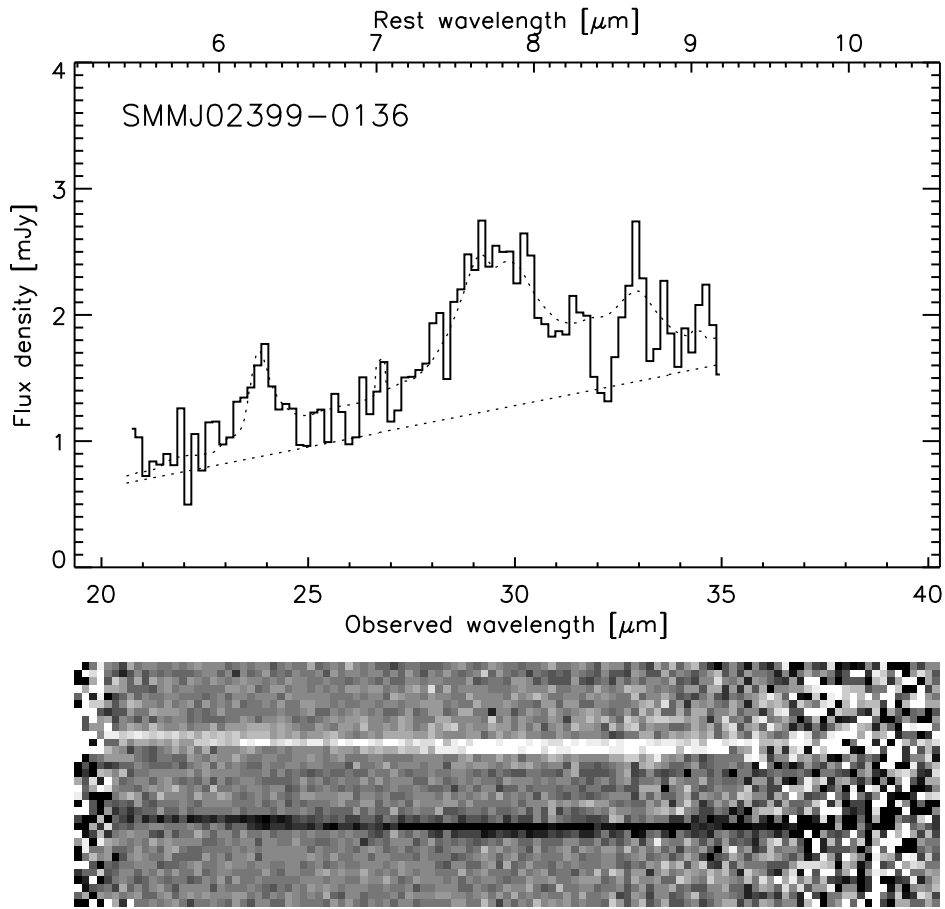


Figure 2.1: Spitzer IRS low resolution spectrum of SMMJ02399-0136 (top) along with the 2-dimensional long slit spectrum from which it was extracted (bottom). Note the increase of noise at long wavelengths. The thin dotted lines indicate the fit of the spectrum by the sum of the scaled and redshifted ISO-SWS spectrum of the starburst M82, and a linearly sloped and unabsorbed AGN continuum.

is intrinsically narrower and in a less complex part of the mid-IR spectrum than the broader $7.7/8.6\mu\text{m}$ complex. Fitting just this feature and comparing to similar fits to local universe ISO-SWS PAH spectra we obtain a redshift of 2.829 with a formal fit uncertainty of 0.013. Both values are in better than 1% agreement with the accurate CO-based redshift of 2.8076 for SMMJ02399-0136 (Frayser et al. 1998; Genzel et al. 2003).

The spectrum of the fainter MMJ154127+6616 is dominated by a broad peak near $30\mu\text{m}$ observed wavelength, with very weak emission at shorter and longer wavelengths. We identify this feature with the $7.7\mu\text{m}$ PAH feature, based on the fit obtained to a redshifted starburst spectrum (Fig. 2.2). We have also investigated fits with the obscured continuum spectrum

2.3 Spectral Classification and Redshifts

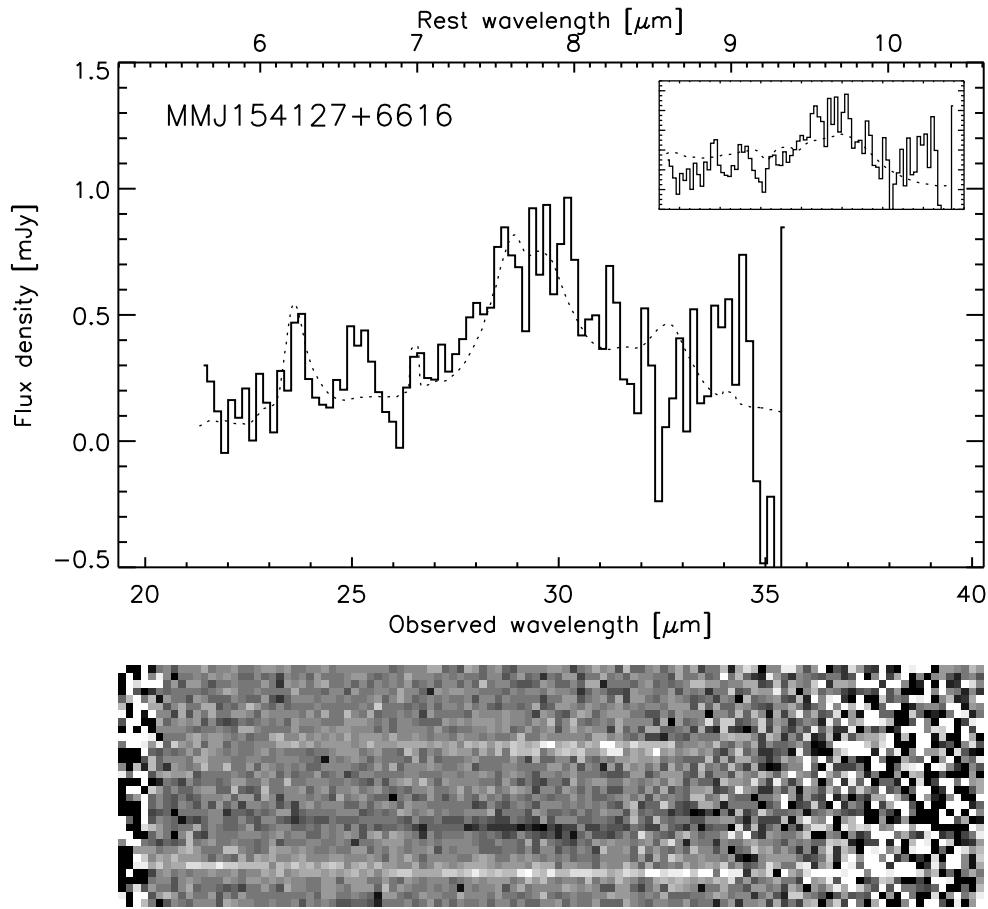


Figure 2.2: Spitzer IRS low resolution spectrum of MMJ154127+6616. The thin dotted line indicates the fit by the scaled and redshifted spectrum of M82. The small insert repeats the spectrum together with the lower quality fit by the obscured galaxy IRAS F00183-7111. The bright line at the bottom of the 2-dimensional spectrum is a serendipitous source found in the slit.

of IRAS F00183-7111 (Tran et al. 2001; Spoon et al. 2004). Such spectra have a maximum near $8\mu\text{m}$ rest wavelength, at the onset of the silicate absorption feature, and have to be considered as alternative fit to peaked mid-IR spectra of infrared galaxies. While resulting in comparable redshifts, the fits with an F00183-like spectrum do not reproduce the weakness or absence of short wavelength continuum emission (see insert of Fig. 2.2). This is corroborated by a factor 1.5 increase in reduced χ^2 of the 82 degree of freedom fit over this spectral range when changing from an M82 to an F00183 template. We suggest that the spectrum of MMJ154127+6616 is PAH dominated, consistent with the presence of a marginally significant maximum at the position of the $6.2\mu\text{m}$ feature.

2 The first observed mid-infrared spectra of submillimeter galaxies

To our knowledge, no redshift more accurate than the uncertain radio/submm estimates has been reported for MMJ154127+6616. Using their SCUBA 850 μ m flux in addition to the MAMBO 1.2mm and radio data, Eales et al. (2003, Object A2125-MM27 in their list) estimate $z=2.45_{-0.67}^{+0.67}$ from the radio/submm relation and $z < 1$ from the technically difficult 1200 μ m to 850 μ m ratio. Aretxaga et al. (2003) estimate $z=2.8_{-0.3}^{+1.7}$ with slight variations for different adopted models. From the fit in Fig. 2.2, we derive $z=2.80$ with an uncertainty of $\Delta z=0.1$ estimated from the global fit. This uncertainty is likely an upper limit given the indications for 6.2 μ m PAH emission. As for SMMJ02399-0136, this is somewhat larger than the median redshift for the part of the SMG population for which redshifts have been obtained in the optical (Chapman et al. 2005). These results demonstrate the power of IRS to derive redshifts not only for 24 μ m selected sources (Houck et al. 2005), but also for those bright SMG sources where the redshifted mid-IR features lie shortwards of the noisy $\lambda \gtrsim 35\mu$ m region of the IRS low resolution spectra.

For our adopted cosmology, a dust temperature of 45K and an emissivity index $\beta = 1.5$ (consistent with the SMMJ02399-0136 studies of Ivison et al. (1998) and Genzel et al. (2003)) the intrinsic 8-1000 μ m luminosity is $L_{IR} \sim 1.2 \times 10^{13} L_{\odot}$ for SMMJ02399-0136, after correcting for the lensing amplification of 2.45. We estimate $L_{IR} \sim 1.9 \times 10^{13} L_{\odot}$ for MMJ154127+6616 scaling with the intrinsic 850 μ m fluxes.

2.4 ULIRG-like rest frame mid- to far-infrared SEDs

The rest frame mid- to far-IR SEDs provide clues about properties, energy sources, and radiation fields of SMGs but are presently insufficiently constrained by direct observations. Constraints on their far-IR peaks are currently indirect using the observed submm and radio fluxes and the assumption of the radio/far-IR correlation for star forming galaxies (Chapman et al. 2003a, 2005). In view of the variations observed in local galaxy SEDs, we have added another constraint by comparing the ratio of PAH features and SCUBA 850 μ m continua (rest frame $\sim 222\mu$ m for our two objects). We adopt SCUBA fluxes of 23mJy for SMMJ02399-0136 (Smail et al. 2002) and 14.6mJy for MMJ154127+6616 (A2125-MM27 in Eales et al. 2003). In Fig. 2.3 the ratio of peak flux density of the 7.7 μ m PAH feature after continuum subtraction to the continuum flux density at rest frame 222 μ m for our two SMGs is compared to the same measure for 11 local ultraluminous infrared galaxies (ULIRGs) with PAH emission, where the PAH data have been taken from ISOPHOT-S observations (e.g. Rigopoulou et al. 1999) and the continua from slight extrapolations of the far-IR photometry of Klaas et al. (2001), which reaches out to 200 μ m observed wavelength. The PAH to far-IR ratios of the two SMGs are fully consistent with that of the local ULIRG population. These SED properties are in agreement with the finding from spatially resolved mm interferometry that SMGs are scaled up versions of the compact star formation events in local ULIRGs (Tacconi et al. 2006).

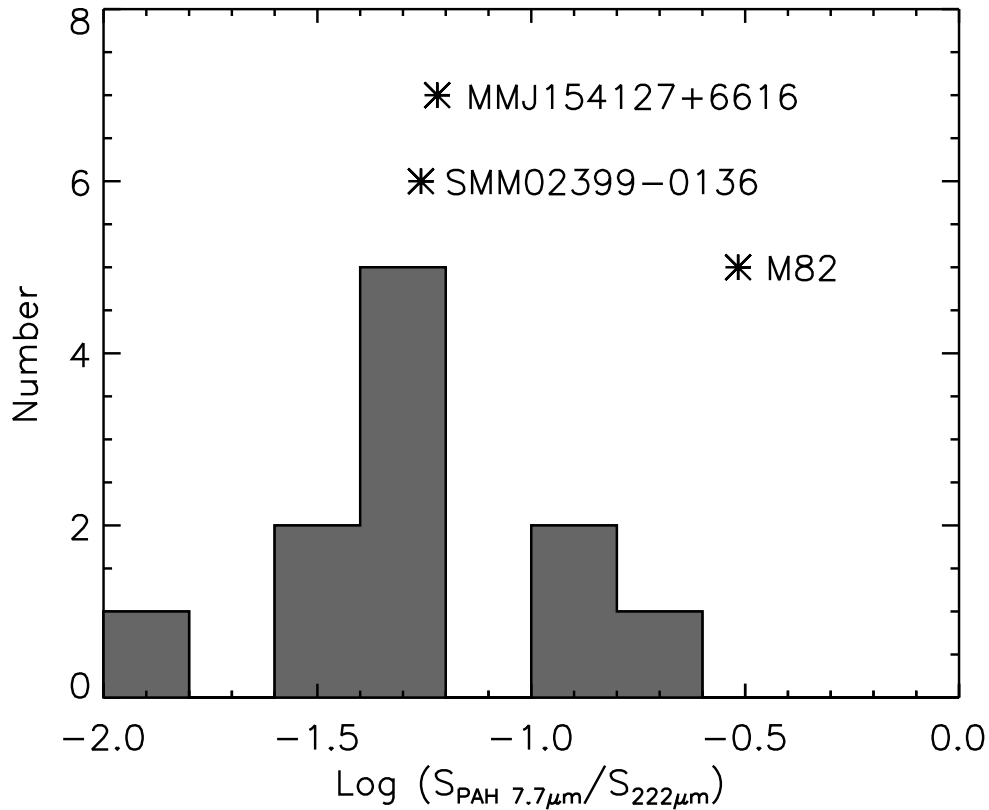


Figure 2.3: Histogram showing the ratio of PAH $7.7\mu\text{m}$ peak flux density and rest frame $222\mu\text{m}$ continuum flux density for eleven local ULIRGs. In this measure of the mid- to far-IR SED, the two SMGs are very similar to the local ULIRG population. However, both show a lower value than the low luminosity starburst M82. The M82 point is based on the PAH data of Förster Schreiber et al. (2003) and the far-IR continuum of Colbert et al. (1999), obtained in large and similar apertures.

2.5 AGN content

With both strong AGN continuum and PAH features, at a feature-to-continuum ratio ~ 1 , SMMJ02399-0136 is at the transition between predominantly starburst powered and predominantly AGN powered according to the mid-IR diagnostic of Genzel et al. (1998). AGN signatures are also seen in the optical spectrum (Ivison et al. 1998). The combination of mid-IR spectroscopy and the Chandra X-ray data of Bautz et al. (2000) can constrain the properties of this AGN. Bautz et al. (2000) clearly detect relatively hard X-ray emission from SMMJ02399-0136, with an observed luminosity in the rest frame 2-10keV band of $0.18 \times 10^{44} \text{erg s}^{-1}$ (corrected to our adopted cosmological parameters). Because of limited photon statistics, their data cannot discriminate between seeing the direct AGN emission, al-

2 The first observed mid-infrared spectra of submillimeter galaxies

though absorbed by a significant column of $N_H \sim 10^{24} \text{cm}^{-2}$ (with the intrinsic emission ~ 15 times brighter), and a fully Compton thick AGN seen in reflection, with the intrinsic emission brighter by the inverse of their adopted reflection efficiency of 0.022. For two related reasons, the Compton thick case appears more consistent with our infrared observations. First, the ratio of rest frame hard X-rays and mid-IR AGN continuum $\log(L_{2-10\text{keV}}/\nu L_\nu(6\mu\text{m}))$ is -0.54 for the reflected case. This ratio is at the center of the equivalent distribution of mid-IR to intrinsic hard X-ray ratios for local AGN, studied by Lutz et al. (2004), while the lower ratio for the direct emission case would be at the lower end of this distribution. Second, correcting from intrinsic hard X-rays to AGN bolometric luminosity assuming $L_{2-10\text{keV}}/L_{\text{Bol}} \sim 0.09$ for AGN (Elvis et al. 1994), the reflected case with $L_{\text{Bol,AGN}} \approx 2 \times 10^{12} L_\odot$ is closer to the roughly similar contributions of AGN and star formation that are suggested by the infrared spectroscopy. In summary, we conclude that SMMJ02399-0136 is powered by roughly equal contributions of star formation and a Compton-thick AGN.

No strong AGN continuum is present in MMJ154127+6616 (Fig. 2.2), in particular below $\sim 6.5\mu\text{m}$ rest wavelength where it would be most easily detectable in the presence of PAHs. This is further supported by the weakness of the tentative 16 and $22\mu\text{m}$ photometric detections of Charmandaris et al. (2004), at levels below 0.1mJy. As is the case for local ULIRGs, it is appropriate to caution that our conclusion of dominance of star formation does not exclude in any way the presence of an AGN that is a very minor contributor to the bolometric luminosity. A significant number of minor AGN in SMGs is suggested by the deepest Chandra observations (Alexander et al. 2003, 2005a).

2.6 Discussion

We have presented Spitzer mid-IR spectroscopy of two of the brightest known submillimeter galaxies, SMMJ02399-0136 and MMJ154127+6616. Our unambiguous detections of PAH spectral features and mid-IR continua allows us to constrain the energy sources in these objects, and to determine the previously unknown redshift for one of them (MMJ154127+6616). We find that the luminosity of the first galaxy is generated by approximately equal contributions from star-formation and an AGN. The second galaxy is dominated by star formation.

The existence of star formation dominated systems at infrared luminosities in excess of $10^{13} L_\odot$ is unique to the high redshift universe. In our previous ISO studies of ULIRGs in the local universe, using the same mid-IR methods, we have found star formation dominated systems only up to a luminosity of $10^{12.65} L_\odot$ (Rigopoulou et al. 1999; Tran et al. 2001). Similar conclusions have been reached from optical spectroscopy of local ULIRGs (Veilleux et al. 1999). The existence of higher luminosity starbursts in SMGs may be related to their higher gas fractions (Greve et al. 2005; Tacconi et al. 2006). Star formation proceeding at these extreme rates in high redshift objects ($\gtrsim 1000 M_\odot/\text{yr}$ for $L_{\text{IR}} > 10^{13} L_\odot$) naturally fits into the evolving understanding of the formation of massive galaxies at high redshift, however. Such extreme events can trace the formation of the $10^{11} M_\odot$ galaxies already fully assem-

bled at redshifts $z=1.6$ to 1.9 (Cimatti et al. 2004). Rapid star-formation may also meet the constraint on rapid formation of massive ellipticals inferred from measurements of the α/Fe element abundance ratios (Thomas et al. 2005).

Spectroscopy with IRS can play a central role in elucidating the relationships amongst various infrared selected high redshift galaxy populations. Houck et al. (2005) have recently obtained IRS spectra of $24\mu\text{m}$ bright ($>0.75\text{mJy}$) but optically faint ($R>24$) galaxies selected from a large area Spitzer survey. Submillimeter galaxies at $z\sim 2$ with an Arp220-like SED but still more luminous than a typical SMG from the current SCUBA/MAMBO surveys could meet the basic brightness and obscuration constraint of this sample. The preponderance of heavily obscured continua in the Houck et al. (2005) spectra, however, unlike the PAH and PAH plus continuum spectra of our two SMGs, argues for a small overlap between the two populations, and that the population of R-band faint but $24\mu\text{m}$ bright sources may be dominated by obscured AGN.

2 The first observed mid-infrared spectra of submillimeter galaxies

3

Submillimeter galaxies: redshifts and other properties from mid-infrared spectroscopy

...or... **A Mid-Infrared Spectroscopic Study of Submillimeter Galaxies: Luminous Starbursts at High Redshift**

E. Valiante, D. Lutz, E. Sturm, R. Genzel, L. J. Tacconi, M. D. Lehnert, A. J. Baker
2007, ApJ, 660, 1020

Abstract

We present rest frame mid-infrared spectroscopy of a sample of 13 submillimeter galaxies, obtained using the Infrared Spectrograph (IRS) on board the *Spitzer Space Telescope*. The sample includes exclusively bright objects from blank fields and cluster lens assisted surveys that have accurate interferometric positions. We find that the majority of spectra are well fitted by a starburst template or by the superposition of PAH emission features and a weak mid-infrared continuum, the latter a tracer of Active Galactic Nuclei (including Compton-thick ones). We obtain mid-infrared spectroscopic redshifts for all nine sources detected with IRS. For three of them the redshifts were previously unknown. The median value of the redshift distribution is $z \sim 2.8$ if we assume that the four IRS non-detections are at high redshift. The median for the IRS detections alone is $z \sim 2.7$. Placing the IRS non-detections at similar redshift would require rest frame mid-infrared obscuration larger than is seen in local ULIRGs. The rest frame mid-infrared spectra and mid- to far-infrared spectral energy distributions are consistent with those of local ultraluminous infrared galaxies, but scaled-up further in luminosity. The mid-infrared spectra support the scenario that submillimeter galax-

3 SMGs: redshifts and other properties from mid-IR spectroscopy

ies are sites of extreme star formation, rather than X-ray-obscured AGN, and represent a critical phase in the formation of massive galaxies.

3.1 Introduction

Less than a decade ago, observations with the Submillimeter Common User Bolometer Array (SCUBA; Holland et al. 1999) on the James Clerk Maxwell Telescope (JCMT) identified a new and unexpected population of submillimeter galaxies (SMGs; Smail et al. 1997; Barger et al. 1998; Hughes et al. 1998). Subsequent surveys with SCUBA and the Max-Planck Millimeter Bolometer (MAMBO; Kreysa et al. 1998) array at the IRAM 30m telescope resolved a significant fraction of the cosmic submillimeter background into individual sources (see Blain et al. 2002, and references therein).

A detailed understanding of this population has emerged only slowly, due to their faintness at all short wavelengths and the difficulty of counterpart identification. Photometric estimates of median redshifts around $2.5 - 3$ (Carilli & Yun 2000) are consistent with the recent determination of a median redshift of $z \sim 2.2$ for the $< 50\%$ of the population accessible to optical spectroscopy (Chapman et al. 2005). The optical redshifts of the radio/optical bright sub-class have been confirmed in ~ 15 cases through CO line detections (Frayser et al. 1998, 1999; Neri et al. 2003; Greve et al. 2005; Tacconi et al. 2006). Despite all these efforts, the characterization of the redshift distribution remains incomplete, because of the large positional uncertainties for SMGs without interferometric counterparts and the large uncertainties in purely photometric redshift estimates.

The tendency of SMGs to be faint in X-rays suggests that their large luminosities result primarily from high star formation rates (Alexander et al. 2003, 2005b). Moreover, dynamical and gas phase metallicity studies indicate that they have high (approaching $10^{11} M_{\odot}$) baryonic masses (Genzel et al. 2003; Neri et al. 2003; Tecza et al. 2004; Swinbank et al. 2004; Greve et al. 2005; Tacconi et al. 2006). These high star formation rates and baryonic masses place SMGs at the assembly phase of massive galaxies at $z = 2 - 3$, in rapid and efficient starbursts likely fed by mergers.

The contribution of AGN to the energy output of SMGs has strong implications for the origin of the cosmic submm background and the origin of the correlation between black hole mass and spheroid mass/velocity dispersion in local galaxies (Ferrarese & Merritt 2000; Gebhardt et al. 2000). Studies of the relationship between stellar and black hole mass in submillimeter galaxies, under the assumption of accretion at the Eddington rate, are consistent with a model where the supermassive black holes in SMGs undergo rapid growth to reach the local $M_{\star} - M_{BH}$ relation (Borys et al. 2005).

SMGs thus mark a pivotal point in the evolution of massive galaxies and their central black holes. Observational characterisation of their redshift distribution, space densities, masses, metallicities, AGN content, and structure are all needed to understand their position in the hierarchical growth of structure and the growth of massive galaxies by accretion of gas and

merging of smaller galaxies. Models of hierarchical galaxy formation (e.g. Kauffmann et al. 1999; Baugh et al. 2003) are in the process of adapting to the new observational constraints including properties of the SMG population (e.g. Baugh et al. 2005; Bower et al. 2006). Extreme objects, such as the SMGs, can trace the formation of the $10^{11}M_{\odot}$ galaxies already fully assembled at redshifts of $z = 1.6 - 1.9$ (Cimatti et al. 2004). SMGs may also meet the constraint on rapid formation of low redshift massive ellipticals inferred from measurements of the α/Fe element abundance ratios (Thomas et al. 2005).

Even at low resolution, rest-frame mid-IR spectra of galaxies can discriminate between star formation and accretion (e.g. Genzel & Cesarsky 2000, and references therein) on the basis of four distinct spectral components observed in dusty galaxies in the local universe (Genzel et al. 1998; Laurent et al. 2000; Tran et al. 2001): (i) strong emission from the polycyclic aromatic hydrocarbon (PAH) features found over a very wide range of star forming galaxies; (ii) a variable but usually small contribution of an HII region continuum steeply rising in the $6 - 15\mu\text{m}$ rest wavelength range; (iii) a flatter PAH-free AGN continuum, sometimes accompanied by additional $\lambda \geq 10\mu\text{m}$ AGN related silicate emission (Siebenmorgen et al. 2005; Hao et al. 2005); (iv) absorption features in the $6 - 8\mu\text{m}$ range as well as the $9.7\mu\text{m}$ silicate absorption feature (Spoon et al. 2004).

The anticorrelation between PAH feature strength relative to the AGN continuum and the ionization state of the ionized gas (Genzel et al. 1998; Dale et al. 2006) strongly supports these low resolution diagnostics. Using the *Spitzer Space Telescope*, the diagnostics based on the mid-IR spectral components of dusty luminous and ultraluminous galaxies in the local universe can now be applied to dusty SMGs at high redshift. Our understanding of SMGs can be improved in three ways:

Verification or determination of redshift. Mid-IR spectral features, in particular the narrow aromatic PAH features, if present, allow reasonably accurate redshift measurements ($\Delta z \lesssim 0.1$) even for targets that are very faint at optical wavelengths. They can verify optical redshifts in cases where these are uncertain due to the faintness of the optical counterpart, due to the presence of multiple candidate counterparts (e.g. 8 of 73 SMGs in the redshift study of Chapman et al. (2005) have multiple radio/optical counterparts), or due to uncertain optical line identifications. Mid-IR emission shares with CO line emission a reduced risk of an erroneous redshift assignment, because these tracers are more closely linked than the rest frame UV to the rest frame submm/far-IR emission that dominates the SMG's bolometric luminosity. They are thus less likely to measure the redshift of a misidentified neighbouring source. The difficulties of identification with an optical/near-IR source can be seen for example in the case of HDF850.1 (Downes et al. 1999; Dunlop et al. 2004). For sources without known optical redshifts, new mid-IR spectroscopic redshifts strongly reduce the template ambiguities that are always possible for model-dependent photometric redshifts. The advantage of the mid-IR spectra over CO is that, with existing instrumentation, there is a larger fractional bandwidth coverage than for mm spectroscopy. The disadvantage is that for a possible $z \gtrsim 4$ tail of the SMG redshift distribution, the main PAH features leave the wavelength range of sensitive *Spitzer* spectroscopy.

3 SMGs: redshifts and other properties from mid-IR spectroscopy

Evaluation of the relative importance of AGN and star formation using the relative strength of PAH and continuum. Submillimeter sources are likely starburst-dominated but more luminous than the threshold above which most local infrared galaxies are AGN dominated (Rigopoulou et al. 1999; Veilleux et al. 1999; Tran et al. 2001). Furthermore, although massive ellipticals in formation should also be forming massive black holes in order to produce the $M_{\text{BH}} - \sigma$ relation (Tremaine et al. 2002), evidence for energetically dominant AGN is scarce (Alexander et al. 2003). Evaluating the ratio of starburst and AGN contributions will also allow us to investigate trends with other quantities. We adopt a ratio of $7.7 \mu\text{m}$ PAH feature to local continuum of 1 as the border between starburst and AGN dominance in the bolometric luminosity, following the approach of Genzel et al. (1998) that is well matched to the rest wavelength coverage and S/N of our data. The rest-frame mid-IR continuum, if isolated from the non-AGN components of the mid-IR emission, can provide constraints on the role of AGN, including highly X-ray absorbed sources (Krabbe et al. 2001; Lutz et al. 2004). Mid-IR spectra tracing the re-radiation of absorbed AGN emission thus also constrain the presence of Compton-thick AGN that are hard to separate from inactive objects in current high redshift X-ray data, because their X-ray photon statistics can be insufficient for clear identification of reflected AGN emission, or because the AGN may be fully covered.

Constraining physical conditions in the starburst. By analogy with local galaxies, dilute/cool regions are expected to show a larger PAH contribution to the total infrared emission and a cooler rest frame far-IR peak than denser starbursts (e.g. Dale & Helou 2002). Very compact regions can show absorption features like those of water ice and hydrocarbons. Some of the most luminous local ULIRGs exhibit strong continua with superposed emission features deviating from a canonical PAH feature shape (Tran et al. 2001; Spoon et al. 2004). Similar features may be found in SMGs.

Spitzer spectra are also important to test the popular assumption (e.g. Hughes et al. 1998) that the overall spectral energy distributions (SEDs) of SMGs are similar to those of local star forming Ultraluminous Infrared Galaxies (ULIRGs).

In § 2 we discuss the properties of our sample and in § 3 observations and data analysis. § 4 presents the SMG spectra and discusses the results of their spectral decomposition. In § 5 we discuss the implications for the three main questions raised above.

Table 3.1. Summary of SMG observations

Name	RA J2000	DEC J2000	Error "	Ref.	SL1 (7.4 – 14.5 μm) s \times n.of cycles	LL2 (14.0 – 21.3 μm) s \times n.of cycles	LL1 (19.5 – 38.0 μm) s \times n.of cycles
SMMJ00266+1708 (M12)	00:26:34.10	+17:08:33.7	0.8	F00		120 \times 15	120 \times 30
SMMJ02399–0136 (L1/L2)	02:39:51.87	–01:35:58.8	0.6	G03			120 \times 30
SMMJ09429+4659 (H8)	09:42:53.42	+46:59:54.5		L02		120 \times 15	120 \times 30
SMMJ09431+4700 (H7/H6)	09:43:03.69	+47:00:15.5	0.3	N03			120 \times 30
SMMJ10519+5723 (LE 850.18)	10:51:55.47	+57:23:12.7		I02			120 \times 30
SMMJ10521+5719 (LE 850.12)	10:52:07.49	+57:19:04.0		I02			120 \times 30
MMJ120517–0743.1	12:05:17.86	–07:43:08.5	0.4	D04		120 \times 10	120 \times 30
MMJ120539–0745.4	12:05:39.47	–07:45:27.0	0.4	D04			120 \times 30
MMJ120546–0741.5	12:05:46.59	–07:41:34.3	0.5	D04		120 \times 11	120 \times 30
MMJ154127+6615	15:41:26.90	+66:14:37.3	0.1	B00		120 \times 15	120 \times 30
MMJ154127+6616	15:41:27.28	+66:16:17.0	0.1	B00		120 \times 15	120 \times 30
SMMJ16369+4057 (N2 850.8)	16:36:58.78	+40:57:28.1		I02	240 \times 5	120 \times 10	
SMMJ16371+4053 (N2 1200.17)	16:37:06.60	+40:53:14.0		G05		120 \times 15	120 \times 30

Note. — Names in brackets indicate aliases used in the literature.

References. — Interferometric positions adopted for the IRS observations (from VLA 1.4GHz if not stated otherwise): B00: Bertoldi et al. (2000). D04: PdBI mm position of Dannerbauer et al. (2004). F00: OVRO mm position of Frayer et al. (2000). G03: PdBI mm position of Genzel et al. (2003). G05: 1" from final CO position of Greve et al. (2005). I02: Ivison et al. (2002). L02: Ledlow et al. (2002). N03: PdBI mm position of Neri et al. (2003). For sources with no position error stated in the references, we assume $\lesssim 0.5''$ from the interferometer configurations used.

3.2 Sample Selection

Among the several hundred SMGs detected up to now, our sample comprises exclusively bright ($S_{850\mu\text{m}} \geq 4.5\text{ mJy}$) objects from blank field and cluster lens assisted surveys that have accurate positions from follow-up radio or mm interferometry. Objects from radio pre-selected surveys are not included because they may be biased in redshift and AGN content. No constraint on mid-IR photometric flux, which could potentially introduce biases on SED and energy source, has been applied to this Cycle 1 sample.

The 13 targets in our sample (Tab. 3.1) cover the full range of properties of currently known bright SMGs. The ratio of optical/near-IR and submm fluxes, for example, varies by almost two orders of magnitude (Tab. 3.3). In our sample there are 6 objects with published optical redshifts (Barger et al. 1999; Ledlow et al. 2002; Chapman et al. 2005), in particular 3 cases where the redshift is confirmed by CO interferometry (Neri et al. 2003; Greve et al. 2005), and 7 sources for which no optical redshift is available due to their faintness in the optical/NIR. Including these objects in our study reduces biases that may affect a sample with measured optical redshifts only. The redshift distribution of a sample with optical redshifts will tend to avoid the optical “spectroscopic desert” ($1.2 \lesssim z \lesssim 1.8$). It may also favour sources with unobscured or mildly obscured AGNs because of their strong rest frame UV line emission. We include sources selected at $850\mu\text{m}$ (SCUBA) as well as sources selected at 1.2 mm (MAMBO), to minimize selection effects due to redshift or dust temperature. The sample encompasses the five brightest MAMBO sources with interferometric positions known before the Voss et al. (2006) observations, and a number of bright SCUBA sources with and without redshifts.

3.3 Observations and Data Analysis

We obtained low resolution ($\lambda/\Delta\lambda \sim 60\text{-}120$ ¹) long slit spectra using *Spitzer* IRS (Houck et al. 2004) in the staring mode. The detector is a 128×128 Si:Sb (LL1 and LL2 modules) or Si:As (SL1 module) Blocked Impurity Band (BIB) array.

The rest wavelength range required to detect mid-IR PAH features and/or silicate absorption, encompasses at a minimum wavelengths from 5 to $10\mu\text{m}$. Observations are summarized in Table 3.1. Most of the sources were observed in the LL1 $19.5 - 38.0\mu\text{m}$ module for 30 cycles of 120 s ramp duration. The total on-source integration time was 2 hours from addition of the independent spectra created by the telescope nods along the slit. For objects with $z < 2.7$ and most objects with unknown redshifts we added the LL2 $14.0 - 21.3\mu\text{m}$ range with 15 cycles of 120 s to ensure the required rest wavelength coverage for all plausible redshifts. In these cases, the slit on-source integration time for LL2 was 1 hour. Because of its low redshift, SMMJ16369+4057 was observed in the LL2 range for 10 cycles of 120 s, as well as in the SL1 $7.4 - 14.5\mu\text{m}$ module for 5 cycles of 240 s (2400 s total on-source inte-

¹ $\Delta\lambda$ is approximately constant as a function of λ

gration time). With this observation plan, we could in principle detect both the $6.2\mu\text{m}$ and $7.7\mu\text{m}$ PAH features of a starburst-like spectrum for a redshift range $1.4 \lesssim z \lesssim 3.8$. For lower redshifts, we would observe only the $7.7\mu\text{m}$ maximum, which fully exits the observed window at $z \sim 1$, but the longer wavelength 11.3 and $12.7\mu\text{m}$ PAH features might still provide useful information in such a case.

We reduced the data as follows. We subtracted, for each cycle, the two nod positions of the pipeline 14.0.0 basic calibrated data frames. In the difference just calculated, we replaced deviant pixels by values representative of their spectral neighborhoods. We subtracted residual wavelength dependent background, measured in source-free regions of the two dimensional difference spectra. In averaging all the cycles of the 2-dimensional subtracted frames, we excluded values more than three times the local noise away from the mean. The calibrated 1-dimensional spectra for the positive and the negative beams were extracted using the optimum extraction mode of the SPICE analysis package (version 1.4.1), and the two 1-dimensional spectra averaged in order to obtain the final spectrum.

Since our measurements are close to the sensitivity limit of the instrument, for all data analysis we cut away the long and short wavelength ends of each module, where the noise is much higher and no signals are detected.

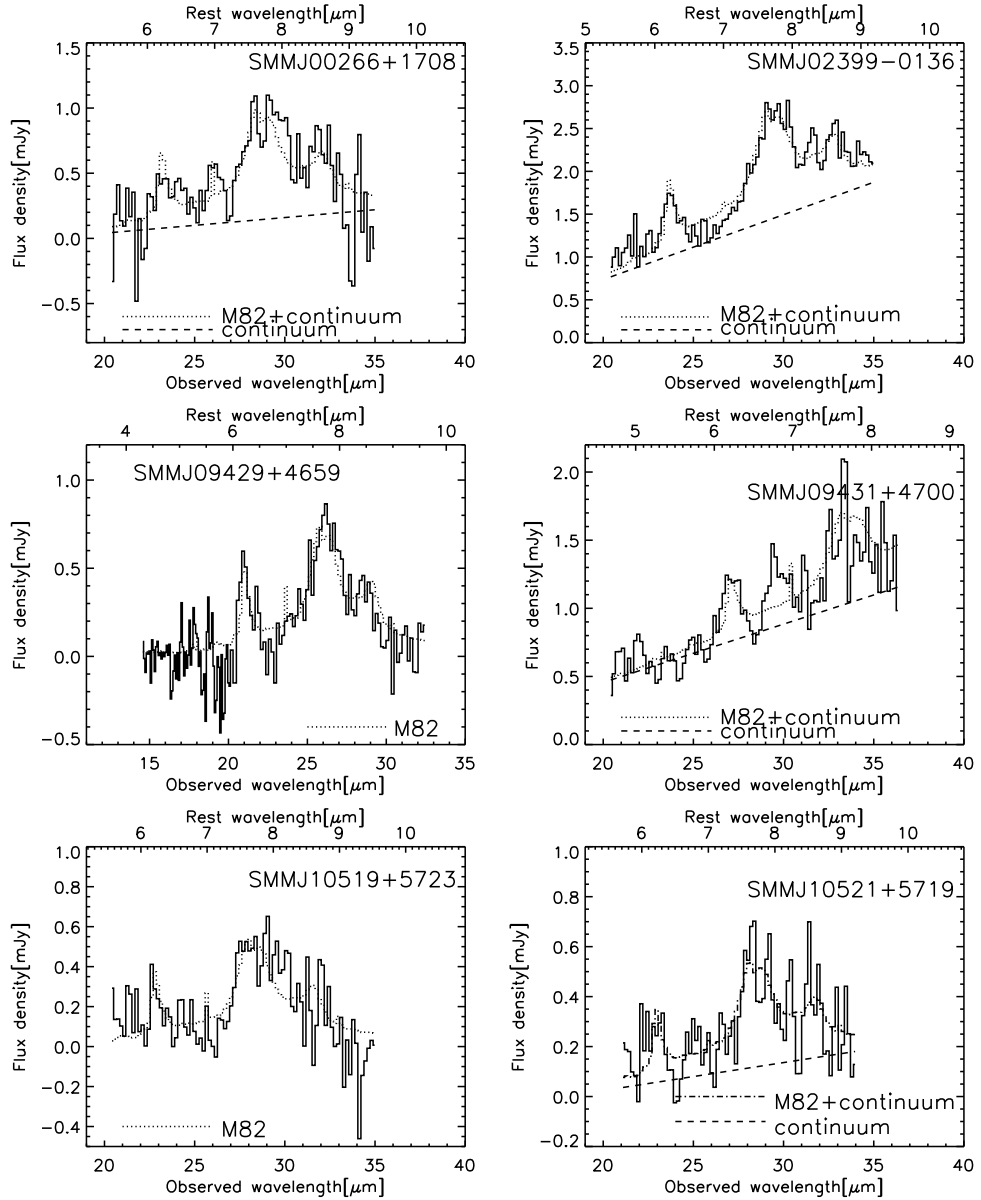
In order to do a formal χ^2 template fit for our sources, it is essential to determine the uncertainties on each point of the spectra. We used a processed and deglitched image of one of the undetected sources (the result was comparable for all of them). The uncertainty for each spectral point was calculated as the noise for each pixel times the square root of the number of pixels in the resolution element, which increases with wavelength. The noise for each pixel has been assumed to be the clipped standard deviation on a row of 20 pixels, all at the same wavelength. The resolution element is defined by the IRS pipeline, subdividing the region of the array covered by the spectrum into a sequence of trapezoid-shaped elements. This estimate may not fully reproduce the absolute noise level of a given observation, due to variations in strength of zodiacal light with position and epoch, but is a good approximation of the change of noise as a function of wavelength.

3.4 Results

The spectra of the nine detected sources and the four non-detections are shown in Fig. 3.1. As quantified by spectral fits below, the detections can be well reproduced by combinations of PAH features and continua. In one or two cases a heavily absorbed continuum is a possible alternative. We do not see evidence for strong continua like those seen in local QSOs (which also show silicate emission outside our rest wavelength coverage, see Siebenmorgen et al. 2005; Hao et al. 2005; Sturm et al. 2005). These individual classifications are strongly supported by the PAH-dominated average of the SMG spectra (Fig. 3.3), which shows much larger PAH equivalent widths than those seen in QSOs (Schweitzer et al. 2006).

In spectra of faint sources with poor S/N, only spectral features with sufficiently large

3 SMGs: redshifts and other properties from mid-IR spectroscopy



continue in the next page...

3.4 Results

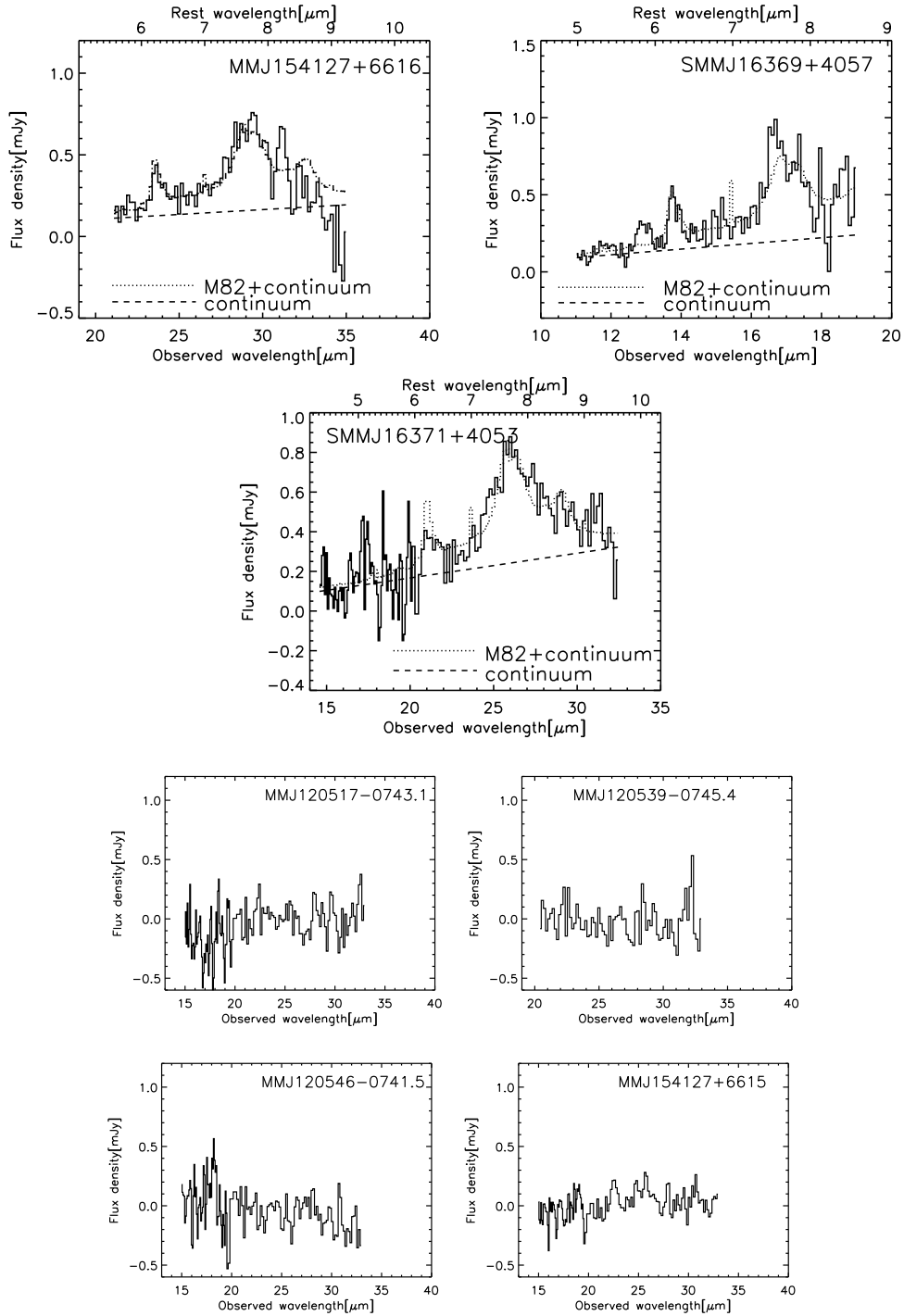


Figure 3.1: *Spitzer* IRS low resolution spectra (solid lines) of the sample galaxies. The detected sources are shown together with the best template fit (dotted and dashed line). Their redshifts are listed in Table 3.3. The last four spectra show the IRS non-detections.

3 SMGs: redshifts and other properties from mid-IR spectroscopy

equivalent widths can be used for redshift determination. At one extreme, these features are the strong PAH emission features of starburst galaxies. These features appear whenever the interstellar medium is exposed to moderately intense UV radiation (e.g. Draine 2003). The other extreme shows strong absorption features, the strongest being silicate absorption. Examples of PAH features in high-redshift galaxies observed with the IRS are in Teplitz et al. (2005), Yan et al. (2005), Lutz et al. (2005a) and Desai et al. (2006). An extremely absorbed local source is IRAS F00183–7111 (Tran et al. 2001), whose IRS spectrum is shown in Spoon et al. (2004). Similar spectra have been observed in optically obscured high redshift $24\mu\text{m}$ sources (Houck et al. 2005; Weedman et al. 2006).

Redshifts can be determined by using either the set of strong PAH emission features or, for absorbed spectra, the $8\mu\text{m}$ maximum and nearby silicate absorption. The strongest PAH feature is at $7.7\mu\text{m}$ (rest frame), so a similar redshift ($\Delta z \sim \pm 0.1$) would be derived even if it is ambiguous whether the strongest feature is the $8\mu\text{m}$ maximum or true PAH emission. The physical interpretation of the source, however, would be very different for the two alternatives. In order to correctly identify a feature as a PAH, we require an indication that the $6.2\mu\text{m}$ PAH feature is present with the correct shape and (relative to the $7.7\mu\text{m}$ feature) flux. In our sample there is no case of ambiguity in identifying a feature with the 6.2 or $7.7\mu\text{m}$ PAH feature, since either both are detected or the large observed width indicates that it cannot be the narrow $6.2\mu\text{m}$ PAH feature. For one of our sources, template fits identify such a single broad maximum with the $7.7\mu\text{m}$ PAH feature but, depending on rest wavelength range and S/N, it is also conceivable to identify such a single broad peak with the $8\mu\text{m}$ maximum of absorbed spectra.

We estimate redshifts by χ^2 fitting a selection of templates to the full spectra of the detected sources. Two of the templates are absorbed, likely AGN dominated, sources: NGC 4418 and IRAS F00183–7111 (Spoon et al. 2001, 2004). As a third template we use the starburst spectrum of M82 (Sturm et al. 2000), both as observed (with the spectrum dominated by pure PAH emission) and with superposition of an additional continuum that is assumed to vary linearly over the short wavelength range covered. This last spectrum is similar to those of local universe infrared luminous galaxies having significant contributions to their bolometric luminosities from both star formation and powerful AGN (e.g. NGC7469, Mrk273, Genzel et al. 1998). More complex fitting schemes have been used to interpret low resolution mid-IR spectra, for example by allowing additional obscuration to the PAH dominated starburst component (e.g. Tran et al. 2001), or by decomposing the PAH component into individual features that can be well approximated by Lorentzians (e.g. Boulanger et al. 1998; Smith et al. 2007). We do not adopt such schemes here because of the S/N of our data and their rest wavelength coverage, which is usually limited to shortward of the $9.6\mu\text{m}$ silicate absorption by the IRS wavelength range.

Table 3.2. Fit results. The best fit is in bold type (see the text for details).

Name	M82			IRAS F00183–7111			NGC 4418			M82 + continuum		
	χ^2	z	σ_z	χ^2	z	σ_z	χ^2	z	σ_z	χ^2	z	σ_z
SMMJ00266+1708	1.5	2.73	0.01	3.1	2.75	0.02	2.0	2.66	0.01	1.4	2.73	0.02
SMMJ02399–0136	17	2.80	0.01	12	2.86	0.01	21	2.72	0.01	1.1	2.81	0.02
SMMJ09429+4659	0.58	2.38	0.01	1.5	2.43	0.03	0.86	2.33	0.01	0.59	2.38	0.02
SMMJ09431+4700	10	3.33	0.01	3.2	3.26	0.04	4.3	3.20	0.01	0.99	3.36	0.02
SMMJ10519+5723	0.68	2.67	0.01	1.2	2.67	0.01	0.80	2.64	0.02	0.75	2.67	0.02
SMMJ10521+5719	0.74	2.69	0.01	1.3	2.75	0.02	1.1	2.73	0.01	0.63	2.69	0.02
MMJ154127+6616	0.55	2.78	0.01	0.82	2.79	0.04	0.60	2.67	0.02	0.35	2.79	0.02
SMMJ16369+4057	0.60	1.21	0.01	1.68	1.17	0.01	0.66	1.12	0.01	0.30	1.21	0.02
SMMJ16371+4053	1.1	2.38	0.01	1.2	2.48	0.01	1.3	2.34	0.01	0.41	2.38	0.02

Table 3.3. Properties of the SMG sample

Name	S _{850μm} mJy	S _{1.4GHz} μ Jy	K mag	Opt. mag	Magn. ^a	z ^b	z _r ^c	S _{PAH7.7μm} ^d mJy	S _{cont.7.7μm} ^e mJy	T _d K	L _{IR} × 10 ¹³ L _⊙	Best fit
SMMJ00266+1708	18.6±2.4 ^f	94±15 ^f	22.5 ^f	I>26.1 ^f	2.4		2.73	0.750	0.150	35.3	0.5	M82+AGN
SMMJ02399−0136	23.0±1.9 ^g	526±10 ^h	17.8 ^g	R=21.2 ^g	2.5	2.80	2.81	1.12	1.44	53.4	2.5	M82+AGN
SMMJ09429+4659	4.9±1.5 ⁱ	970±3.5 ⁱ	19.7 ^j	R=25.2 ^j	1.3		2.38	0.683		83.0	6.3	M82
SMMJ09431+4700	10.5±1.8 ⁱ	55±3.5 ⁱ	20.2 ^j	R=23.8 ^j	1.2	3.35	3.36	0.607	1.04	41.6	0.9	M82+AGN
SMMJ10519+5723	4.5±1.3 ^k	47±10 ^k	>20.4 ^k	I=24.6 ^k		2.69	2.67	0.491		42.0	0.5	M82
SMMJ10521+5719	6.2±1.6 ^k	278±12 ^k	>20.6 ^k	I=22.7 ^k		2.69	2.69	0.370	0.122	61.6	2.9	M82+AGN
MMJ120517−0743.1	6.3±0.9 ^l	40±13 ^m	22.5 ^m	R~25.4 ^m			>3.6					
MMJ120539−0745.4	6.3±1.4 ^l	55±13 ^m	>22.7 ^m	R>26.2 ^m			>3.6					
MMJ120546−0741.5	18.5±2.4 ^l	42±13 ^m	21.9 ^m	R>26.2 ^m			>3.6					
MMJ154127+6615	10.7±1.2 ^l	81±13 ⁿ	>21.2 ^p	R>24.9 ^p			>3.6					
MMJ154127+6616	14.6±1.8 ^l	67±13 ⁿ	20.5 ⁿ	R>24.5 ⁿ			2.79	0.472	0.159	35.0	0.9	M82+AGN
SMMJ16369+4057	5.1±1.4 ^k	74±29 ^k	18.2 ^k	R=22.5 ^k		1.19	1.21	0.493	0.205	27.5	0.1	M82+AGN
SMMJ16371+4053	11.2±2.9 ^o	74±23 ^o	19.2 ^q	I=23.2 ^q		2.38	2.38	0.519	0.242	34.3	0.7	M82+AGN

^a Adopted lensing magnification where applicable, magnification 1 is assumed otherwise. See text for references. The submm and radio fluxes and optical/near-IR magnitudes listed here are not corrected for amplification, while the infrared luminosities include the magnification correction. Magnitudes are on the Vega system.

^b Redshift from previous measurements. See text for references.

^c Redshift from best fit to IRS mid-IR spectrum (this work). Uncertainty 0.06 including effects of potential template mismatch (See Sect. 4 for details).

^d Flux of the PAH 7.7 μ m rest frame feature after continuum subtraction.

^e Flux of the continuum 7.7 μ m rest frame.

^f Frayer et al. (2000) ^g Smail et al. (2002) ^h Smail et al. (2000) ⁱ Cowie et al. (2002)

^j Ledlow et al. (2002). Opt/NIR magnitudes for SMMJ09431+4700 are dominated by the H6 component while H7 is the dominant submm component (Tacconi et al. 2006).

^k Ivison et al. (2002) ^l Eales et al. (2003) ^m Dannerbauer et al. (2004) ⁿ Bertoldi et al. (2000) ^o Chapman et al. (2005)

^p Dannerbauer (2004) ^q Smail et al. (2004)

Results of the fits with all the templates are listed in Table 3.2. The best fit for each object is specified in Tab. 3.3 and also shown in Fig. 3.1. The redshifts derived from the best fit for each object are also listed in Table 3.3 and compared with known redshifts where available. IRS and previous redshifts are consistent for all the sources with previous redshifts from optical spectroscopy (SMMJ09431+4700 by Ledlow et al. 2002, SMMJ10519+5723, SMMJ10521+5719, SMMJ16369+4057, SMMJ16371+4053 by Chapman et al. 2005) and sometimes from additional CO interferometry (SMMJ02399–0136 by Frayer et al. 1998, SMMJ09431+4700 by Neri et al. 2003; Tacconi et al. 2006, SMMJ16371+4053 by Greve et al. 2005). Three sources had no accurately determined redshifts. For these, our new redshifts are inside the 68% confidence intervals of the photometric estimates of Aretxaga et al. (2003) for at least three of the six different evolutionary models used. The formal fit uncertainties for the best fit are up to about $\Delta z = 0.02$ but, because of the differences in derived redshifts depending on the template used (Tab. 3.2), we assume an uncertainty $\Delta z = 0.06$ for all the sources. For the six sources with both IRS and optical/CO redshifts measured we derive a reassuringly small standard deviation of only 0.014 for the difference between the best fitting IRS redshift and independent optical/CO redshift. For the uncertainty of a new IRS redshift from a spectrum similar in quality to our spectra, we nevertheless prefer the more conservative $\Delta z = 0.06$ which includes the possibility of template mismatch, since the smaller standard deviation for the six sources includes only spectra reasonably well fit by the M82 (plus continuum) templates. $\Delta z = 0.06$ is an overestimate if the identification of PAHs in the spectrum is beyond any doubt. Table 3.3 also classifies sources according to how their spectra are characterized: PAH emission (M82 best fit), silicate absorption or $8\mu\text{m}$ maximum (IRAS F00183–7111 or NGC4418 best fit) or a superposition of PAH emission and a linearly rising continuum.

In the remainder of this section, we briefly describe the properties of the nine SMGs with new mid-IR rest-frame spectra. We also discuss the four non-detections and constraints on their possible redshifts and/or SED properties.

SMMJ00266+1708 The best fit for this source is the combination of M82 PAH template and weak AGN continuum (see Fig. 3.1), but the χ^2 test gives similar results also for the absorbed continuum NGC 4418 template (see Tab. 3.2). The spectrum lacks an evident $6.2\mu\text{m}$ PAH feature, the wavelength of which still falls in the observed band. We proceed with the best fitting PAH plus continuum interpretation but note that a classification of this source as an absorbed AGN is clearly not excluded. The previous photometric redshift of $z = 2.7_{-0.2}^{+2.3}$ estimated by Aretxaga et al. (2003) is consistent with our spectroscopic value $z = 2.73 \pm 0.06$. Frayer et al. (2000) identify a faint ERO counterpart for this object and estimate a lensing magnification 2.4 ± 0.5 , which we adopt for our analysis.

SMMJ02399–0136 The mid-IR spectrum of this source was already presented by Lutz et al. (2005a). It contains well detected $6.2\mu\text{m}$ and $7.7\mu\text{m}$ PAH features superposed on a strong continuum (see Fig. 3.1). This source is at the transition between predominantly starburst powered and predominantly AGN powered, according to the mid-IR diagnostics of Genzel et al. (1998) and Laurent et al. (2000). AGN signatures are also seen in the optical spectrum

3 SMGs: redshifts and other properties from mid-IR spectroscopy

(Ivison et al. 1998). Combining mid-IR spectroscopy and *Chandra* X-ray observations (Bautz et al. 2000), we conclude that this source is powered by roughly equal contributions of star formation and a Compton-thick AGN (Lutz et al. 2005a), in agreement with constraints on the importance of star formation in this object from molecular gas mass and its position relative to the radio/far-IR correlation (Frayser et al. 1998). Its luminosity (see Tab. 3.3) is calculated taking into account a lensing magnification factor of 2.5 (Ivison et al. 1998).

SMMJ09429+4659 This source is well fitted with the starburst-like M82 spectrum. No accurate redshift was previously known for this object. Using the radio-submm spectral index and the models from Carilli & Yun (2000), the estimated redshift is $z = 0.4 \pm 0.3$. The intense radio emission suggests, though, that there is a significant radio contribution from an AGN, even if we do not see AGN emission in the mid-IR spectrum, making the value estimated from the radio-submm relation only a lower limit. Assuming this galaxy follows the $K - z$ relationship for powerful radio galaxies (Jarvis et al. 2001), it most likely lies at $z \geq 2$ (Ledlow et al. 2002). Our spectroscopic value of $z = 2.38 \pm 0.06$ confirms the high redshift of this object. The luminosity of this source (see Tab. 3.3) is calculated by taking into account a lensing magnification factor of 1.3 (Cowie et al. 2002).

SMMJ09431+4700 We pointed IRS at the mm position (Neri et al. 2003) of component H7 in the notation of Ledlow et al. (2002), but note that component H6 is included in the observing aperture as well. This source has the highest redshift of the sample ($z = 3.36$), not accounting for the non-detected objects (see discussion below). It is well fitted with a PAH spectrum plus a strong linearly rising continuum, so we infer that it is powered by both starburst activity and a powerful AGN (see Fig. 3.1). The optical spectrum of component H6 shows features of a weak AGN (Ledlow et al. 2002). The spectral properties, line widths and line ratios of this galaxy are very similar to those seen for narrow-line Seyfert 1 galaxies (NLSy1s; Crenshaw et al. 1991). *XMM-Newton* observations (Ledlow et al. 2002) suggest that the intrinsic X-ray luminosity of the AGN is modest ($L_{2-10\text{keV}} \lesssim 10^{44} \text{ erg s}^{-1} \text{ cm}^{-2}$), unless there is heavy obscuration. Comparison to the strong rest frame mid-IR continuum seen in the IRS spectrum suggests the latter is indeed the case: at $L_{2-10\text{keV}}/vL_{\nu}(6\mu\text{m}) \lesssim 0.015$, this source falls more than an order of magnitude below the relation between unobscured 2 – 10 keV luminosity and $6\mu\text{m}$ continuum for local AGN (Lutz et al. 2004). SMMJ09431+4700 hosts a heavily obscured or Compton-thick AGN, the location of which we cannot firmly ascribe to component H6 or H7. The luminosity of SMMJ09431+4700 (see Tab. 3.3) is calculated taking into account a lensing amplification factor of 1.2 (Cowie et al. 2002).

SMMJ10519+5723 The lowest χ^2 fit for this object is the one with the M82 starburst template, which is supported by the tentative detection of a $6.2\mu\text{m}$ PAH feature. Still, the χ^2 is not much higher for the absorbed continuum template NGC 4418. We interpret this source as powered by starburst activity, consistent with optical spectroscopy (Chapman et al. 2005), but note that an absorbed continuum interpretation cannot be firmly excluded. The spectroscopic redshift suggested for this source by Chapman et al. (2003a) was $z = 3.699$. Later, Egami et al. (2004) and Chapman et al. (2005) indicated values of $z = 2.69$ and $z =$

2.686 respectively. Our fits give $z = 2.67 \pm 0.06$ using the starburst template and $z = 2.64 \pm 0.06$ using the obscured one. Both redshifts are in agreement with the latest optical results.

SMMJ10521+5719 The spectrum of this source shows PAH features plus a weak continuum. The source does not contain AGN features in the optical spectrum (Chapman et al. 2005). The mid-IR AGN continuum is detected but the feature-to-continuum ratio is much higher than in the cases of SMMJ02399–0136 and SMMJ09431+4700, thus suggesting a smaller AGN contribution. The presence of an AGN is confirmed as well from radio and X-ray emission that show the possible presence of a radio loud quasar (Ivison et al. 2002).

MMJ154127+6616 The mid-IR spectrum of this source was already published by Lutz et al. (2005a). We reprocessed the data using a later version of the IRS pipeline (14.0.0). The new reduction further increases the similarity to a starburst spectrum with well defined $6.2\mu\text{m}$ and $7.7\mu\text{m}$ PAH features and is well fitted by a M82 spectrum plus a very weak flat continuum. The χ^2 is not much worse adopting the NGC4418 template which better matches the emission at long wavelengths, but the clear presence of both PAH features strongly increases confidence that this source is powered by star formation.

SMMJ16369+4057 This source has the lowest redshift of the sample ($z = 1.21$) and is well fitted with the M82 spectrum plus a very weak flat continuum. The optical spectroscopy of Chapman et al. (2005) detects typical starburst lines, consistent with our result.

SMMJ16371+4053 The mid-IR spectrum of this source shows clear $6.2\mu\text{m}$ and $7.7\mu\text{m}$ PAH features. A flat continuum is detected. The mid-IR spectrum shows that it is powered mainly by starburst activity, even though an AGN is probably also present. AGN lines have been detected in the optical spectrum of Chapman et al. (2005).

IRS non-detections The sources for which we have neither detected features nor continua in the IRS spectra despite accurate interferometric positions are MMJ120517–0743.1, MMJ120539–0745.4, MMJ120546–0741.5 and MMJ154127+6615. Multiple arguments support the reality of these mm sources: they are well detected in the original MAMBO data (Bertoldi et al. 2000; Dannerbauer et al. 2002, 2004), are confirmed by SCUBA (Eales et al. 2003), have weak VLA counterparts (Bertoldi et al. 2000; Dannerbauer et al. 2004) and have dust continuum emission directly confirmed and located by mm interferometry (Dannerbauer et al. 2002, 2004; Dannerbauer 2004). The faintness or non-detection of their optical/near infrared counterparts (see also Table 3) lead these authors to the conclusion that these sources must be at very high redshift and/or highly obscured.

We now consider each of these scenarios in turn. If the IRS non-detections are intrinsically similar to the detected sources but simply more distant, we can place one lower limit on their redshifts by requiring that the $7.7 - 8.6\mu\text{m}$ PAH complex or the $8\mu\text{m}$ maxima in any absorbed spectra have remained undetected because they were shifted to wavelengths longer than $\sim 35\mu\text{m}$, where the detector sensitivity falls rapidly and the noise increases. This argument implies redshifts greater than 3.6. Similarly, since $6.2\mu\text{m}$ features in PAH emission spectra would already be lost in the noise at wavelengths longer than $\sim 30\mu\text{m}$ (being somewhat weaker), such sources could only be IRS non-detections for $z > 3.8$. Hence, we would conclude for all undetected sources redshifts $\gtrsim 3.6$.

3 SMGs: redshifts and other properties from mid-IR spectroscopy

If the IRS non-detections lie at redshifts similar to those of the IRS detections, their SEDs must be significantly different. We infer in Section 5.2 below that the detected sources already have a ratio of mid-IR PAH to far-IR emission similar to that of local ULIRGs. This implies that to escape IRS detection at the same redshifts, the non-detections would need to be even more heavily obscured in the mid-IR than local ULIRGs. By way of example, consider Arp 220, well known for its extremely low ratio of mid- to far-IR emission (e.g. Sanders et al. 1988; Haas et al. 2001). At $z \sim 2.5$, an extreme Arp 220-like SED scaled to the millimeter fluxes of the IRS non-detections would still manifest a broad PAH feature peaking at the 0.15 – 0.2 mJy level. No such feature is indicated in the spectra of the four non-detections (Fig. 3.1).

Previous assessments of the “higher redshift” and “higher obscuration” scenarios for these sources have been based on faint or undetected near-IR counterparts. For MMJ120517–0743.1, MMJ120539–0745.4, and MMJ120546–0741.5, faint K_s -band magnitudes and the assumption of SEDs similar to those of local ULIRGs imply very high redshifts $z \gtrsim 4$ (Dannerbauer et al. 2002). Similarly, the $K > 21.2$ counterpart of MMJ154127+6615 implies a redshift $z \gtrsim 3$. This particular argument is weakened by evidence that SMGs can have rest-frame *UV/optical* obscurations greater than those of local ULIRGs; SMMJ00266+1708, for example, has a very faint near-IR counterpart but (based on our data) $z = 2.73$. However, if we generalize the argument to the rest-frame *mid-infrared*, which is more difficult to obscure than the *UV/optical*, we are on stronger ground. Tellingly, our IRS non-detections are at least ~ 3 times fainter in the rest-frame mid-IR than even SMMJ00266+1708. This result is confirmed by the mid-IR imaging of Charmandaris et al. (2004), who place all four sources (three not detected and one tentatively detected) at the low end of the mid-IR to submm flux ratio distribution.

A further reason to prefer the “higher redshift” scenario for the IRS non-detections is that the radio counterparts to all four are faint, despite their bright mm fluxes (Bertoldi et al. 2000; Dannerbauer et al. 2004). The mean of their ratio of 850 μm and 1.4 GHz flux densities (212 ± 77) is about twice that of the Chapman et al. (2005) sample (95 ± 9), and still higher than both the value of 108 ± 9 , obtained for the same sample after exclusion of potentially radio-loud ($S_{1.4\text{GHz}} > 200 \mu\text{Jy}$) SMGs, and the value of 150 ± 20 , derived from a 15 sources subsample matching the mean SCUBA flux of our four non-detections. This trend is consistent with higher redshifts (Carilli & Yun 2000), although the scatter about the radio/submm vs. z relation is large. Taken together, the various lines of evidence suggest that the four IRS non-detections do lie at high redshift, although with all arguments still based on SED assumptions. Direct spectroscopic redshifts will be needed for a definitive conclusion.

3.5 Discussion

3.5.1 The redshift distribution has a median of $z \sim 2.8$

Figure 3.2 shows the redshift distribution for our sample. Taking into account the lower limits adopted for the undetected sources, we derive a median redshift of $z = 2.79$ for the full sample of 13 SMGs. The median redshift of the 9 detected sources is $z = 2.69$. These values are noticeably higher than the median $z = 2.2$ measured by Chapman et al. (2005) for their sample of 73 submillimeter galaxies with optical redshifts, and also higher than their estimate of $z = 2.3$ for the extrapolation to the full SMG population. None of our new IRS redshifts is in the optical “redshift gap” ($1.2 \lesssim z \lesssim 1.8$) of the optical spectroscopic census of the submillimeter galaxy population (Chapman et al. 2005), where some new IRS redshifts might have been expected. It is natural to assume that the optical redshifts are still biased towards the optically bright and low redshift part of the population (Dannerbauer et al. 2004). The recent discovery of a submillimeter galaxy at redshift $z \sim 4$ (Knudsen et al. 2006) similarly indicates an extension of the SMG redshift distribution beyond the one established by Chapman et al. (2005). In contrast, Pope et al. (2006) suggest from a combination of spectroscopic and photometric redshifts a median redshift of 2.0 for those SMGs in the HDF-North region that they consider securely identified through radio or *Spitzer* counterparts.

Our results suggest a modest extension of the Chapman et al. (2005) redshift distribution towards a larger high redshift tail, but the number statistics of our and other current SMG samples with redshifts is small. To investigate the significance of this difference, we have run simple Monte-Carlo simulations to estimate the probability of obtaining by chance a median redshift ≥ 2.79 for a 13 objects sample drawn randomly from a Chapman et al. (2005) redshift distribution. Using the distributions plotted in Fig. 4 of Chapman et al. (2005), this probability is a low 0.3% drawing 13-objects samples from their optical SMG redshift distribution with overall median 2.2, and a still interesting 8% for drawing from their suggested extrapolation to the overall SMG redshift distribution with median 2.3. The latter comparison is conservative in ignoring the fact that our sample with mostly *radio*-interferometric identifications is still biased against the very highest redshift objects.

In addition to these simple statistical comparisons, and perhaps more important, there can be effects of field-to-field variations including spikes in the redshift distribution for the current small area SMG surveys (Blain et al. 2004). A potential $z > 4$ redshift spike in the NDF region observed with MAMBO by Dannerbauer et al. (2004) from which three of our IRS non-detections are drawn, for example, could emphasize the high z component in our small sample. Likewise, the results of Pope et al. (2006) could have been driven in the opposite direction by being drawn from a single field. These constraints clearly call for further analyses using larger samples from large and widely separated fields.

3 SMGs: redshifts and other properties from mid-IR spectroscopy

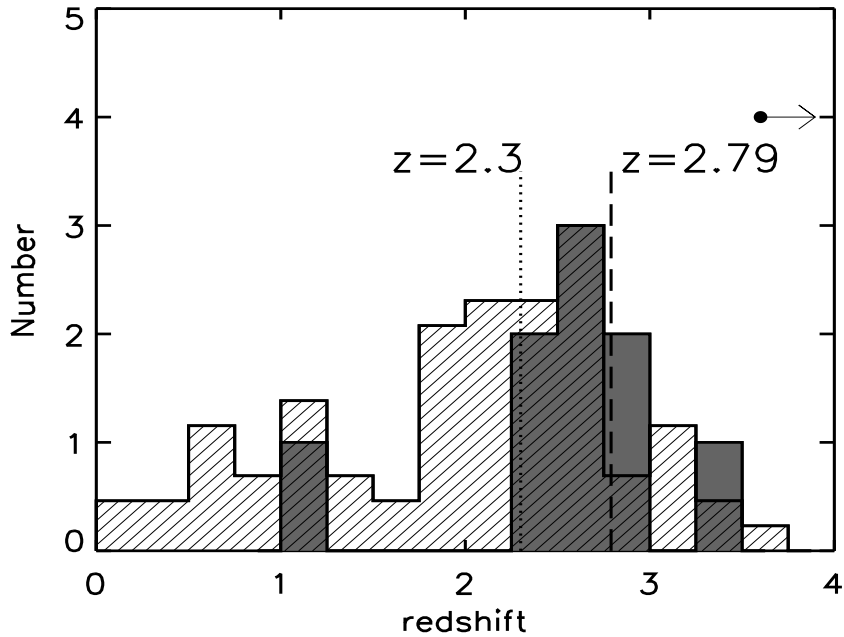


Figure 3.2: Histogram showing the redshift distribution for our SMG sample (solid) and for the submillimeter-flux-limited sample of Chapman et al. (2005) (cross-hatched), scaled for the maximum value. The dotted line at $z = 2.3$ indicates the median value obtained by Chapman et al. (2005) and the dashed line at $z = 2.79$ indicates the median of our sample distribution. Our value is calculated assuming $z \geq 3.6$ for undetected sources.

3.5.2 SMGs have ULIRG-like SEDs and are largely starburst-powered

The rest frame mid-IR spectra of SMGs and their comparison to the far-IR part of the SEDs hold interesting clues about their physical properties, energy sources and radiation fields. The average spectrum of the nine detected SMGs, individually scaled to the same rest wavelength flux $S_{222\mu\text{m}} = 15 \text{ mJy}$ to give all sources equal weight (see Fig. 3.3), clearly shows the PAH features at 6.2 and $7.7 \mu\text{m}$ but relatively weak continuum. The rest wavelength of $222 \mu\text{m}$ was chosen for this scaling because it is well constrained by observations, since it is the rest frame wavelength for the SCUBA $850 \mu\text{m}$ flux at redshift $z = 2.8$, about the median redshift of the sample. Scaling by the rest frame far-IR emission is close to scaling by bolometric flux, which is appropriate for interpreting the mid-IR diagnostics in Fig. 3.3 in terms of energy sources of a typical SMG without biasing towards star formation (PAH) or AGN (continuum). For galaxies at different redshifts, the rest frame $222 \mu\text{m}$ continuum emission was extrapolated from the SCUBA flux. For this step as well as in quantifying the bulk properties of our targets, we assign luminosities and temperatures following the approach of

Chapman et al. (2005) who use the local FIR/radio relation (Helou et al. 1985) to assign FIR SEDs to sources with known redshift, radio, and submm fluxes. The adopted far-IR SED model is a grey body with $S_{\nu,T} \propto k(\nu)B_{\nu,T}$ with $k(\nu) \propto \nu^\beta$ and $\beta = 1.5$. We calculated T_d for our galaxies using two photometric points (850 μm and 1.4 GHz) and the relation found by Chapman et al. (2005)

$$T_d \propto \frac{1+z}{(S_{850\mu\text{m}}/S_{1.4\text{GHz}})^{0.26}} \quad (3.1)$$

with a proportionality constant of 6.29 (see Tab. 3.3). Infrared luminosities are calculated as the integral between 8 and 1000 μm of the SED, assuming a ΛCDM cosmology with $H_0 = 70 \text{ km s}^{-1} \text{ Mpc}^{-1}$, $\Omega_M = 0.3$ and $\Omega_\Lambda = 0.7$ (see Tab. 3.3). Like other SMGs, our sample objects are inferred to be very luminous objects ($L_{\text{IR}} \sim 10^{13} L_\odot$).

The spectrum of Fig. 3.3 provides a first and direct indication that our sources are, on average, starburst-like (see also Menéndez-Delmestre et al. 2007, for a similar conclusion for several lower redshift SMGs). It can be seen as a superposition of a M82-type PAH spectrum and a weak additional continuum. Comparison with the spectra of the mostly starburst-dominated local ULIRG population (see e.g. Fig. 1 in Lutz et al. 1998) suggests that SMGs are scaled up versions of these objects. A further proof of this comes from a comparison of the ratio of PAH features and $S_{222\mu\text{m}}$ continua. Figure 3.4 shows the ratio of peak flux density of the 7.7 μm PAH feature, after continuum subtraction, to the continuum flux density at 222 μm rest frame for all the detected sources of our sample and for 11 local ULIRGs with PAH emission and good FIR photometry. The ULIRG data have been taken from ISOPHOT-S observations (Rigopoulou et al. 1999) and the continua from slight extrapolations of the far-IR photometry of Klaas et al. (2001), which extends to an observed wavelength of 200 μm . The PAH-to-far-infrared ratios of our sources are fully consistent with those of the local ULIRG population. These SED properties are in agreement with the conclusion, from spatially resolved mm interferometry, that SMGs are similar to local ULIRGs suitably scaled for their larger masses, luminosities and star formation rates, as well as their greater gas fractions (Tacconi et al. 2006).

Given this similarity of SMGs and local ULIRGs in the comparison between PAH and far-IR parts of the SED, it is instructive to also compare the dust temperatures for $z \approx 2.5$ SMGs with those of local galaxies. Chapman et al. (2005) infer $T_d \sim 36 \pm 7 \text{ K}$ for SMGs which can be compared to local galaxies in two ways: (1) SMGs have colder dust temperatures than local ULIRGs of the same luminosity (that means colder dust than so-called HyLIRGs). For local HyLIRGs, Chapman et al. (2003b) find $T_d \sim 42 \text{ K}$ at $L \sim 10^{13} L_\odot$. This could be due to their difference in energy sources: local HyLIRGs seem predominantly AGN driven (e.g. Tran et al. 2001), while many SMGs of the same luminosity are starbursts. (2) SMGs have similar dust temperatures to the bulk of the local ULIRG population which has luminosities just above $10^{12} L_\odot$. For local ULIRGs, Chapman et al. (2003a) infer $T_d \sim 36 \text{ K}$. This comparison is in line with other indications that SMGs are “scaled up” versions of such ULIRGs rather than direct analogs of local HyLIRGs.

3 SMGs: redshifts and other properties from mid-IR spectroscopy

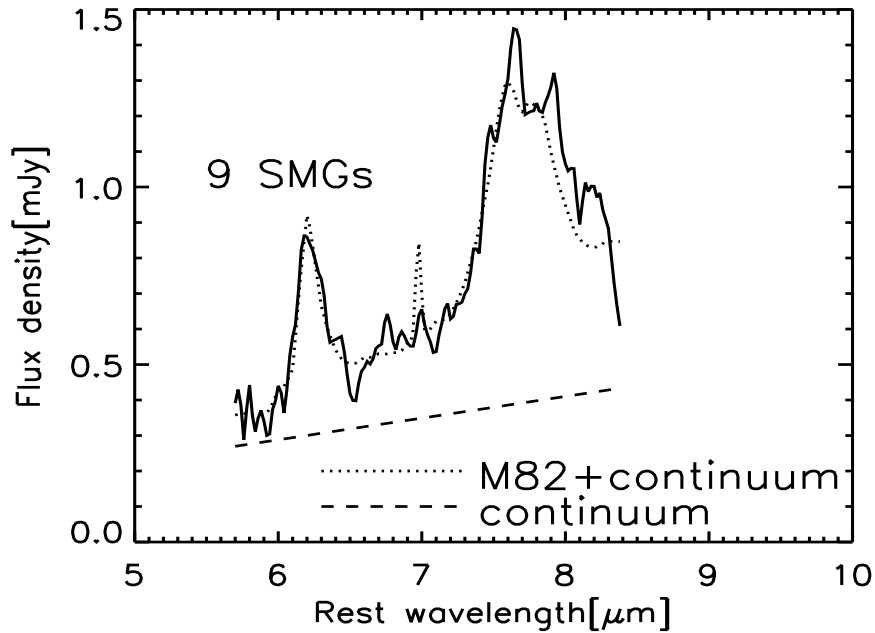


Figure 3.3: Average IRS spectrum of all 9 detected SMGs, individually scaled to $S_{222\mu\text{m}} = 15 \text{ mJy}$ in the rest wavelength. Both the $6.2\mu\text{m}$ and the $7.7\mu\text{m}$ PAH features are clearly visible. The spectrum is well fitted by the starburst-like spectrum of M82 plus a weak continuum.

From the rest frame mid-IR spectra it is possible to evaluate the presence and the strength of a possible AGN contribution to the very large infrared luminosity of the SMGs of our sample. Many SMGs show evidence of an AGN, from X-ray observations (Alexander et al. 2003, 2005a,b) or optical/near-IR spectra (e.g. Ivison et al. 1998; Swinbank et al. 2004; Chapman et al. 2005). However, the most important question is not whether there are detectable AGN signatures, but whether or not the AGN is a significant contributor to the luminosity of the galaxies. From our spectral decompositions, we can use the ratio of PAH $7.7\mu\text{m}$ peak and local continuum as an indicator of the AGN and star formation contribution to the bolometric luminosity. Following studies of local infrared galaxies (Genzel et al. 1998; Laurent et al. 2000; Tran et al. 2001), we adopt a feature to continuum ratio of 1 as the border between predominantly star formation and predominantly AGN powered². The fitted fluxes for the $7.7\mu\text{m}$ PAH peak and local continuum are listed in Table 3.3.

²Our decomposition by template fit differs from the one used by Genzel et al. (1998), which interpolates between two points in the observed spectrum to define the continuum, in approaching very high feature to continuum values in the limit of almost pure star formation. The two methods give very similar results in the presence of significant AGN continuum

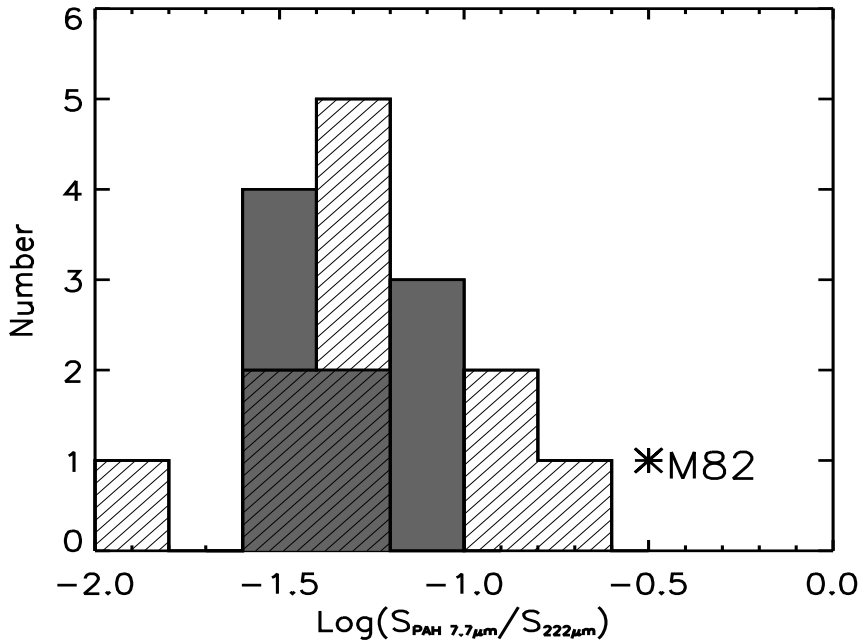


Figure 3.4: Histogram showing the ratio of PAH $7.7\mu\text{m}$ peak flux density and rest frame $222\mu\text{m}$ continuum flux density for our SMG sample (solid) and for eleven local ULIRGs (cross-hatched). In this measurement of the mid-to far-infrared SED, SMGs are very similar to the local ULIRG population. However, they show a lower value than the low luminosity starburst M82. The M82 point is based on the PAH data of Förster Schreiber et al. (2003) and the far-IR continuum of Colbert et al. (1999), obtained in large and similar apertures.

In our sample, there is no trace of an AGN continuum in the adopted fits to the rest frame mid-IR spectrum for two sources (SMMJ09429+4659 and SMMJ10519+5723). Seven sources (SMMJ00266+1708, SMMJ02399–0136, SMMJ09431+4700, SMMJ10521+5719, MMJ154127+6616, SMMJ16369+4057, SMMJ16371+4053) are well fitted by a superposition of an AGN continuum and PAH features. We note again that the alternative fit by an obscured (AGN?) continuum cannot be firmly excluded for one of these (SMMJ00266+1708). Assuming that a feature to continuum ratio of 1 means similar bolometric contribution from star formation and accretion, we conclude that, of these nine targets, two are pure starbursts with at best very weak AGN, five have AGN with modest contributions of the order 20%, and two (SMMJ02399–0136, SMMJ09431+4700) have strong AGN contributing slightly above half of the bolometric luminosity. We cannot constrain the starburst or AGN nature of the four undetected sources that are likely at high redshift, apart from stating that their non-detection means absence of a strong unobscured hot AGN continuum even for redshifts somewhat above 3.6. Our sample is small, so it seems rea-

3 SMGs: redshifts and other properties from mid-IR spectroscopy

sonable to expect that the full submillimeter population will show an even wider range of AGN properties perhaps including less obscured, energetically dominant AGNs. Egami et al. (2004) and Ivison et al. (2004) have used mid-IR photometry as a diagnostic tool to put limits on the AGN contribution to the infrared luminosity and agree that fewer than 25% of the SCUBA/MAMBO sources observed are AGN powered. From X-ray observations, Alexander et al. (2005b) found that, on average, the AGN contribution in a large sample of radio-detected SMGs was likely to be modest ($\simeq 10\%$). This result assumes that SMGs do not have a substantially larger dust-covering factor than optically selected quasars, and that there is no significant number of fully Compton-thick AGNs that are hard to detect in X-rays. Our finding of starbursts being prevalent in the mid-IR spectra extends this result by showing that SMGs typically do not contain such dominant X-ray obscured AGNs with strong mid-IR continuum re-emission. Obscured AGNs with strong mid-IR continuum are found in *Spitzer* mid-IR surveys (e.g. Martínez-Sansigre et al. 2005), but show only little overlap with the SMG population (Lutz et al. 2005b). In general it seems that the AGN contribution to the infrared luminosity of most SMGs is small when compared to heating from star-formation activity.

While the IRS spectra argue against dominant AGN being typical for SMGs, they can still help to constrain the obscuration of the lesser AGN found, independent of whether sufficient photons are available for a detailed X-ray spectral analysis (Alexander et al. 2005b). From comparison to X-ray data, we have argued in the discussion of the individual sources for high X-ray obscuration of the two strongest AGN in our sample. For $z = 2.8$, a rest frame $6\mu\text{m}$ continuum of $\sim 0.1\text{ mJy}$ for the weaker AGN, and the relation of rest frame $2 - 10\text{ keV}$ flux and $6\mu\text{m}$ AGN continuum from Lutz et al. (2004), a rest frame $2 - 10\text{ keV}$ emission of $4 \times 10^{-15}\text{ erg s}^{-1}\text{ cm}^{-2}$ is expected for an unobscured AGN following this relation. This is in the sensitivity regime of current X-ray data in the corresponding observed frame band, and can constrain the obscuration of such “minor” AGN with the caveat that large samples are needed given the variations in intrinsic AGN SEDs and the corresponding significant scatter of the mid-IR/X-ray relation. We have used *Chandra* archival X-ray data to put limits on the observed frame $0.5 - 2\text{ keV}$ emission of SMMJ00266+1708 ($< 0.56 \times 10^{-15}\text{ erg s}^{-1}\text{ cm}^{-2}$) and MMJ154127+6616 ($< 0.16 \times 10^{-15}$). From *XMM-Newton* observations of SMMJ10521+5719 in the same soft band, a value of $0.16 \times 10^{-15}\text{ erg s}^{-1}\text{ cm}^{-2}$ is derived (Brunner et al., in prep.). These limits and fluxes imply that the rest frame $2 - 10\text{ keV}$ emission is lower than the extrapolation from the mid-IR continuum to unobscured X-rays. Noticeable X-ray obscuration may thus be found in many of the minor AGN in SMGs, in agreement with Alexander et al. (2005b).

Metallicity and dust-to-gas ratios in many high redshift galaxies are expected to be lower than at low redshift. Low metallicity systems show weaker mid-IR PAH emission bands (e.g. Engelbracht et al. 2005). In addition to differences in radiation fields, this is probably due to the fact that these galaxies are young and thus may lack the carbon-rich AGB stars required to form the PAH molecules. However, the enrichment will proceed once intense star formation activity is underway for a sufficient time, or if there has been preceding star formation. This

seems to be the case for SMGs. They show very clear PAH features as tracers of their intense starbursts. We can therefore assume that high metallicity is typical for the population of massive SMGs, consistent with the supersolar metallicity derived from nebular emission for SMM14011 (Tecza et al. 2004) and the roughly solar abundances in the SMG sample of Swinbank et al. (2004). In fact, because of the intense star formation, the metallicity of these systems should rapidly approach that of their likely present-day descendants: luminous elliptical galaxies (Swinbank et al. 2004). These observations and the scenario that SMGs evolve to ellipticals are in full agreement with the fossil record that the formation of the stars of local ellipticals must have happened rapidly and at high redshift (Thomas et al. 2005).

3.6 Conclusions

We have presented *Spitzer* mid-IR spectra of a sample of 13 submillimeter galaxies. For nine of them, we have unambiguous detections of PAH spectral features and/or mid-IR continua that allow us to constrain energy sources in these objects and to determine, in three cases for the first time, their redshifts.

The IRS detections alone have a median $z \sim 2.7$. If the four IRS non-detections lie at similar redshifts, their rest frame mid-IR obscurations would have to be even more extreme than those of local ULIRGs. More plausibly, the four IRS non-detections lie at higher redshifts (≥ 3.6), giving a median $z \sim 2.8$ for the full set of 13. Although our sample is small, this result may indicate an extension to higher redshift of the SMG redshift distribution relative to radio-preselected samples with optical redshifts.

In the majority of cases, the detection of PAH emission and the weakness of AGN continua indicate that these galaxies are mainly starburst-powered. This result agrees with previous X-ray, optical and SED studies that indicate only a small AGN contribution to the IR luminosity compared to heating from star-formation activity. Our work extends these studies by also constraining the role of highly obscured AGN.

The SED properties of our galaxies are in agreement with the SMGs being scaled-up versions of the compact star-forming regions in local ULIRGs.

The existence of star formation dominated systems at infrared luminosities in excess of $10^{13}L_{\odot}$ is unique to the high redshift universe. The presence of high luminosity starbursts in SMGs may be related to their higher gas fractions (Greve et al. 2005; Tacconi et al. 2006).

Mid-IR spectroscopy with IRS, together with ancillary observations from the optical through radio wavelengths, can play a central role in understanding the nature of submillimeter galaxies and can be a powerful tool for probing the earliest and most dramatic stage of the evolution of galaxies.

This work is based on observations made with the *Spitzer Space Telescope*, which is operated by the Jet Propulsion Laboratory, California Institute of Technology, under a contract with NASA. We thank the referee for thorough and helpful comments. The authors want to thank M.Brusa and V.Mainieri for help with X-ray data. E.V. would like to thank the

3 SMGs: redshifts and other properties from mid-IR spectroscopy

following people for helpful discussions and support during the work: M.Righi, F.Braglia, L.Conversi.

4

A backward evolution model for infrared surveys

Abstract

Empirical “backward” galaxy evolution models for infrared bright galaxies are constrained using multi-band infrared surveys. We developed a new Monte-Carlo algorithm for this task, implementing luminosity dependent distribution functions for the galaxies’ far-IR SED and for the AGN contribution, allowing for evolution of these quantities. A local far-IR luminosity function is adopted and evolved using power law parametrizations for possible luminosity and density evolutions. By attaching an appropriate SED to every source predicted by the model, the algorithm enables simultaneous comparisons with multiple surveys in a wide range of wavebands. The adopted SEDs take into account the contributions of both starbursts and AGN to the L_{TIR} , for the first time in a coherent treatment rather than separate AGN and star-forming populations. The quantification of this contribution, varying with L_{TIR} , is made locally using a large sample of LIRGs and ULIRGs for which the mid-IR spectra are available in the *Spitzer* archive. The relation shows also significant changes at high z . Constrained by data from the literature, our best-fit model adopts a very strong luminosity evolution, $L = L_0(1+z)^{3.4}$, up to $z = 2$ and a density evolution, $\rho = \rho_0(1+z)$, up to $z = 1$, for the population of infrared galaxies. At higher z , the evolution rates drop as $(1+z)^{-1}$ and $(1+z)^{-1.5}$ respectively. In order to reproduce both number counts and redshifts distributions from mid-IR to submillimeter wavelengths, it is necessary to introduce both an evolution in the AGN contribution and an evolution in the $L - T$ relation: clues of such evolutions have been already obtained in recent photometric and spectroscopic studies of submillimeter galaxies.

4.1 Introduction

The discovery of the cosmic infrared background (CIB) (see Hauser & Dwek 2001 for a review), together with recent deep cosmological surveys in the infrared (IR) and submillimeter bands, has opened new perspectives on our understanding of galaxy formation and evolution. The surprisingly high amount of energy contained in the CIB showed that it is crucial to probe its contributing galaxies to understand when and how the bulk of stars formed in the Universe. Thanks to the deep cosmological surveys carried out by ISO (Kessler et al. 1996, e.g. Aussel et al. 1999; Oliver et al. 2000), SCUBA (Holland et al. 1999, e.g. Hughes et al. 1998), MAMBO (Kreysa et al. 1998, e.g. Bertoldi et al. 2000) and *Spitzer* (Werner et al. 2004, e.g. Papovich et al. 2004; Frayer et al. 2006) it is now possible, to various degrees, to resolve the CIB into discrete sources. The source counts are high when compared to no-evolution or moderate-evolution models for infrared galaxies (Guiderdoni et al. 1998; Franceschini et al. 1998). The striking results of these surveys concerning the evolution of the infrared and submillimeter galaxy population, and the constraints from the measures of the CIB, make necessary the development of new models to explain the high rate of evolution of infrared galaxies.

The problem of describing the number distribution of galaxies in the Universe is usually tackled via one of two methods. In the first method, known as the *forward evolution* approach, the evolution is computed assuming some initial conditions of the physical processes of chemical evolution and photometric evolution of the stellar populations that heat the dust. The so-called *semi-analytical* approach combines these assumptions on chemical/photometric evolution of galaxies with modeling considering dissipative and non-dissipative processes affecting galaxy formation within dark matter halos (Baugh et al. 2006) and has provided a reasonable fit to the source counts in the infrared (Guiderdoni et al. 1998). Arguably, the *forward evolution* approach has the advantage of being based on a more fundamental set of assumptions. However the obvious disadvantage is the larger number of free/unknown parameters assumed in these models. Compared to other wavelengths, there is one further complication for forward modelling of infrared surveys. Even if global properties of the evolving galaxies like star formation rate or AGN activity are correctly modelled, additional assumptions about the dust content and structure of the galaxy have to be invoked to convert them into a prediction of the luminosity and spectral energy distribution of the re-emitted infrared radiation.

The alternative method, often called *backward evolution* approach, takes the observed, present day ($z = 0$) luminosity function (LF) and evolves it in luminosity and/or density back out to higher redshifts assuming some parametrization of the evolution (e.g. Pearson & Rowan-Robinson 1996; Xu et al. 2001). This method has the advantage of being both direct and relatively simple to implement. The disadvantage in the past was that the information on which the assumptions about evolution were made often came from IRAS or ISO data which extended out only to relatively low redshifts. Because of their simplicity, backward evolution models have traditionally played a strong role in the planning of new infrared surveys. A backward

evolution model fitting the main constraints provided by previous missions can be easily modified to predict the results of new missions and help in the first steps of interpreting their results. Thanks to the latest deep and comprehensive observations, the tools to constrain the *backward evolution* methodology to significantly higher redshifts are now available.

Very recently, several empirical approaches have been proposed to model the high rate of evolution of infrared galaxies, in particular to reproduce source counts of the mid-IR surveys made with *Spitzer* (e.g. Lagache et al. 2003, 2004; Gruppioni et al. 2005, Xu et al. 2008¹, Rowan-Robinson et al. 2008¹, Franceschini et al. 2008¹).

The “classical” backward evolution model starts from different populations of galaxies, typically cirrus, starburst, active galactic nuclei (AGN) and ultraluminous infrared galaxies (ULIRGs) (e.g. Rowan-Robinson 2001), or a subset of those. Each population is assigned a proper spectral energy distribution (SED) and a local luminosity function and evolved independently, assuming it has a proper cosmic evolution rate. This approach is based on hypotheses not always satisfied. First of all, the SEDs adopted for starburst galaxies usually are either represented by a single SED or come from a set of templates where a unique relation between temperature and luminosity is assumed. This aspect was already discussed by Chapman et al. (2003b): analyzing a sample of local infrared galaxies, they found that the luminosity-temperature ($L-T$) relation presents a significant spread and that some evolution of the relation with redshift cannot be excluded. Second, and perhaps more important, different populations of galaxies are not so distinct as assumed in the models: very often AGN and starbursts co-exist in the same object, can be predominant at different times depending of the evolution stage of the object itself and can influence each other (e.g. AGN feedback on star formation).

Backward evolution models based on single SEDs or the simple SED family approach described above have been quite successful in fitting the number counts from the IRAS and ISO missions, the first submillimeter counts, the global CIB level, and for making first predictions for *Spitzer* and *Herschel*. The number and quality of observed constraints is increasing, however, and already the first *Spitzer* results have led to on the spot modifications (c.f. the modified SEDs adopted by Lagache et al. 2004) that may either represent true improved knowledge or reflect our reaching the limitations of the simple assumptions made previously. Furthermore, questions gaining increased importance, like the co-existence of AGN and star-formation in infrared galaxies, cannot be addressed by this generation of models, not even in the simple sense of fitting existing data and extrapolating to new observations that is inherent to the backward evolution approach. The goal of this work is hence to take the next step and develop a backward evolution model that considers realistic spreads in far-infrared SEDs, in AGN contributions at different luminosities, and their possible evolution with redshift. To that end, we first have to describe the local situation that is the starting point of the backward evolution scenario.

Luminous (LIRGs: $10^{11} < L_{\text{TIR}} \equiv L_{8-1000\mu\text{m}} < 10^{12} L_{\odot}$) and ultraluminous (ULIRGs:

¹in preparation

4 A backward evolution model for infrared surveys

$L_{\text{TIR}} > 10^{12} L_{\odot}$) infrared galaxies (Sanders et al. 1988) have been studied extensively in the local Universe, for instance with the *Infrared Astronomical Satellite* (IRAS; e.g. Soifer et al. 1987; Saunders et al. 1990), the *Infrared Space Observatory* (ISO; e.g. Lutz et al. 1998; Genzel & Cesarsky 2000; Tran et al. 2001), and more recently, with the *Infrared Spectrograph* (IRS; Houck et al. 2004) on board of *Spitzer* (e.g. Weedman et al. 2005; Brandl et al. 2006; Armus et al. 2007; Desai et al. 2007). These galaxies exhibit a large range of properties in the mid-IR, some showing strong PAH emission features characteristic of powerful (up to $\approx 1000 M_{\odot} \text{yr}^{-1}$) star formation rates (e.g. Brandl et al. 2006; Smith et al. 2007), and all exhibiting a large range in $9.7 \mu\text{m}$ silicate absorption or emission strengths (e.g. Weedman et al. 2005; Desai et al. 2007; Imanishi et al. 2007). *Spitzer* IRS is now enabling the study of mid-IR spectra of infrared galaxies to much higher redshifts ($z \gtrsim 3$; Valiante et al. 2007 or Chapter 3). Although locally rare, infrared galaxies become an important population at high redshifts and account for an increasing fraction of the star-formation activity in the universe (Le Flocc’h et al. 2005). By studying their infrared properties, we are just starting to estimate the extent to which AGN and star-formation contribute to their infrared luminosities, and therefore determine a correct census of starbursts and AGN at epochs in the Universe when their luminosity density was at its maximum.

The local luminosity function of IR-bright galaxies can be described considering two different populations: normal galaxies, dominating the “low-luminosity” part of LF, and starburst galaxies, dominant in the “high-luminosity” part. The AGN contribution appears dominant only at very high luminosity ($L_{\text{TIR}} \gtrsim 2 \times 10^{12} L_{\odot}$). Nevertheless, a small fraction of the total infrared luminosity can be due to the presence of an active galactic nucleus even in star formation dominated cases, and vice versa (Genzel et al. 1998). There are several studies of the AGN content for luminous galaxies at ULIRG and HYLIRG (hyperluminous infrared galaxies, $L_{\text{TIR}} > 10^{13} L_{\odot}$) levels, both using X-ray (Franceschini et al. 2003; Teng et al. 2005) and mid-IR (e.g. Genzel et al. 1998; Lutz et al. 1998; Tran et al. 2001) emission, and it is generally believed that AGN are typically less important at lower infrared luminosities. Still missing is a comprehensive study including lower luminosities ($< 10^{12} L_{\odot}$), with the aim of quantifying the distribution of AGN luminosity respect to the infrared luminosity of the host and the fraction of infrared luminosity due to accretion. Such a study is made in the following section (see § 4.2).

This chapter is organized as follows: in the first part (§ 4.2), starting from an IRAS-based sample of LIRGs and ULIRGs observed with IRS, we derive local distribution functions for the AGN contribution at different infrared luminosities. Using a small sample of distant galaxies, we also try to explore this relation at higher z . In the second part (§ 4.3), we present a new model whose originality is to consider a single population of infrared galaxies, with a single local luminosity function. An SED including the contribution due to starbursts and AGN is associated to each source, according with the relations derived in the first part for local and distant objects. This model, besides reproducing existing source counts, redshift distributions and CIB intensity, is also able for the first time to quantify the contribution due to starbursts and/or AGN to the total infrared luminosity and how this contribution evolves

for different classes of luminosity.

4.2 The AGN contribution in local ULIRGs and LIRGs

In order to be useful for the backward modelling project outlined above, a local calibration of the distribution of AGN contributions at given infrared luminosity has to reach from the highest luminosities down to at least the low end of the LIRG regime ($10^{11}L_{\odot}$). Given the evidence for the major contribution of objects above this luminosity threshold to the CIB and to the cosmic star formation rate at $z \gtrsim 1$ (e.g. Elbaz et al. 2002; Pérez-González et al. 2005), covering this luminosity range is essential. Historically, many of the references cited above have focussed on the ULIRG ($> 10^{12}L_{\odot}$) regime and even its upper end where the AGN contribution is highest, while studies at lower luminosities mostly focussed on individual interesting objects. What is needed is a quantification of AGN content for an unbiased far-IR selected sample reaching down to $10^{11}L_{\odot}$. Of the two principle routes towards this observational goal, X-ray observations and mid-IR spectroscopy, we make use of the second for two reasons. First, there is not yet a full unbiased and deep X-ray dataset for such a sample available. There are XMM and Chandra data of depth required for good X-ray spectral analysis for many local LIRGs/ULIRGs, but still with a tendency to target known AGN. Second, since the implicit goal of our modelling effort is to characterize the AGN effect on the infrared SED, mid-IR data can provide useful constraints quite directly even when adopting simple analysis methods, while evidence from other wavelengths would have to go through a conversion to the mid-IR range, or even in two steps via the AGN bolometric power, a process that will be subject to the considerable scatter of AGN SEDs (see also § 4.2.2).

Our basic approach is to determine the distribution of AGN contributions for local LIRGs and ULIRGs from the IRAS Revised Bright Galaxy Sample (Sanders et al. 2003) for which archival Spitzer spectroscopic coverage is essentially complete. We adopt a simple quantification of the AGN contribution from the rest frame $6\mu\text{m}$ continuum which, while not making use of the full detail of the best S/N spectra, is applicable to the entire sample and allows for straightforward use in the later modelling. We also compare to X-ray results for part of the sample.

In mid-IR spectra of AGN, the $6\mu\text{m}$ flux after subtraction of the starbursts contribution ($f_{6\text{AGN}}$), is related to the nuclear activity, as indicated by the intrinsic hard X-ray flux (Lutz et al. 2004). Hard X-rays, unless extremely obscured in fully Compton-thick objects, can provide a direct view to the central activity, while the infrared continuum is due to AGN emission reprocessed by dust, either in the torus or on somewhat larger scales. The mid-IR continuum has the advantages of showing no significant differences between type 1 and type 2 AGN and of being a good tracer of nuclear activity even in those cases where hard X-rays are strongly absorbed. Low resolution mid-IR spectra of galaxies can be decomposed into three components (Laurent et al. 2000): a component dominated by the aromatic “PAH” features arising from photodissociation regions or from the diffuse interstellar medium of the

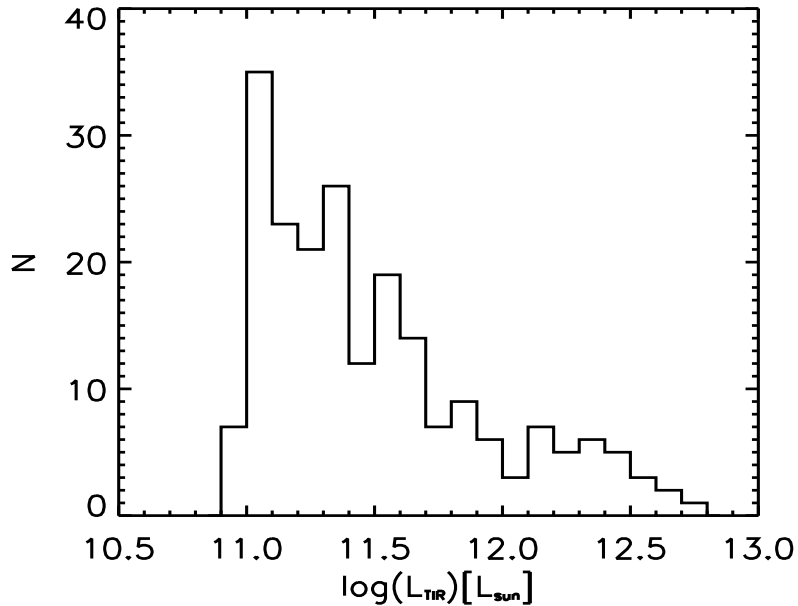


Figure 4.1: Total infrared luminosity distribution of the galaxies of our sample, including galaxies from RBGS catalog (Sanders et al. 2003) and sources from Tran et al. (2001).

host, a continuum rising steeply toward wavelengths beyond $10\mu\text{m}$ due to HII regions and a typically flatter thermal AGN dust continuum present in active galaxies.

In the range covered by the low resolution modules of IRS (SL1 and SL2, from ~ 5 to $\sim 14\mu\text{m}$ as described in Houck et al. 2004), the AGN emission is most easily isolated shortwards of the complex of aromatic emission features (Laurent et al. 2000). We determine the continuum at $6\mu\text{m}$ rest wavelength and eliminate non-AGN emission by subtracting a star formation template scaled with the strength of the aromatic “PAH” features arising from the host or from circumnuclear star formation. This method does not require to spatially resolve the AGN from the host and, thanks to the high sensitivity of IRS, allows also the detection of a weak AGN in the presence of strong star formation in many nearby galaxies.

4.2.1 Sample selection and data reduction

The starting point for this study is the IRAS Revised Bright Galaxy Sample (RBGS), a complete flux-limited survey of all extragalactic objects with $60\mu\text{m}$ flux $f_{60} > 5.24\text{Jy}$ (Sanders et al. 2003). The galaxies with $L_{\text{TIR}} > 10^{11} L_{\odot}$ were selected from this sample and the mid-IR IRS data were obtained from the *Spitzer* archive for all of the them, with the exception of 6

4.2 The AGN contribution in local ULIRGs and LIRGs

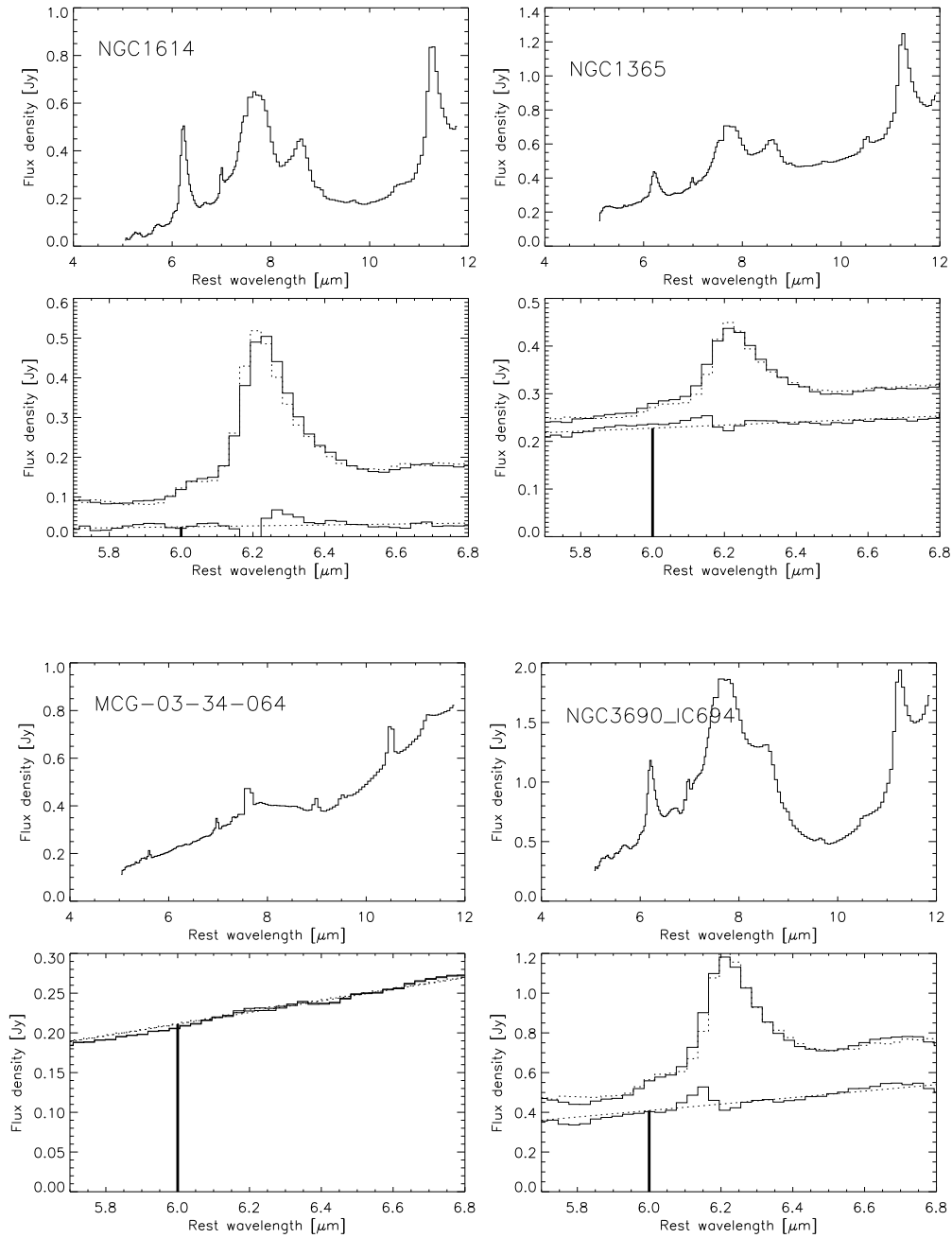


Figure 4.2: Examples for the decomposition used to isolate the AGN continuum. *Top panels:* *Spitzer* IRS low resolution spectra of four representative galaxies. *Bottom panels:* Cutout of the region around the $6.2\mu\text{m}$ PAH feature. Top continuous line = observed spectrum. Top dotted line = fit by the sum of the M82 spectrum and a linear AGN continuum. Bottom dotted line = fitted AGN continuum. Bottom continuous line = difference of observed spectrum and fitted PAH component. The thick vertical line indicates $\tilde{f}_{6\text{AGN}}$.

4 A backward evolution model for infrared surveys

sources that were not yet observed or for which there were no observation programs at all. Most of our observations have been obtained within the observational program PID 30323 (PI L.Armus)

Because of the limit in flux, this sample misses the most luminous infrared galaxies that are rare in the local universe. In fact, it does not include any galaxy with $L > 10^{12.5} L_{\odot}$, excluding all HYLIRGs, for example, from the analysis. In order to enlarge our range in luminosity, in particular including representatives of the most luminous tail of the local galaxy population, we added 14 galaxies from the sample of 16 by Tran et al. (2001). These latter galaxies were selected from surveys at different limits in f_{60} and with a preference for high-luminosity targets. They do not introduce any bias in mid-IR spectral properties or AGN content. In particular, no AGN-related IRAS color criteria, like the f_{25}/f_{60} ratio, were applied in the selection.

The total sample includes 211 sources spanning a luminosity range $10^{10.9} \leq L_{\text{TIR}} \leq 10^{12.8} L_{\odot}$ (see Fig. 4.1 and Tab. 4.1).

We reduced the data as follows. We subtracted, for each cycle, the two nod positions of the pipeline 15.3.0 basic calibrated data frames. In the difference just calculated, we replaced deviant pixels by values representative of their spectral neighborhoods. We subtracted residual wavelength dependent background, measured in source-free regions of the two dimensional difference spectra. In averaging all the cycles of the 2-dimensional subtracted frames, we excluded values more than three times the local noise away from the mean. The calibrated 1-dimensional spectra for the positive and the negative beams were extracted and the two 1-dimensional spectra averaged in order to obtain the final spectrum, using the SMART analysis package (Higdon et al. 2004).

We derive $f_{6\text{AGN}}$ by a decomposition over a range from $5.5 \mu\text{m}$ to $6.85 \mu\text{m}$ rest wavelength. We fit the spectrum by the superposition of a star formation component dominated by the $6.2 \mu\text{m}$ PAH feature (M82 spectrum by Sturm et al. 2000) and a simple linear approximation of the AGN continuum. Fig. 4.2 shows the decomposition of the spectrum for sources with different nature: NGC1614 is a pure starburst, NGC1365 is classified as a Seyfert 1.8 from its optical spectrum, has a Compton-thin AGN observed in the X-ray emission (Risaliti et al. 2000) but shows also PAH features in the mid-IR spectrum, MCG-03-34-064 has a typical AGN-dominated mid-IR spectrum and the galaxy pair NGC3690/IC694 (Arp299) is classified as Compton-thick AGN from its X-ray spectrum (Della Ceca et al. 2002) and its mid-IR spectrum reveals that the nuclear activity is quite high but coincident with strong star formation.

The results of the fit procedure are $\tilde{f}_{6\text{AGN}}$, represented in Fig. 4.2 by the thick vertical line, and $\tilde{f}_{6.2\text{peakSB}}$, an average flux density of the PAH component over the rest wavelength range 6.1 to $6.35 \mu\text{m}$ (see Tab. 4.1). The spectrum of M82 is well suited for this decomposition but represents just a single object that may not be fully representative for star forming objects in general. In order to take into account the dispersion among star-forming objects in relative importance of all the components of the model of Laurent et al. (2000), we apply to the results of our fit the correction calculated by Lutz et al. (2004). This correction is derived

4.2 The AGN contribution in local ULIRGs and LIRGs

from applying the same M82-based decomposition to a small sample of 11 star-forming objects. The values $f_{6\text{AGN}}$ used for the further analysis (see Tab. 4.1) are obtained after subtracting $0.096 \times \tilde{f}_{6.2\text{peakSB}}$ from the direct fit results $\tilde{f}_{6\text{AGN}}$. Error estimates for $f_{6\text{AGN}}$ are the quadratic sum of two components. The first is a measurement error based on individual pixel noise derived from the dispersion in the difference of observation and fit. The second is $0.085 \times \tilde{f}_{6.2\text{peakSB}}$, thus considering the dispersion in the properties of the comparison star forming galaxies.

4 A backward evolution model for infrared surveys

Table 4.1. Full sample of infrared galaxies: results of the fit and corrected $f_{6\text{AGN}}$ fluxes

Name	z	$\log(L_{\text{TIR}})$ L_{\odot}	$\tilde{f}_{6\text{AGN}}$ mJy	$\tilde{f}_{6.2\text{peakSB}}$ mJy	$f_{6\text{AGN}}$ mJy
Sources from RBGS catalog (Sanders et al. 2003)					
NGC0023	0.015	11.05	13.9±1.0	132.7±1.8	<23.8
NGC0034	0.020	11.44	48.8±3.1	182.2±5.7	<62.9
MCG-02-01-051/2	0.027	11.41	6.8±0.8	116.4±1.5	<19.9
ESO350-IG038	0.021	11.22	57.8±0.5	46.2±0.8	53.4±4.0
NGC0232	0.020	11.30	20.5±1.5	144.4±2.6	<31.4
MCG+12-02-001	0.016	11.44	20.5±1.7	284.2±3.2	<48.4
NGC0317B	0.018	11.11	14.6±0.7	121.4±1.3	<23.6
IC1623A/B	0.020	11.65	196.4±2.5	358.2±4.5	162.0±30.5
MCG-03-04-014	0.035	11.63	8.3±0.7	141.8±1.3	<24.1
ESO244-G012	0.023	11.39	12.6±1.3	201.4±2.3	<34.3
CGCG436-030	0.031	11.63	35.8±0.6	96.5±1.1	26.5±8.2
ESO353-G020	0.016	11.00	20.2±1.1	132.5±2.0	<30.1
ESO297-G011/012	0.017	11.09	16.0±1.1	182.5±2.0	<31.1
IRASF01364-1042	0.048	11.76	4.0±0.2	16.1±0.4	<5.2
III Zw035	0.028	11.56	2.1±0.1	8.1±0.2	<2.7
NGC0695	0.033	11.63	5.5±0.5	79.0±0.9	<13.5
UGC01385	0.019	10.99	7.1±0.7	96.8±1.3	<16.5
NGC0828	0.018	11.31	17.3±1.1	159.9±2.0	<29.2
NGC0838	0.013	11.00	5.6±1.5	210.8±2.7	<36.0
IC0214	0.030	11.37	3.9±0.5	67.8±0.8	<11.6
NGC0877	0.013	11.04	3.7±0.1	4.3±0.2	3.3±0.4
UGC01845	0.016	11.07	25.2±2.0	230.6±3.6	<42.5
NGC0958	0.020	11.17	5.0±0.1	6.4±0.2	4.4±0.6
NGC0992	0.014	11.02	5.0±1.0	161.7±1.9	<27.6
NGC1068	0.003	11.27	10493.6±30.6	120.5±55.8	10482.0±32.3
UGC02238	0.021	11.26	16.4±1.4	210.8±2.5	<35.9
IRASF02437+2122	0.023	11.11	18.3±0.4	26.4±0.6	15.8±2.3
UGC02369	0.031	11.60	9.3±0.6	80.5±1.1	<15.3
UGC02608	0.023	11.35	67.0±1.1	72.4±1.9	60.0±6.3
NGC1275	0.018	11.20	120.2±0.8	5.7±1.5	119.7±0.9
IRASF03217+4022	0.023	11.28	12.9±0.9	79.3±1.6	<18.9
NGC1365	0.005	11.00	227.8±1.7	144.7±3.1	213.9±12.4
IRASF03359+1523	0.035	11.47	0.4±0.1	3.7±0.2	<0.7
CGCG465-012	0.022	11.15	6.3±0.5	71.6±0.9	<12.2
IRAS03582+6012	0.030	11.37	189.7±1.5	10.5±2.7	188.7±1.7
UGC02982	0.017	11.13	6.0±0.8	113.8±1.4	<19.4
ESO420-G013	0.012	11.02	86.6±1.1	177.8±1.9	69.5±15.2
NGC1572	0.020	11.24	18.6±0.6	84.7±1.1	<24.9
IRAS04271+3849	0.019	11.06	9.3±0.7	125.5±1.3	<21.4
NGC1614	0.016	11.60	24.8±2.9	331.6±5.3	<56.7

4.2 The AGN contribution in local ULIRGs and LIRGs

Table 4.1

Name	z	$\log(L_{\text{TIR}})$ L_{\odot}	$\tilde{f}_{6\text{AGN}}$ mJy	$\tilde{f}_{6.2\text{peakSB}}$ mJy	$f_{6\text{AGN}}$ mJy
UGC03094	0.025	11.35	21.2±0.5	80.3±0.9	<27.2
ESO203-IG001	0.053	11.79	12.9±0.4	2.8±0.8	12.6±0.5
MCG-05-12-006	0.019	11.12	13.9±0.5	85.5±0.8	<20.3
NGC1797	0.015	11.00	12.8±0.9	145.3±1.7	<24.8
CGCG468-002	0.017	11.10	41.1±0.6	76.2±1.0	33.8±6.5
VII Zw031	0.054	11.94	8.5±0.7	123.0±1.2	<21.0
IRAS05083+2441	0.023	11.21	5.1±0.9	165.8±1.7	<28.2
IRAS05129+5128	0.027	11.36	11.4±0.4	82.1±0.8	<17.5
IRASF05187-1017	0.028	11.23	6.2±0.3	31.3±0.6	<8.5
IRASF05189-2524	0.043	12.11	204.8±0.9	36.6±1.6	201.3±3.2
IRAS05223+1908	0.030	11.59	367.8±1.1	11.7±2.0	366.7±1.5
NGC1961	0.013	11.02	8.6±0.3	8.8±0.6	7.8±0.8
MCG+08-11-002	0.019	11.41	26.3±1.1	165.4±2.0	<38.6
UGC03351	0.015	11.22	22.3±0.9	126.7±1.6	<31.8
IRAS05442+1732	0.019	11.25	13.0±1.5	194.7±2.7	<33.2
UGC03410	0.013	11.04	5.2±0.5	66.1±0.8	<11.3
IRASF06076-2139	0.037	11.59	9.7±0.3	26.6±0.5	7.1±2.3
NGC2146	0.003	11.07	45.6±6.2	881.1±11.3	<150.3
ESO255-IG007	0.039	11.84	11.7±1.3	214.5±2.4	<36.6
ESO557-G002	0.021	11.19	5.3±0.3	49.2±0.6	<9.0
UGC3608	0.022	11.30	8.0±0.4	59.1±0.7	<12.4
IRASF06592-6313	0.023	11.17	11.7±0.5	64.8±0.9	<16.5
AM0702-601	0.031	11.58	100.2±0.4	22.5±0.8	98.0±2.0
NGC2342	0.018	11.25	5.6±0.4	67.5±0.8	<11.5
NGC2369	0.011	11.10	30.0±1.4	166.9±2.6	<42.5
IRAS07251-0248	0.088	12.32	16.4±1.1	4.7±2.1	15.9±1.2
NGC2388	0.014	11.23	22.0±1.1	168.3±2.1	<34.5
MCG+02-20-003	0.016	11.08	53.4±1.7	74.7±3.0	46.2±6.6
IRASF08339+6517	0.019	11.05	2.9±0.8	92.0±1.4	<15.7
NGC2623	0.018	11.54	22.3±0.8	86.2±1.4	<28.8
IRAS08355-4944	0.026	11.56	78.7±0.6	100.2±1.1	69.1±8.5
ESO432-IG006	0.016	11.02	18.7±1.0	135.5±1.8	<28.8
ESO60-IG016	0.046	11.76	56.4±0.6	35.3±1.1	53.0±3.1
IRASF08572+3915	0.058	12.10	291.5±2.9	10.8±5.4	290.5±3.0
IRAS09022-3615	0.060	12.26	83.2±0.5	76.3±0.9	75.9±6.5
IRASF09111-1007	0.054	12.00	5.8±0.3	35.3±0.5	<8.4
UGC04881	0.040	11.69	9.0±0.3	62.3±0.6	<13.6
UGC05101	0.039	11.95	46.7±1.0	66.9±1.6	40.3±5.8
MCG+08-18-013	0.026	11.28	0.3±0.1	1.5±0.2	<0.3
IC0563/4	0.020	11.19	6.0±0.4	54.0±0.8	<10.0
NGC3110	0.017	11.31	9.1±0.7	123.5±1.3	<21.0

4 A backward evolution model for infrared surveys

Table 4.1

Name	z	$\log(L_{\text{TIR}})$ L_{\odot}	$\tilde{f}_{6\text{AGN}}$ mJy	$\tilde{f}_{6.2\text{peakSB}}$ mJy	$f_{6\text{AGN}}$ mJy
IC2545	0.034	11.73	311.7±6.2	30.6±11.3	308.8±6.7
IRASF10173+0828	0.049	11.80	2.1±0.1	6.0±0.2	1.5±0.5
NGC3221	0.013	11.00	0.5±0.2	34.8±0.4	<5.9
NGC3256	0.009	11.56	66.1±3.1	581.7±5.7	<109.3
ESO264-G036	0.023	11.35	10.6±1.0	38.3±1.7	6.9±3.4
IRASF10565+2448	0.043	12.02	16.6±0.6	108.9±1.1	<24.7
ESO264-G057	0.017	11.08	7.3±0.5	76.4±0.9	<13.0
MCG+07-23-019	0.035	11.61	0.7±0.1	8.7±0.2	<1.5
CGCG011-076	0.025	11.37	29.9±0.8	102.8±1.4	20.0±8.8
IC2810	0.034	11.59	5.9±0.3	43.2±0.5	<9.1
ESO319-G022	0.016	11.04	9.4±0.3	31.4±0.5	6.4±2.7
NGC3690/IC694	0.011	11.88	409.0±5.6	519.4±10.2	359.1±44.5
ESO320-G030	0.011	11.10	24.1±1.2	150.1±2.2	<35.3
ESO440-IG058	0.023	11.36	10.3±0.8	123.8±1.4	<21.1
IRASF12112+0305	0.073	12.28	4.6±0.4	29.7±0.6	<6.9
ESO267-G030	0.018	11.19	14.1±0.7	90.4±1.4	<20.9
NGC4194	0.009	11.06	50.2±3.1	366.2±5.7	<77.6
IRAS12116-5615	0.027	11.59	42.3±0.8	135.6±1.5	29.3±11.6
IRASF12224-0624	0.026	11.27	6.2±0.3	1.5±0.5	6.1±0.3
NGC4418	0.007	11.08	202.3±12.1	44.0±22.0	198.1±12.7
UGC08058	0.042	12.51	670.0±2.8	43.1±5.1	665.9±4.6
NGC4922	0.024	11.32	43.6±0.5	42.1±0.9	39.6±3.6
CGCG043-099	0.037	11.62	9.3±0.4	77.7±0.8	<15.1
MCG-02-33-098/9	0.016	11.11	12.0±0.9	135.7±1.7	<23.1
ESO507-G070	0.022	11.49	13.6±0.7	89.4±1.3	<20.3
IRAS13052-5711	0.021	11.34	7.1±0.4	72.0±0.7	<12.5
NGC5010	0.021	11.50	29.2±4.6	65.9±8.2	22.9±7.2
IRAS13120-5453	0.031	12.26	45.3±1.4	200.0±2.5	<60.2
IC0860	0.013	11.17	6.4±0.2	20.6±0.4	4.4±1.8
VV250a	0.031	11.74	14.1±1.1	144.6±2.0	<24.9
UGC08387	0.023	11.67	19.5±0.9	177.2±1.6	<32.7
NGC5104	0.019	11.20	16.1±0.8	98.1±1.5	<23.4
MCG-03-34-064	0.017	11.24	211.0±1.3	7.0±2.4	210.3±1.4
NGC5135	0.014	11.17	33.8±1.8	149.9±3.2	<45.1
ESO173-G015	0.010	11.34	62.4±2.6	302.2±4.7	<85.0
IC4280	0.016	11.08	6.5±0.5	57.5±0.9	<10.8
NGC5256	0.028	11.49	14.0±0.5	109.0±1.0	<22.1
NGC5257/8	0.023	11.55	5.3±0.3	39.4±0.6	<8.2
UGC08696	0.038	12.14	52.1±1.8	57.7±2.8	46.6±5.2
UGC08739	0.017	11.08	9.8±0.5	49.7±0.9	<13.5
ESO221-IG010	0.010	11.17	7.7±0.9	114.2±1.6	<19.5

4.2 The AGN contribution in local ULIRGs and LIRGs

Table 4.1

Name	z	$\log(L_{\text{TIR}})$ L_{\odot}	$\tilde{f}_{6\text{AGN}}$ mJy	$\tilde{f}_{6.2\text{peakSB}}$ mJy	$f_{6\text{AGN}}$ mJy
NGC5331	0.033	11.59	6.4±0.4	68.5±0.7	<11.7
NGC5394/5	0.012	11.00	14.3±1.2	123.4±2.2	<23.6
CGCG247-020	0.026	11.32	10.3±0.5	82.2±0.9	<16.4
NGC5653	0.012	11.06	7.4±0.5	63.9±0.9	<12.2
IRASF14348-1447	0.082	12.30	7.4±0.4	22.9±0.6	5.2±2.0
IRASF14378-3651	0.068	12.15	6.1±0.4	24.9±0.7	<8.0
NGC5734	0.014	11.06	12.8±0.6	58.8±1.0	<17.2
VV340a	0.033	11.67	13.4±0.6	93.9±1.2	<20.4
VV705	0.041	11.89	1.9±0.3	14.5±0.5	<3.0
ESO099-G004	0.029	11.67	15.3±0.5	101.7±0.9	<22.9
IRASF15250+3608	0.055	12.02	35.6±2.5	12.2±4.0	34.4±2.7
NGC5936	0.013	11.07	11.8±0.9	126.5±1.7	<21.6
UGC09913	0.018	12.21	44.7±1.9	102.0±3.0	34.9±8.9
NGC5990	0.013	11.06	97.2±0.5	76.3±0.9	89.9±6.5
NGC6052	0.016	11.02	3.6±0.9	60.6±1.7	<10.5
NGC6090	0.030	11.51	1.5±0.4	47.3±0.8	<8.1
IRASF16164-0746	0.027	11.55	17.3±2.2	94.7±3.9	<24.9
CGCG052-037	0.024	11.38	10.5±0.7	134.0±1.3	<22.8
NGC6156	0.011	11.07	16.0±0.3	37.6±0.6	12.4±3.2
ESO069-IG006	0.046	11.92	12.4±1.4	168.6±2.6	<28.8
IRASF16399-0937	0.027	11.56	13.5±0.4	40.0±0.7	9.7±3.4
ESO453-G005	0.021	11.29	3.6±0.2	20.2±0.3	<5.1
NGC6240	0.024	11.85	73.5±3.5	167.4±6.5	57.4±14.7
IRASF16516-0948	0.023	11.24	1.7±0.3	49.7±0.6	<8.5
NGC6286	0.019	11.32	14.3±0.6	104.3±1.1	<22.1
IRASF17132+5313	0.051	11.89	3.1±0.2	23.1±0.4	<4.8
IRASF17138-1017	0.017	11.42	5.9±0.9	59.4±1.7	<10.5
IRASF17207-0014	0.043	12.39	19.6±1.1	103.2±1.7	<27.4
ESO138-G027	0.021	11.34	12.2±0.4	70.5±0.7	<17.4
UGC11041	0.016	11.04	8.2±0.6	82.0±1.1	<14.3
CGCG141-034	0.020	11.13	12.5±0.5	72.0±0.8	<17.9
IRAS17578-0400	0.013	11.35	8.9±0.7	111.9±1.3	<19.1
IRAS18090+0130	0.029	11.58	8.5±0.6	103.5±1.0	<17.6
NGC6621	0.021	11.23	8.9±0.6	75.8±1.2	<14.6
CGCG142-034	0.019	11.11	9.6±0.4	50.4±0.7	<13.4
IRASF18293-3413	0.018	11.81	41.1±2.8	507.7±5.1	<86.5
NGC6670A/B	0.029	11.60	9.6±0.6	125.0±1.1	<21.3
IC4734	0.016	11.30	20.2±0.8	111.7±1.5	<28.5
NGC6701	0.013	11.05	16.9±1.0	122.1±1.7	<26.0
ESO593-IG008	0.049	11.87	7.1±0.5	69.5±0.9	<12.3
NGC6786/UGC11415	0.025	11.43	22.1±0.7	94.1±1.3	<29.1

4 A backward evolution model for infrared surveys

Table 4.1

Name	z	$\log(L_{\text{TIR}})$ L_{\odot}	$\tilde{f}_{6\text{AGN}}$ mJy	$\tilde{f}_{6.2\text{peakSB}}$ mJy	$f_{6\text{AGN}}$ mJy
IRASF19297-0406	0.086	12.37	7.7±0.4	29.4±0.8	<9.9
IRAS19542+1110	0.065	12.04	11.1±0.4	18.3±0.7	9.3±1.6
ESO339-G011	0.019	11.12	28.5±0.6	52.3±1.0	23.5±4.5
NGC6907	0.011	11.03	7.5±0.6	73.6±1.0	<13.0
MCG+04-48-002	0.014	11.06	22.6±1.0	158.0±1.8	<34.4
NGC6926	0.020	11.26	5.3±0.1	4.0±0.2	4.9±0.4
IRAS20351+2521	0.034	11.54	5.0±0.5	62.6±1.0	<10.7
CGCG448-020	0.036	11.87	20.2±0.5	61.7±0.8	14.3±5.3
ESO286-IG019	0.043	12.00	39.5±1.0	23.1±1.8	37.3±2.2
ESO286-G035	0.017	11.13	8.1±0.8	138.4±1.5	<23.6
IRAS21101+5810	0.039	11.75	5.6±0.3	48.9±0.5	<9.2
ESO343-IG013	0.019	11.07	12.9±0.5	91.0±1.0	<19.7
NGC7130	0.016	11.35	33.4±0.5	67.1±1.0	27.0±5.7
ESO467-G027	0.018	11.02	3.3±0.3	41.0±0.5	<7.0
ESO602-G025	0.025	11.27	29.9±0.7	140.0±1.2	<40.3
UGC12150	0.021	11.29	17.5±0.8	109.7±1.5	<25.7
ESO239-IG002	0.043	11.78	10.2±0.3	39.6±0.5	<13.2
IRASF22491-1808	0.077	12.11	3.3±0.2	16.1±0.3	<4.5
NGC7469	0.016	11.59	171.8±1.9	261.1±3.5	146.7±22.3
CGCG453-062	0.025	11.31	6.0±0.3	48.4±0.5	<9.6
ESO148-IG002	0.045	12.00	24.7±0.4	58.0±0.7	19.1±4.9
NGC7552	0.005	11.03	114.9±3.5	564.4±6.3	<156.9
IC5298	0.027	11.54	44.1±1.7	40.8±3.1	40.2±3.9
NGC7591	0.017	11.05	12.2±0.5	56.9±0.8	<16.5
NGC7592	0.024	11.33	28.4±0.6	126.1±1.2	<37.8
ESO077-IG014	0.042	11.70	11.2±0.6	70.3±1.0	<16.5
NGC7674	0.029	11.50	138.5±1.2	16.0±2.1	137.0±1.8
NGC7679	0.017	11.05	13.6±1.2	145.1±2.1	<24.8
IRASF23365+3604	0.064	12.13	5.1±0.3	17.0±0.5	3.5±1.5
MCG-01-60-022	0.023	11.21	5.3±0.5	75.2±0.8	<12.8
IRAS23436+5257	0.034	11.51	11.4±0.3	35.1±0.5	8.0±3.0
NGC7752/3	0.017	11.01	5.3±0.4	55.8±0.7	<9.5
NGC7771	0.014	11.34	17.8±1.0	120.2±1.8	<26.8
MRK0331	0.018	11.41	22.3±1.5	275.3±2.7	<46.9

Sources from Tran et al. (2001)

IRASF00183-7111	0.327	12.77	45.1±0.6	2.4±1.2	44.9±0.6
IRAS00188-0856	0.129	12.31	11.8±0.3	7.3±0.5	11.1±0.7
IRAS00275-2859	0.279	12.46	35.8±0.1	3.8±0.2	35.4±0.3
IRAS00406-3127	0.342	12.64	11.6±0.3	1.2±0.6	11.5±0.3
IRAS02113-2937	0.194	12.29	1.7±0.1	8.1±0.2	<2.3

4.2 The AGN contribution in local ULIRGs and LIRGs

Table 4.1

Name	z	$\log(L_{\text{TIR}})$ L_{\odot}	$\tilde{f}_{6\text{AGN}}$ mJy	$\tilde{f}_{6.2\text{peakSB}}$ mJy	$f_{6\text{AGN}}$ mJy
IRASF02115+0226	0.400	12.48	1.2 ± 0.1	2.1 ± 0.1	1.0 ± 0.2
IRASF02455-2220	0.296	12.57	1.8 ± 0.1	2.5 ± 0.2	1.6 ± 0.2
IRAS03000-2719	0.221	12.41	2.7 ± 0.1	5.5 ± 0.2	2.2 ± 0.5
IRAS03538-6432	0.310	12.65	8.9 ± 0.2	4.9 ± 0.3	8.4 ± 0.5
IRAS03521+0028	0.152	12.46	2.1 ± 0.1	6.7 ± 0.2	1.5 ± 0.6
IRAS04384-4848	0.213	12.32	3.8 ± 0.3	5.1 ± 0.5	3.3 ± 0.5
IRAS17463+5806	0.309	12.48	2.2 ± 0.1	2.7 ± 0.1	1.9 ± 0.3
IRAS18030+0705	0.146	12.18	0.5 ± 0.1	15.8 ± 0.2	< 2.7
IRASF23529-2119	0.430	12.55	8.9 ± 0.1	1.1 ± 0.2	8.8 ± 0.1

4.2.2 Comparison to X-ray measurements

While we use the mid-IR continuum to quantify the AGN contribution, it is instructive to compare to X-ray data for part of our sample where such data are available. So far, the correlation between mid-IR continuum and X-ray emission was demonstrated only for Seyferts and QSOs (Lutz et al. 2004; Horst et al. 2008) rather than IR-selected galaxies. ULIRGs show often the simultaneous presence of active star formation and AGN. In principle, the contribution at mid-IR wavelengths that is due to the star formation should not influence the relation between the X-rays intrinsic emission and $f_{6\text{AGN}}$, since the $6.2\mu\text{m}$ PAH feature has been subtracted before measuring the latter. Anyway, before assuming that $f_{6\text{AGN}}$ is a good AGN quantifier, we test if the correlation between the AGN luminosity and the mid-IR continuum emission derived by Lutz et al. (2004) holds also for our sample.

We check the correlation for all the sources with X-ray data. Tab. 4.2 shows the results of our fit of the $6\mu\text{m}$ luminosity ($L_{6\text{AGN}}$) for the 28 galaxies for which X-ray observations are available in the literature. Fig. 4.3 compares mid-IR and X-ray luminosities: our measurements and limits for infrared galaxies are consistent with the mean ratio and dispersion found by Lutz et al. (2004) for Seyferts and QSOs, represented in the diagram by continuous and dotted lines. The only clear exception is the source IRASF15250+3608: it presents an absorbed mid-IR spectrum, likely indicating an obscured AGN, and different spectral decomposition methods, as shown both in Fig. 4.4 and in Nardini et al. (2008), agree that an AGN should give the main contribution to the mid-infrared emission. Nevertheless its weak X-ray emission is interpreted as due to starburst (Franceschini et al. 2003) with no evidence for absorption. Overall, these findings suggest that the X-ray emission of IRASF15250+3608 is dominated by host star formation while a strong AGN seen in the mid-IR is too obscured to even show tracers like reflected emission in the X-ray spectrum. The diagram does not show the 8 sources classified as Compton-thick from the X-ray spectrum (see Tab. 4.2) because of the impossibility to derive a reliable absorption corrected X-ray flux in such sources. Three

4 A backward evolution model for infrared surveys

Table 4.2. Galaxies with X-ray observations

Name	z	$\log(L_{\text{TIR}})$ L_{\odot}	$\log(\nu L_{6\text{AGN}})$ erg s^{-1}	$\log(L_{\text{HX}})^1$ erg s^{-1}	Notes ²
IRAS00188-0856	0.129	12.31	44.3	>41.9 ^a	SB/Compton-thick AGN
NGC1068	0.003	11.27	44.1	>40.9 ^b	Compton-thick AGN
NGC1275	0.018	11.20	43.6	43.8 ^b	AGN
NGC1365	0.005	11.00	42.8	41.6 ^b	AGN
IRAS03521+0028	0.152	12.46	>43.9	>41.3 ^a	SB/Compton-thick AGN
NGC1614	0.016	11.60	>43.3	>41.4 ^b	Compton-thick AGN
IRASF05189-2524	0.043	12.11	44.6	43.3 ^c	AGN
UGC05101	0.039	11.95	43.8	43.3 ^d	AGN
NGC3256	0.009	11.56	>43.1	41.4 ^b	SB
NGC3690/IC694	0.011	11.88	43.6	>41.5 ^e	Compton-thick AGN
IRASF12112+0305	0.073	12.28	>43.7	41.6 ^f	SB
UGC08058	0.042	12.51	45.1	44.0 ^g	AGN
MCG-03-34-064	0.017	11.24	43.8	42.4 ^b	AGN
NGC5135	0.014	11.17	>43.0	>40.9 ^b	Compton-thick AGN
NGC5256	0.028	11.49	>43.4	>41.9 ^b	Compton-thick AGN
UGC08696	0.038	12.14	43.8	42.4 ^h	AGN
IRASF14348-1447	0.082	12.30	>43.9	41.7 ^f	SB
IRASF15250+3608	0.055	12.02	44.0	41.5 ^f	SB
UGC09913	0.018	12.21	43.1	>41.0 ^h	Compton-thick AGN ⁱ
NGC6240	0.024	11.85	43.5	42.5 ^h	AGN
IRASF17207-0014	0.043	12.39	>43.8	41.6 ^f	SB
ESO286-IG019	0.043	12.00	43.9	42.9 ^f	AGN
NGC7130	0.016	11.35	42.8	>41.4 ^b	Compton-thick AGN
IRASF22491-1808	0.077	12.11	>43.6	41.2 ^f	SB
NGC7469	0.016	11.59	43.6	43.6 ^b	AGN
ESO148-IG002	0.045	12.00	43.6	42.3 ^f	SB/AGN
NGC7674	0.029	11.50	44.1	>41.9 ^b	Compton-thick AGN
IRASF23365+3604	0.064	12.13	>43.5	>41.5 ^a	SB/Compton-thick AGN

¹ Hard X-ray intrinsic luminosity (corrected for absorption) in the range 2.0 – 10.0 KeV.

² X-ray classification. If not indicated, the reference is the same as for the X-ray luminosity.

References. — (a) Teng et al. (2005) (b) Risaliti et al. (2000) (c) Severgnini et al. (2001) (d) Maiolino et al. (2003) (e) Della Ceca et al. (2002) (f) Franceschini et al. (2003) (g) Braito et al. (2004) (h) Ptak et al. (2003) (i) Iwasawa et al. (2005)

sources which may show in the X-rays either emission of a Compton-thick AGN or star formation signatures are shown with lower limits to the X-rays. They are all objects observed by Teng et al. (2005) and are too faint for conventional spectral fitting. Their hardness ratios (soft X-ray to far-IR flux ratios and hard X-ray to bolometric flux ratios) suggest that these galaxies are not energetically dominated by AGN, but the possibility that they host a Compton-thick AGN cannot be ruled out.

This first test is a further proof that $f_{6\text{AGN}}$ is a good proxy for nuclear activity for the

4.2 The AGN contribution in local ULIRGs and LIRGs

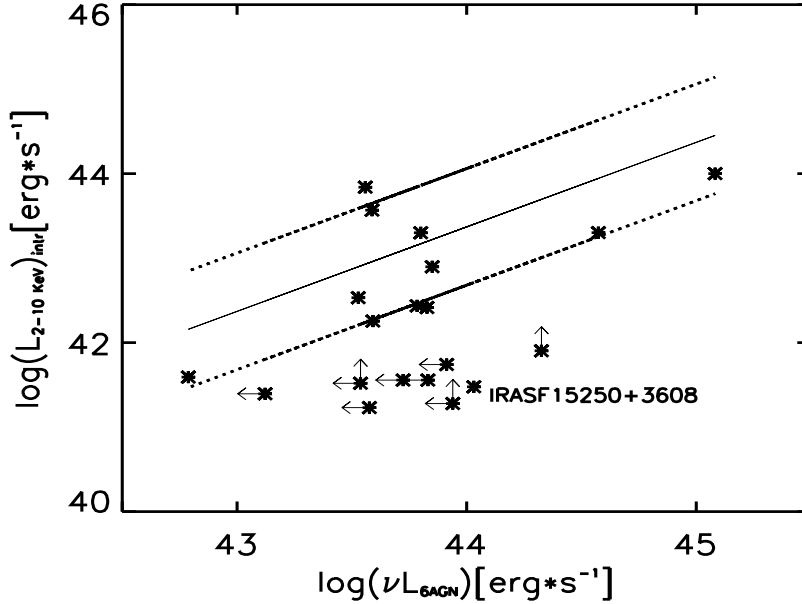


Figure 4.3: Hard X-ray luminosities (2 – 10 KeV) corrected for absorption vs. L_{6AGN} for those infrared galaxies where an absorption corrected X-ray flux was available. Continuum and dotted lines indicate the mean ratio and the dispersion found by Lutz et al. (2004) for Seyferts and QSOs.

objects in our sample. Furthermore, these data show that mid-IR emission is a powerful tool to quantify the AGN luminosity even for sources without X-ray detections, because of the high absorption due to the Compton-thick material surrounding the nucleus.

For the aims of this work, the use of mid-IR spectra, in particular of f_{6AGN} , is the best way to quantify the AGN fraction for several reasons: (1) in order to derive a local luminosity function, we need high statistics: the number of objects for which mid-IR spectra are available is much higher than the number of sources with X-ray data of sufficient quality; (2) we are interested in the contribution of AGN to the infrared emission: L_{6AGN} is much more correlated to the AGN's infrared emission than, for example, $L_{2-10KeV}$; (3) f_{6AGN} is sensible also to Compton-thick AGN, not detected in the X-rays: this kind of galaxies, already present in the local universe, becomes very important at high- z , as shown both in mid-IR (Daddi et al. 2007) and X-ray (Gilli et al. 2007) surveys.

4 A backward evolution model for infrared surveys

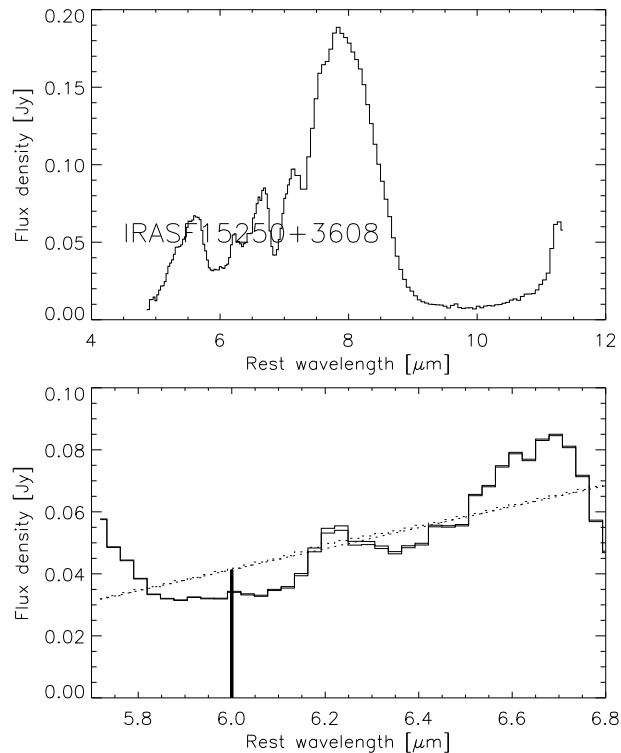


Figure 4.4: Decomposition of the mid-IR spectrum of IRAS F15250+3608. Symbols are like in Fig. 4.2. This source shows a mid-IR absorbed spectrum, indicating an obscured AGN, but the X-ray counterpart has no trace of nuclear activity (Franceschini et al. 2003).

4.2.3 Distribution of the AGN contribution

Next we want to study the AGN contribution to L_{TIR} of ULIRGs and LIRGs as a function of luminosity. Our results will be used in the modeling of § 4.3 to build composite SEDs taking into account the two main aspects (starbursts and AGN) of infrared galaxies.

Fig. 4.5 shows the distributions of the ratio between the $6\mu\text{m}$ AGN continuum luminosity and the total infrared luminosity ($vL_{6\text{AGN}}/L_{\text{TIR}}$) for five different luminosity bins, spanning a range from $10^{10.9}$ to $10^{12.8}L_{\odot}$. These distributions do not show the intrinsic AGN luminosity, but the fraction of the IR emission due to the contribution of an AGN, because of the normalization used.

As shown from the distributions of Fig. 4.5 (solid and cross-hatched histograms) and also in the diagram of Fig. 4.9 (open squares), there is not an evident trend with luminosity in the values of the means of the *detections*. In the bins at lower L_{TIR} there is good statistic, but the percentage of upper limits to $L_{6\text{AGN}}$ is rather high (upper limits are represented by cross-hatched histograms). In the bins at higher L_{TIR} , where the $f_{6\text{AGN}}$ detection rates increase in

4.2 The AGN contribution in local ULIRGs and LIRGs

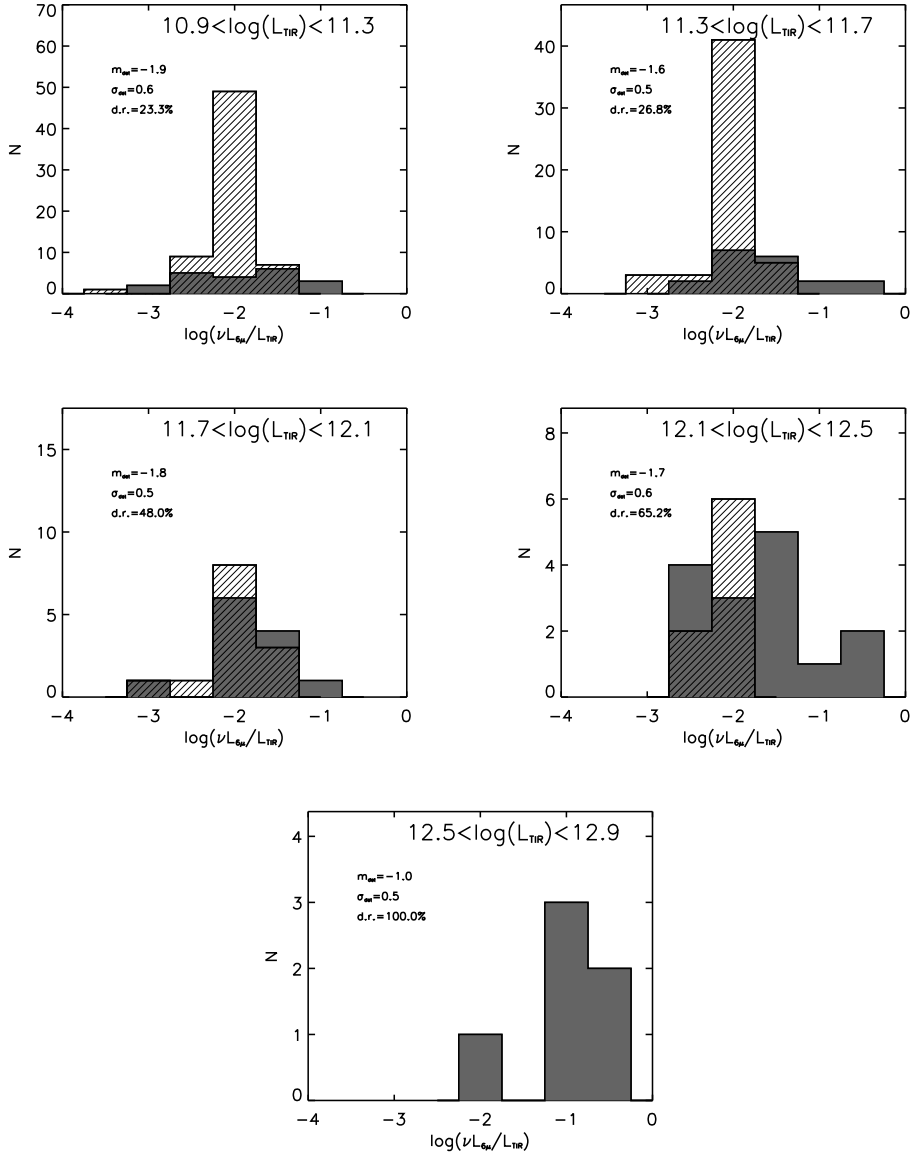


Figure 4.5: Distribution of $\nu L_{6\mu}/L_{TIR}$, for different luminosity bins. Solid histograms show the measurements, while the cross-hatched histograms indicate objects with upper limits. As indicated in each diagram, the mean values of the detections do not vary significantly between the different bins. What noticeably varies is the detection rate, spanning values from 23.3% to 100%.

4 A backward evolution model for infrared surveys

a significant way (solid histograms represent detections), the statistic becomes more modest. In both cases, the averages obtained from detections only (open squares in Fig. 4.9) have to be considered upper limits to the real mean values of the distributions of $\nu L_{6\text{AGN}}/L_{\text{TIR}}$.

The evident trend that our measurements show is in the detection rate as a function of L_{TIR} . The decreasing fraction of upper limits clearly means that the distribution is changing across the luminosity bins and that there must be a trend also in the intrinsic distribution of $\nu L_{6\text{AGN}}/L_{\text{TIR}}$. With some assumptions about the shape of the distribution, it is possible to obtain information about the main parameters (mean and standard deviation) of the intrinsic distribution of $\nu L_{6\text{AGN}}/L_{\text{TIR}}$ by Monte-Carlo simulations, taking into account the flux limit defining the RBGS sample as well as the *Spitzer*-IRS detection limit.

4.2.4 Simulating the distribution of the AGN contribution

In order to reproduce our measurements, in terms of detection rate, mean and standard deviation of the detections (hereafter d.r., m_{det} , σ_{det}), using Monte-Carlo simulations, we need to make assumptions about the intrinsic distribution of $\nu L_{6\text{AGN}}/L_{\text{TIR}}$ we are looking for and the quantities that affect our upper limits. $\nu L_{6\text{AGN}}/L_{\text{TIR}}$ is tightly correlated with two different quantities. $L_{6\text{AGN}}$ depends in a trivial way on $f_{6\text{AGN}}$, i.e. on the sensitivity of the instrument. L_{TIR} is related to the $60\mu\text{m}$ flux by relations well known and tested on IRAS data (Helou et al. 1985; Dale et al. 2001).

Our RBGS-based sample is selected at $60\mu\text{m}$. Therefore, the first step of the simulation consists in generating a population of sources having a $60\mu\text{m}$ flux density spanning a range from 5.24 to 200 Jy and a distribution $N(f_{\nu}) \propto f_{\nu}^{-1.5}$ (Sanders et al. 2003), expected for a complete sample of objects in a non-evolving Euclidean universe that is a reasonable approximation for the relatively small redshift range covered by our sample. We derive L_{TIR} for each source generated starting from its $60\mu\text{m}$ flux density, adopting $L_{\text{TIR}} \sim 2 \times \nu L_{60\mu\text{m}}$ as appropriate for our sample. Assuming that the distribution of $\nu L_{6\text{AGN}}/L_{\text{TIR}}$ is gaussian with a certain mean and standard deviation (m , σ), we calculate the expected value of $f_{6\text{AGN}}$. At this point we apply a detection limit to $f_{6\text{AGN}}$ and calculate d.r., m_{det} and σ_{det} . The values of m and σ that best reproduce the measured d.r., m_{det} and σ_{det} for each luminosity bin are assumed to be the parameters of the $\nu L_{6\text{AGN}}/L_{\text{TIR}}$ intrinsic distribution.

Our IRS data come from the public *Spitzer* archive, so from several observing campaigns with different goals. The depths of the observations are different for different objects. To assign a detection limit to $f_{6\text{AGN}}$, we consider the values of 3σ for the detections and the values of the upper limits for the non-detections in each luminosity bin. We assume the medians of the distributions of these values as the detection limits of our measurements. These values span from $\sim 18\text{ mJy}$ to $\sim 1\text{ mJy}$, depending on the luminosity bin (see Tab. 4.3).

Fig. 4.6 shows the results of the simulation for a population of 2×10^4 objects. This amount is necessary to make the results independent from the randomness of the generated values. Each diagram shows the best gaussians that, given the detection limit, reproduce the observed values of d.r., m_{det} and σ_{det} . A summary of the distribution parameters of

4.2 The AGN contribution in local ULIRGs and LIRGs

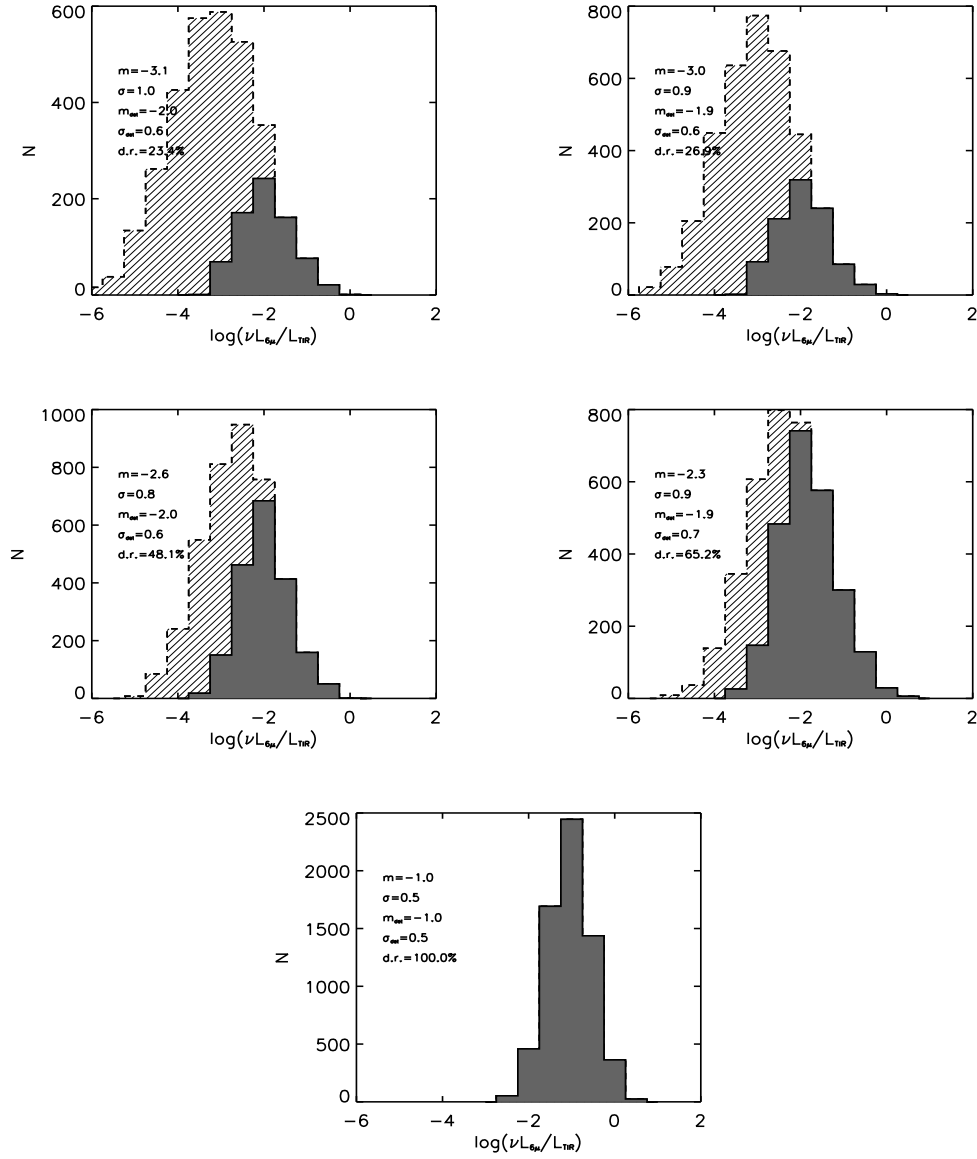


Figure 4.6: Simulations of $\nu L_{6\text{AGN}}/L_{\text{TIR}}$, assumed to be normal distributed, reproducing the same detection rates (d.r.), means (m_{det}) and sigma (σ_{det}) of the detections obtained from the data. The detection limit assumed for $f_{6\text{AGN}}$ is 20 mJy. Symbols are like in Fig. 4.5. Each simulation is made for a population of 2×10^4 objects. Each diagram reproduces the values observed in the corresponding panel of Fig. 4.5 and shows also mean (m) and sigma (σ) of the distribution adopted.

4 A backward evolution model for infrared surveys

Table 4.3. Distributions parameters of measurements and simulations

$\log(L_{\text{TIR}})$ L_{\odot}	Measurements			Detect.limit mJy	Simulations			m	σ
	m_{det}	σ_{det}	d.r.[%]		m_{det}	σ_{det}	d.r.[%]		
10.9÷11.3	-1.9	0.6	23.3	17.9	-2.0	0.6	23.4	-3.1	1.0
11.3÷11.7	-1.6	0.5	26.8	17.5	-1.9	0.6	26.9	-3.0	0.9
11.7÷12.1	-1.8	0.5	48.0	10.5	-2.0	0.6	48.2	-2.6	0.8
12.1÷12.5	-1.7	0.6	65.2	8.3	-1.9	0.7	65.2	-2.3	0.9
12.5÷12.9	-1.0	0.5	100.0	0.9	-1.0	0.5	100.0	-1.0	0.5

measurements and simulations is presented in Tab. 4.3. The values found for m and σ are also plotted in Fig. 4.9 (green stars). Here, a correlation between the contribution to the infrared luminosity due to the AGN and the total infrared luminosity is clearly visible, with a dispersion decreasing with the luminosity. The best fit, $\nu L_{6\text{AGN}}/L_{\text{TIR}} \propto L_{\text{TIR}}^{\alpha}$, gives $\alpha = 1.4 \pm 0.6$.

The achieved results assume the $\nu L_{6\text{AGN}}/L_{\text{TIR}}$ distribution to be gaussian for each luminosity bin. This is a reasonable first hypothesis, because it is simple with a small number of parameters and reproduces the observations in terms of detection rate, mean and dispersion of the detections. More attention is needed when applying it to our Monte Carlo simulations of the infrared sky. The low AGN activity end of the distribution, corresponding mostly to IRS non-detections, is certainly poorly constrained, but such differences between already weak and totally insignificant AGN will not have a major effect on the predictions. Differences at the high AGN activity end can be more important by introducing or missing very luminous mid-IR sources dominated by AGN. Comparing for example the $\log(\nu L_{6\text{AGN}}/L_{\text{TIR}})$ distribution for the third luminosity bin in Fig. 4.5 and Fig. 4.6 ($11.7 < \log(L_{\text{TIR}}) < 12.1$), we find the modelled distribution extending up to $\log(\nu L_{6\text{AGN}}/L_{\text{TIR}}) \sim 0$ which is not reached by the observations. This could reflect limits in the statistics of our IRS sample as well as a true overprediction of our simple gaussian hypothesis at the high $\log(\nu L_{6\text{AGN}}/L_{\text{TIR}})$ end. We will return to this issue in § 4.4.2 in the context of our backward evolution model. In the following we assume that the increase of the fraction of AGN occurs only up to the last luminosity bin measured ($L_{\text{TIR}} \sim 10^{12.7} L_{\odot}$) and then the relation between $\nu L_{6\text{AGN}}/L_{\text{TIR}}$ and L_{TIR} becomes flat (see Fig. 4.9, green dotted line).

4.2.5 Evolution with redshift

It is interesting to check if and how the relation just found between $\nu L_{6\text{AGN}}/L_{\text{TIR}}$ and L_{TIR} evolves with redshift. Previous studies already showed that, even if in the local universe ULIRGs tend to be AGN-dominated at $L_{\text{TIR}} > 10^{12.5} L_{\odot}$ (Lutz et al. 1998; Veilleux et al. 1999; Tran et al. 2001), this trend is not followed any more at high redshifts. For example,

4.2 The AGN contribution in local ULIRGs and LIRGs

submillimeter galaxies that, with their typical infrared luminosity of $\sim 10^{13} L_{\odot}$, are among the most luminous objects known, are mainly starburst dominated. Mid-IR spectroscopy in fact showed that the contribution to the total luminosity due to AGN continuum is small in most of the sources observed with *Spitzer* IRS at high redshifts (Lutz et al. 2005a or Chapter 2, Menéndez-Delmestre et al. 2007, Valiante et al. 2007 or Chapter 3, Pope et al. 2008). These results are consistent with X-ray observations of the same population (Alexander et al. 2005a).

A systematic study at high redshifts is difficult with current data. The high-redshift sources with mid-IR spectroscopy were often selected for their high luminosity. So, we can check our relation only for the most luminous part of the range in L_{TIR} spanned in the local Universe. More important, in order to have an unbiased sample of objects, we have to exclude sources selected by methods that prefer AGN or starbursts as power source of the infrared emission. For this reason, we do not include in our comparison, for example, optically obscured sources selected at $24\mu\text{m}$ (Yan et al. 2004, 2007), most of them presenting warm dust, typical of AGN-powered sources, in the comparison of mid-IR and millimeter observations (Lutz et al. 2005b).

Ideally, to be consistent with the locally derived IRAS luminosity function, a high- z sample should be selected at $60 \times (1+z)\mu\text{m}$, at the peak of the dust emission, but this cannot be done with our pre-*Herschel* observations.

Our high redshift sample includes all the sources observed by Menéndez-Delmestre et al. (2007), Valiante et al. (2007), Pope et al. (2008) and Brand et al. (2008) for which the observations cover the range from $5.5\mu\text{m}$ to $6.85\mu\text{m}$ rest wavelength (see Tab. 4.4). Objects from the first three works are submillimeter galaxies, some of them radio pre-selected. These selections do not prefer AGN or starburst as main power source, even if SMGs later showed to be mainly starburst powered. Sources from Brand et al. (2008) are optically faint objects selected at $70\mu\text{m}$: their mid-IR spectra show that they can be either PAH or absorption dominated. All the IRS data have been retrieved from the *Spitzer* archive and reduced using the same techniques described in § 4.2.1, in order to derive $L_{6\text{AGN}}$ in a consistent way for all the objects. The results of the fit process are listed in Tab. 4.4. The values of L_{TIR} have been taken from the works cited above.

The sources of the high redshift sample have very large infrared luminosities ($L_{\text{TIR}} \sim 10^{13} L_{\odot}$), so we can compare their $\nu L_{6\text{AGN}}/L_{\text{TIR}}$ with the local values only in the overlap of the luminosity ranges. We can check if the trend found in the IRAS sample still holds in distant galaxies. We consider three luminosity bins, each spanning a range that is twice the bins previously considered. Fig. 4.7 shows the distributions of the $\nu L_{6\text{AGN}}/L_{\text{TIR}}$. Unfortunately, the statistic is rather modest for the bins at lowest and highest luminosities.

The redshift range spanned by this sample is very broad ($0.37 < z < 3.35$). In particular, the bin at lowest luminosity is mainly populated by objects lying at $z \lesssim 1$, while the most luminous bins include the most distant sources. We treat the whole sample as a unique population, because the inclusion of the $z \lesssim 1$ objects does not significantly change the $\nu L_{6\text{AGN}}/L_{\text{TIR}}$ distribution in any of the luminosity bins.

4 A backward evolution model for infrared surveys

Table 4.4. High redshift sample of infrared galaxies: results of the fit and corrected $f_{6\text{AGN}}$ fluxes

Name	z	$\log(L_{\text{TIR}})$ L_{\odot}	$\tilde{f}_{6\text{AGN}}$ mJy	$\tilde{f}_{6.2\text{peakSB}}$ mJy	$f_{6\text{AGN}}$ mJy
Sources from Brand et al. (2008)					
70Bootes1	0.50	12.15	0.21±0.04	0.30±0.08	0.18±0.05
70Bootes2	0.37	11.79	0.12±0.04	0.50±0.07	<0.12
70Bootes3	0.99	13.05	0.15±0.04	1.10±0.08	<0.25
70Bootes4	0.98	12.95	0.14±0.04	1.15±0.07	<0.14
70Bootes5	1.21	13.24	1.98±0.08	0.28±0.14	1.96±0.08
70Bootes6	0.94	13.01	1.81±0.07	0.25±0.12	1.79±0.07
70Bootes7	0.66	12.61	0.32±0.04	1.30±0.07	<0.43
70Bootes8	0.81	12.88	0.74±0.06	0.30±0.10	0.71±0.06
70Bootes9	0.67	12.81	0.23±0.05	2.38±0.09	<0.42
70Bootes10	0.51	12.41	0.72±0.06	0.29±0.10	0.69±0.07
70Bootes11	0.48	12.49	2.01±0.07	0.31±0.13	1.98±0.08
Sources from Pope et al. (2008)					
C3	1.88	12.78	0.15±0.03	0.10±0.05	0.14±0.03
GN39	1.98	12.70	0.08±0.04	0.54±0.07	<0.08
GN07	1.99	12.84	0.09±0.03	0.30±0.06	<0.09
GN06	2.00	12.81	0.06±0.03	0.51±0.05	<0.06
C1	2.01	12.98	0.48±0.07	0.30±0.12	0.45±0.07
GN26	1.23	12.56	0.05±0.02	0.81±0.03	<0.14
GN17	1.73	12.30	0.17±0.03	0.39±0.06	0.13±0.05
GN19	2.48	13.08	0.13±0.04	0.26±0.06	<0.13
GN04	2.55	12.82	0.24±0.04	0.15±0.08	0.23±0.05
Sources from Menéndez-Delmestre et al. (2007)					
SMMJ030228+000654	1.41	13.44	0.07±0.03	0.27±0.05	<0.12
SMMJ163639+405636	1.50	12.81	0.09±0.02	0.17±0.04	0.07±0.03
SMMJ163650+405735	2.38	13.52	0.41±0.05	0.33±0.07	0.38±0.06
Sources from Valiante et al. (2007) or Chapter 3					
SMMJ00266+1708	2.73	12.70	0.15±0.05	0.30±0.09	<0.15
SMMJ02399-0136	2.81	13.40	0.42±0.04	0.21±0.07	0.40±0.04
SMMJ09429+4659	2.38	13.80	0.08±0.04	0.43±0.07	<0.08
SMMJ09431+4700	3.36	12.95	0.58±0.04	0.29±0.07	0.55±0.04
SMMJ10519+5723	2.67	13.07	0.11±0.03	0.14±0.05	0.10±0.03
SMMJ10521+5719	2.69	13.25	0.13±0.03	0.13±0.05	0.11±0.03
MMJ154127+6616	2.79	12.95	0.14±0.01	0.19±0.02	0.12±0.02
SMMJ16369+4057	1.21	12.23	0.15±0.02	0.23±0.03	0.12±0.03
SMMJ16371+4053	2.38	13.04	0.14±0.03	0.18±0.05	0.12±0.03

4.2 The AGN contribution in local ULIRGs and LIRGs

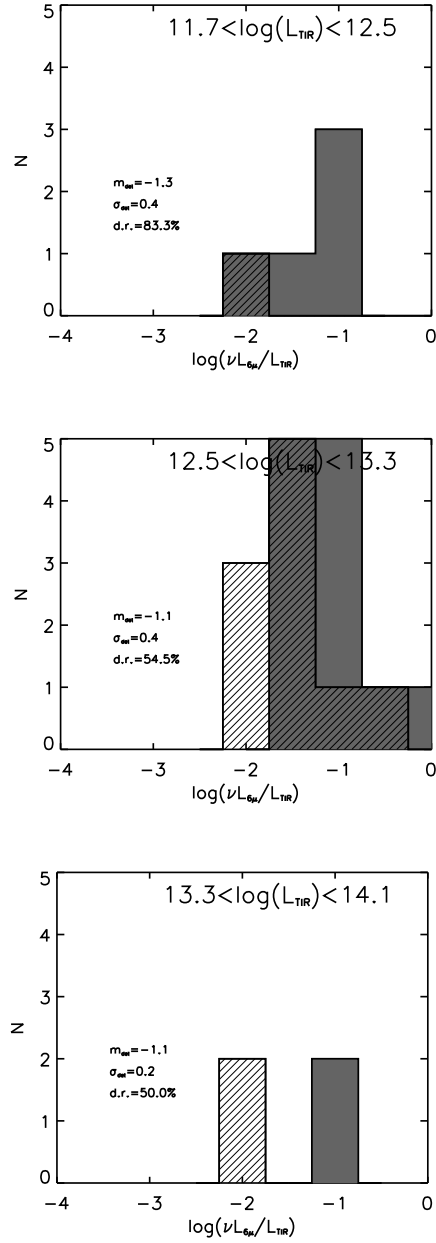


Figure 4.7: Distribution of $\nu L_{6\mu}/L_{\text{TIR}}$ for different luminosity bins. The sample lies at redshift $0.37 < z < 3.35$. Symbols are like in Fig. 4.5. Each diagram shows also the mean, the dispersion and the detection rate of the distribution.

4 A backward evolution model for infrared surveys

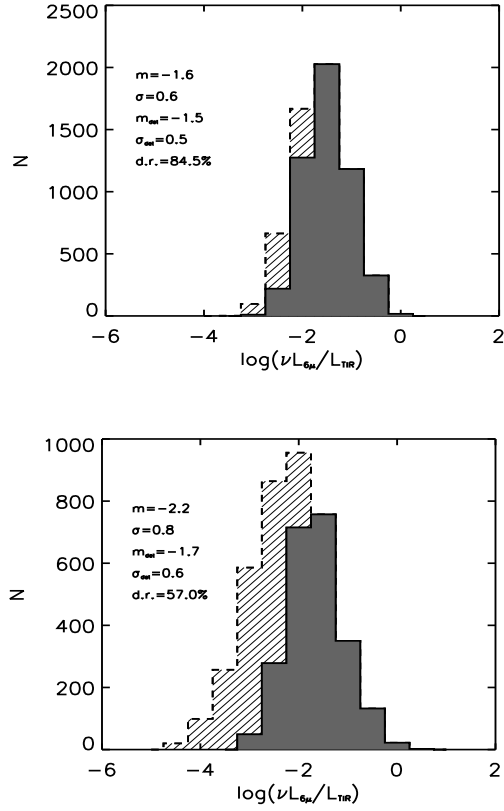


Figure 4.8: Simulations of $\nu L_{6AGN}/L_{TIR}$ normal distributions reproducing the same detection rates (d.r.), means (m_{det}) and sigma (σ_{det}) of the detections obtained from the data of the high redshift sample, assuming a detection limit of 0.13 mJy. Each diagram reproduces the values observed in the corresponding panel of Fig. 4.7, while the last luminosity bin has been not simulated because the statistics it too low to have the fit converging. Symbols are like in Fig. 4.5. Each diagram shows also mean (m) and sigma (σ) of the distribution adopted.

In order to characterize the intrinsic distribution of $\nu L_{6AGN}/L_{TIR}$, we run Monte-Carlo simulations with the same techniques used for the local galaxies explained in § 4.2.4. We generate a population of sources having $60\mu\text{m}$ flux spanning a range from 40 to 1100 mJy. We calculate the expected value of the $60\mu\text{m}$ rest-frame flux from the $850\mu\text{m}$ and $70\mu\text{m}$, respectively for the submillimeter and the $70\mu\text{m}$ selected sources, assuming a grey-body spectrum with emissivity index $\beta = 1.5$ and $T_d = 32\text{K}$. The values obtained give us the range of the $60\mu\text{m}$ population to simulate. Because of the low statistic in the bin at highest luminosity, we are able to reproduce only the distributions of the first two bins, shown in

4.2 The AGN contribution in local ULIRGs and LIRGs

Fig. 4.8.

At high redshift, AGN contributions to the total infrared luminosity are different from the local ones at same luminosity, at least for certain luminosity ranges as can be seen also in Fig. 4.9. For $L_{\text{TIR}} \sim 10^{12}L_{\odot}$, the AGN contribution is still consistent with the local universe distribution given the small number statistics. For the better populated $12.5 < \log(L_{\text{TIR}}) < 13.3$ bin, which contains most of the SMGs, the AGN contribution typically is clearly lower than for the few local objects reaching similar luminosity. All this evidence is tentative given the small number statistics, the possible biases invoked by the selection and identification of the populations used and the broad redshift range considered. It is hence too early to conclude on a specific functional form of the change in the $\nu L_{6\text{AGN}}/L_{\text{TIR}}$ relation. For our further applications in the simulation, we simply assume that the relation is the same as derived locally, with a change in the behaviour of the flat part: while in the local universe the increase of the AGN contribution stops at $L_{\text{TIR}} \sim 10^{12.7}L_{\odot}$, for distant galaxies it occurs at lower luminosities ($L_{\text{TIR}} \sim 10^{12}L_{\odot}$).

4.2.6 Discussion and conclusions

The different role of AGN at low and high redshift for objects in the same L_{TIR} class should not be a surprise. Fig. 4.9 can be read in two (equivalent) ways: (1) the contribution of AGN to L_{TIR} is lower at high- z respect to the local universe for sources with $L_{\text{TIR}} \sim 10^{13}L_{\odot}$, or (2) the AGN content of high- z sources with $L_{\text{TIR}} \sim 10^{13}L_{\odot}$ is similar to that of local galaxies with $L_{\text{TIR}} \sim 10^{12}L_{\odot}$. This latter conclusion points out an analogy in the properties of SMGs and local ULIRGs.

Such an analogy has been already discussed by Tacconi et al. (2006): from CO observations of a sample of 14 SMGs, they conclude that the density of the molecular gas, the luminosity surface density and the temperature of the dust are the same in the two populations and SMGs are similar to local ULIRGs mergers, suitably scaled for their larger masses, luminosities and star formation rates, as well as their greater gas fractions. In spatially resolved observations, SMGs and ULIRGs show considerable likenesses also respect to their kinematic (Tacconi et al. 2008): the SMGs presenting multiple components are interacting systems and are similar to local double-nucleus ULIRGs, while SMGs showing characteristics of a rotational star-forming gas disk present the same surface and volume densities, for example, of the extremely compact ULIRG Arp220. All SMGs studied with sub-arcsecond millimeter interferometer so far, appear to be major mergers in different stages, similar to local ULIRGs.

Our analysis, nevertheless, is modeling-oriented: its purpose is not to find a theoretical explanation for the different populations observed, but just to develop an evolutionary model based on observations being able to reproduce available data and to drive forthcoming surveys with new instruments.

In summary, we have used spectral decomposition to a large sample of *Spitzer* IRS spectra of ULIRGs and LIRGs with $L_{\text{TIR}} > 10^{11}L_{\odot}$ to isolate the AGN $6\mu\text{m}$ continua. We compared

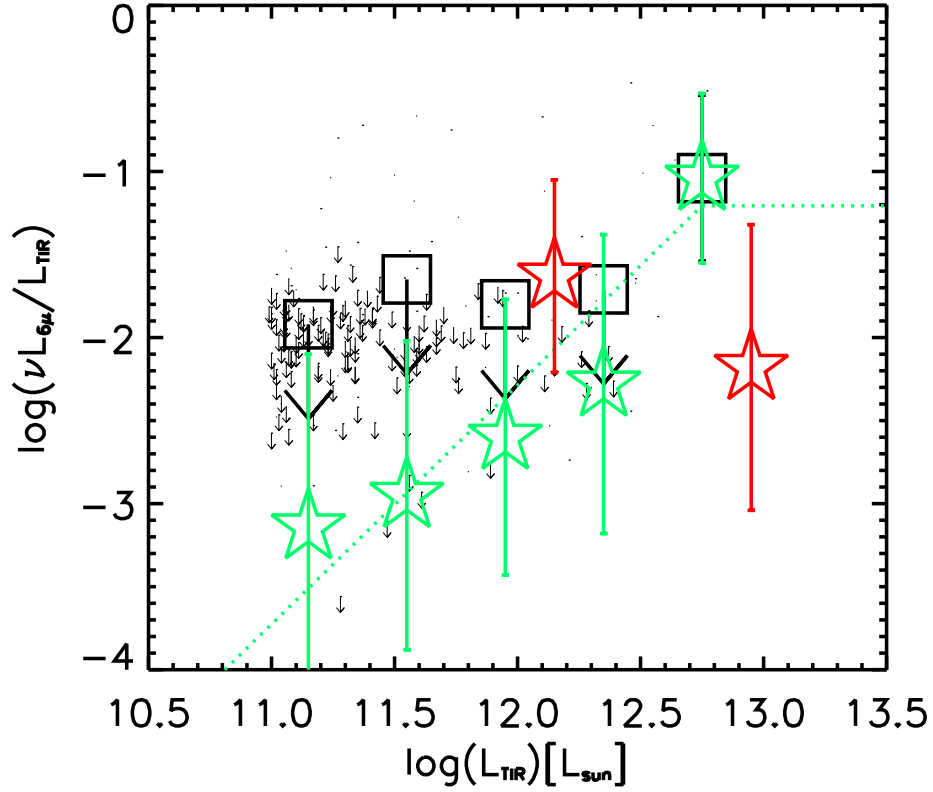


Figure 4.9: $\nu L_{6\mu}/L_{\text{TIR}}$, vs. L_{TIR} . Dots and small arrows represent respectively measurements and upper limits of all the galaxies of our local sample. The large open squares are the means of the detections (m_{det}) in the measurements (see Tab. 4.3 and Fig.4.5). Because of the large amount of non-detections, they represent only an upper-limit of the true $\log \nu L_{6\mu}/L_{\text{TIR}}$ for almost all the bins. The green stars and their errorbars show means (m) and sigma (σ) of the gaussian distributions adopted in the simulations in order to reproduce detection rates (d.t.), means (m_{det}) and sigma (σ_{det}) of the detections from the measurements (see Tab. 4.3 and Fig.4.6). The best fit, $\nu L_{6\mu}/L_{\text{TIR}} \propto L_{\text{TIR}}^{\alpha}$, gives $\alpha = 1.4 \pm 0.6$ and is shown as a dotted green line: the relation is assumed to be flat at high L_{TIR} . The red stars and their errorbars show means and sigma of the gaussian distributions adopted to reproduce measurements of the high redshifts sample (see Fig. 4.7 and Fig. 4.8). The relation found for the local galaxies does not hold any more.

4.3 The model: number counts and redshift distributions of infrared sources

$L_{6\text{AGN}}$ with the intrinsic X-ray luminosity, where available in the literature. The correlation found in previous studies still holds also for our sample. The distribution of $\nu L_{6\text{AGN}}/L_{\text{TIR}}$ depends on L_{TIR} . Even if the mean value of the detections does not vary significantly, the number of the detections increases with increasing luminosity, indicating a change in the intrinsic distribution. Monte-Carlo simulations, making the assumption of an intrinsically gaussian distribution, quantify this increase with luminosity of the AGN contribution to the infrared luminosity. The best fit, $\nu L_{6\mu\text{m}}/L_{\text{TIR}} \propto L_{\text{TIR}}^\alpha$, gives $\alpha = 1.4 \pm 0.6$. The relation does not hold any more at high redshifts. The most luminous high redshift infrared galaxies, $L_{\text{TIR}} \sim 10^{13} L_\odot$, show a small contribution from AGN, being mainly starburst powered. However, the number of distant objects with mid-IR observations is still small.

4.3 The model: number counts and redshift distributions of infrared sources

4.3.1 The strong evolution of infrared galaxies: observational evidence

There has been, in the past years, strong observational evidence indicating extremely high rates of evolution for infrared galaxies.

First, galaxy evolution can be observed through its imprint on the far-IR extragalactic background. Weakly constrained even as recently as the end of the 90s, various observations now measure or give upper/lower limits on the background from the ultraviolet (UV) to the millimeter waveband (e.g. Hauser & Dwek 2001). Data show the existence of a minimum between 3 and $10\mu\text{m}$ separating direct stellar radiation from the infrared part due to radiation re-emitted by dust. This re-emitted dust radiation contains a comparable integrated power as the optical/near-IR: this amount is much larger than what is measured locally (~ 30 per cent). The CIB is thus likely to be dominated by a population of strongly evolving redshifted infrared galaxies. Since the long-wavelength spectrum of the background is significantly flatter than the spectrum of local star-forming galaxies, it strongly constrains the far-IR radiation production rate history (Gispert et al. 2000). The energy density must increase by a factor larger than 10 between the present time and redshift $z \sim 1 - 2$ and then stay rather constant at higher redshift (till $z \sim 3$).

Secondly, several deep cosmological surveys at 15, 24, 70, 90, 170, 850 and $1300\mu\text{m}$ have resolved a fraction of the CIB into discrete sources. For all surveys, number counts indicate a very strong cosmological evolution of infrared galaxies, not only in the total power radiated but also in the shape of the LF. This is particularly obvious at submillimeter wavelengths, where the background is dominated by high-luminosity galaxies (SCUBA and MAMBO sources). The high rates of evolution exceed those measures in other wavelength domains as well as those observed for quasars and active galactic nuclei (AGN).

Finally, high rates of evolution are suggested by the detection of Poissonian fluctuations of the CIB at a high level at 60 and $100\mu\text{m}$ with IRAS (Miville-Deschênes et al. 2002), and

4 A backward evolution model for infrared surveys

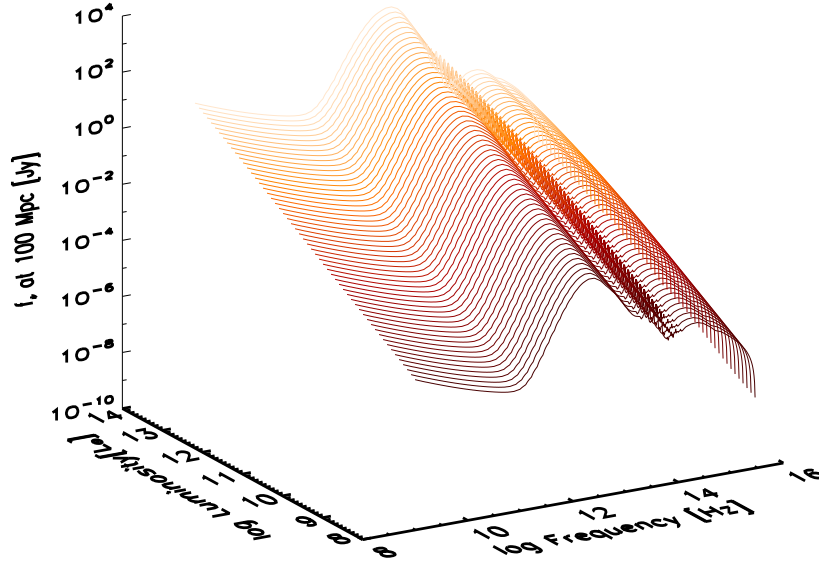


Figure 4.10: The family of SEDs used to derive the adopted SEDs for $\log(L) = 8 - 13.5L_{\odot}$ (Dale et al. 2001; Dale & Helou 2002). The flux density is expressed in Jansky and is scaled for a distance of 100 Mpc. Color intensity is related with the temperature: it spans the range 23 – 45 K.

170 μm with ISOPHOT (Lagache et al. 2000; Matsuhara et al. 2000). For example, the constraints given by Matsuhara et al. (2000) on the galaxy number counts indicate the existence of a strong evolution in the counts.

4.3.2 SEDs

Most of the backward evolution models (§ 4.1) separate the infrared sources into different populations. For example, Franceschini et al. (1988) consider three different populations: (1) normal late-type galaxies, (2) interacting/starburst galaxies and (3) galaxies with AGN. IRAS studies showed that galaxies of different nature in the local Universe have different spectral energy distributions (SEDs), e.g. different values of the f_{60}/f_{25} ratio, so usually each population is associated with a particular SED family. The different populations of the model can evolve as a single population (Xu et al. 1998; Xu 2000) or at different rates, assuming a local LF for each component (Xu et al. 2001). Nevertheless, it is known that infrared galaxies, in particular ULIRGs, can host both starburst activity and an AGN (Genzel et al. 1998; Lutz et al. 1998) and that galaxies classified as Seyfert show starburst tracers at infrared

4.3 The model: number counts and redshift distributions of infrared sources

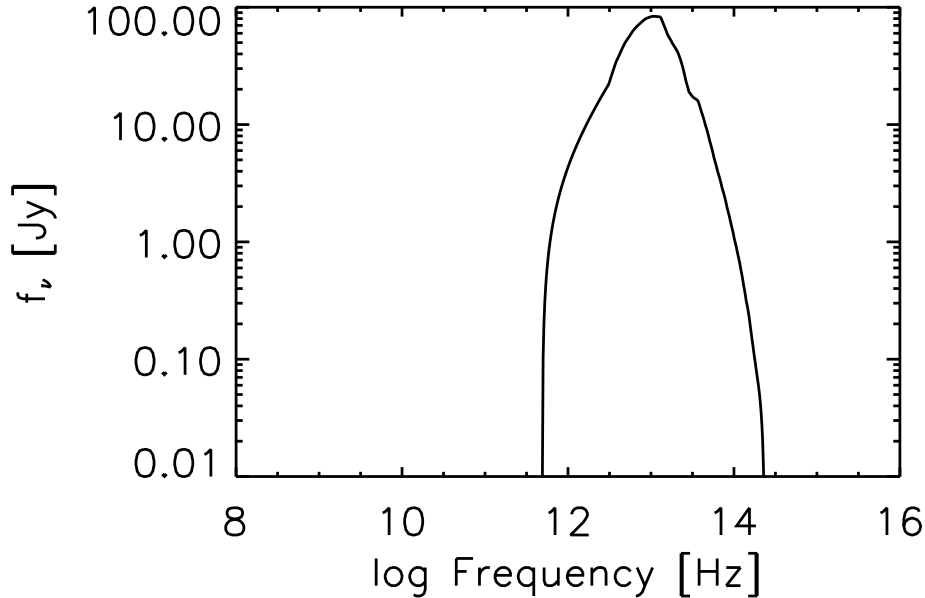


Figure 4.11: AGN template used in the model. It is the nuclear infrared continuum spectrum of the Seyfert galaxy NGC1068 calculated by Efstathiou et al. (1995).

wavelengths (Lutz et al. 2004), while most of the far-IR emission in local QSOs is powered by starbursts (Schweitzer et al. 2006).

The SEDs can either be constructed empirically, considering the individual components responsible for the overall emission from the galaxies (e.g. Rowan-Robinson 1992), or using radiative transfer models (e.g. Efstathiou et al. 2000). While a complicated array of dust properties contributes to the SED of each galaxy, studies of IRAS galaxies have typically reduced the description to a best-fit single dust temperature, T_d , with a one-to-one mapping to the f_{60}/f_{100} flux ratio (hereafter referred to as $R(60, 100)$). It has been demonstrated, as well, that local IRAS galaxies exhibit correlations of $R(60, 100)$ with luminosity (e.g. Dale et al. 2001) and that $R(60, 100)$ changes systematically over a large range of luminosities. A statistical relation exists between $R(60, 100)$ and infrared luminosity, even if the distribution is broad. Up to date, only preliminary analyses of the distribution spread in temperature for each luminosity bin and of its evolution exist (Chapman et al. 2003b). Difficulties of models with simple SED families and evolution functions became obvious with *Spitzer* data (e.g. Lagache et al. 2004). There is already evidence for a change in SED properties with redshift, with the intrinsic SED shapes of high z SMGs resembling lower luminosity local objects rather than similarly luminous local HYLIRGs, but a deep study of SEDs and tem-

4 A backward evolution model for infrared surveys

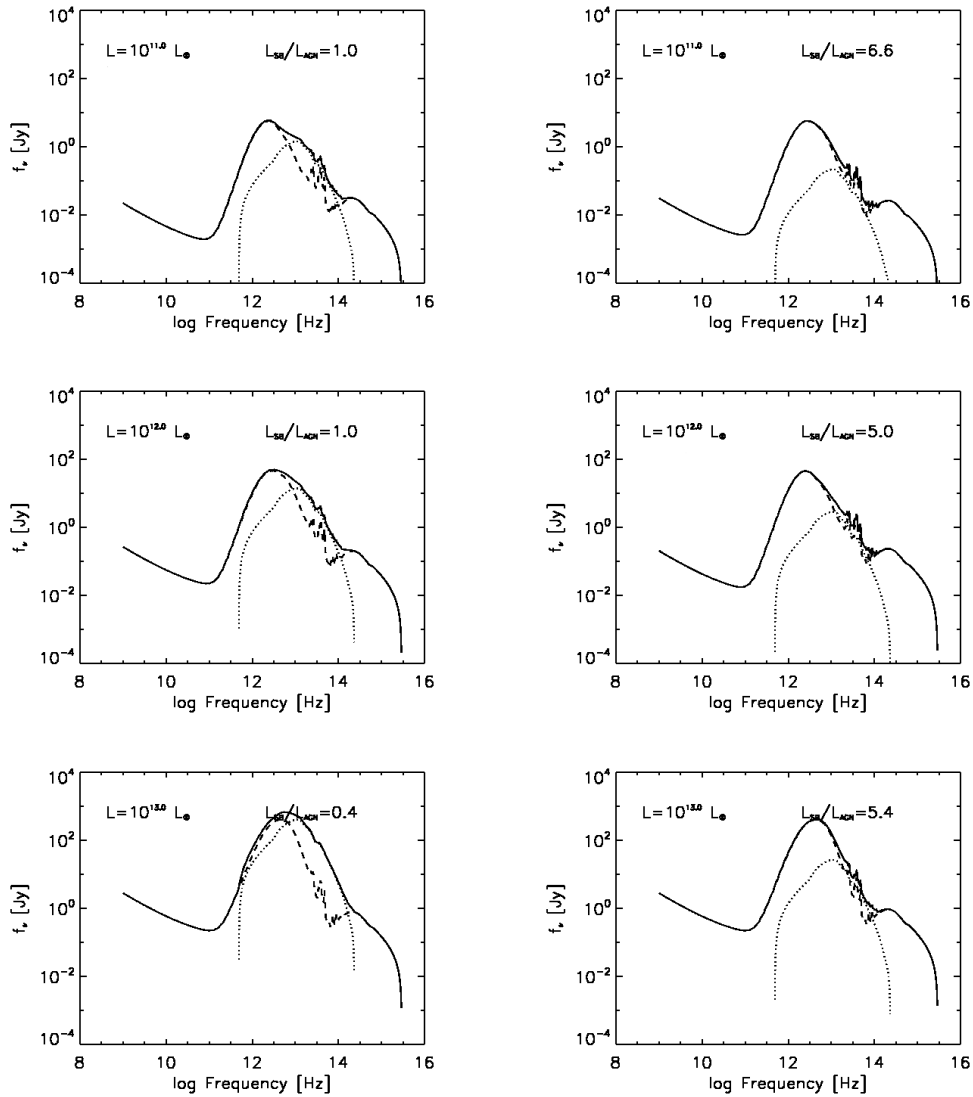


Figure 4.12: Some examples of adopted SEDs (solid lines) obtained adding a star-forming galaxy spectrum (dashed lines) (Dale et al. 2001; Dale & Helou 2002) and an AGN template (dotted lines) (Efstathiou et al. 1995). The flux density is expressed in Jansky and is scaled for a distance of 100 Mpc. In each diagram is indicated L_{TIR} and the ratio between the luminosity of the starburst spectrum and the luminosity of the AGN. For each luminosity class, two examples are shown: an AGN-dominated SED ($L_{SB}/L_{AGN} \leq 1$, left column) and a starburst-dominated SED ($L_{SB}/L_{AGN} > 1$, right column).

4.3 The model: number counts and redshift distributions of infrared sources

peratures of high-redshift galaxies is still missing. The main problems are the degeneracy of dust temperature with redshift (Blain et al. 2002), the limited sample of sub-millimeter galaxies with measurements of spectroscopic redshifts (Chapman et al. 2005; Valiante et al. 2007; Pope et al. 2008), and the selection effects on dust temperature induced by current methods to select high redshift infrared galaxies.

In building the SEDs for our model, we will take into account the coexistence of starburst and AGN in the same galaxies, their varying contribution with L_{TIR} , and the spread in the luminosity-temperature ($L - T$) relation. AGN are hosted in infrared galaxies of different luminosities and their contribution to the total infrared emission can be either negligible or predominant. We studied and discussed the problem of the AGN contribution in § 4.2. We found that, on average, the contribution to the L_{TIR} due to an AGN in IRAS galaxies is proportional to $L_{\text{TIR}}^{1.4}$ of the host. Even if the dispersion in the relation allows the presence of low luminosity AGN-dominated objects (e.g. NGC1068, $\log(L/L_{\odot}) = 11.3$), as well as ULIRGs powered by pure starbursts (e.g. IRASF19297-0406, $\log(L) = 12.4 L_{\odot}$), this correlation holds over a two order of magnitude range, $\log(L) \sim 11 - 13 L_{\odot}$. In § 4.2, we estimated the AGN contribution measuring the emission at $6\mu\text{m}$, after the subtraction of a starburst-like spectrum; this method does not require to spatially resolve the AGN from the host.

In the simulation, we follow the opposite direction. Each source is generated on the base of its \tilde{L}_{TIR} , comprehensive of both the starbursts (\tilde{L}_{SB}) and AGN (\tilde{L}_{AGN}) contributions. Starting from \tilde{L}_{TIR} , we calculate the expected value $\langle vL_{6\mu\text{m}}/L_{\text{TIR}} \rangle$ for that luminosity, using the relation found in § 4.2:

$$vL_{6\mu\text{m}}/L_{\text{TIR}} \propto L_{\text{TIR}}^{1.4}. \quad (4.1)$$

and assuming that it holds up to $L_{\text{TIR}} = L_*$, and then becomes flat (see Fig. 4.9). The value of L_* depends on the redshift.

Then, we generate a random value of $vL_{6\mu\text{m}}/L_{\text{TIR}}$ assuming its distribution is a gaussian with mean $\langle vL_{6\mu\text{m}}/L_{\text{TIR}} \rangle$ and sigma corresponding to the luminosity bin where \tilde{L}_{TIR} lies (see Tab. 4.3). From this random value we derive $\tilde{f}_{6\text{AGN}}$. Last, we scale an AGN template (see Fig. 4.11) in order to have the right flux density $\tilde{f}_{6\text{AGN}}$ at $6\mu\text{m}$. The AGN template used is the model calculated by Efstathiou et al. (1995) for the nuclear infrared continuum spectrum of the Seyfert galaxy NGC1068. The luminosity of the scaled template, \tilde{L}_{AGN} , is the contribution of the AGN to \tilde{L}_{TIR} .

Spectral templates for starbursts are taken from the Dale et al. (2001) (see also Dale & Helou 2002) catalog, divided into 64 classes from $R(60, 100) = 0.29$ to 1.64, corresponding roughly to single-component dust-temperature models of 23 – 45 K. SEDs are normalized integrating each spectrum over the 8 – 1000 μm range and scaling to the expected value of L_{TIR} for its $R(60, 100)$, calculated from the relation found by Chapman et al. (2003b)

$$R(60, 100) = C_* \times \left(1 + \frac{L_*}{L_{\text{TIR}}}\right)^{-\delta} \times \left(1 + \frac{L_{\text{TIR}}}{L_*}\right)^{\gamma} \quad (4.2)$$

with $\gamma = 0.16$, $\delta = 0.02$, $C_* = 0.45$ and $L_* = 5.0 \times 10^{10} L_{\odot}$. In this way we obtain an

4 A backward evolution model for infrared surveys

SED family in the range $10^9 - 10^{15.7}$ Hz spanning luminosities $\log(L) = 8 - 13.5 L_\odot$ (see Fig. 4.10). In the simulation, we use the relation of Chapman et al. (2003b) for the starburst contribution \tilde{L}_{SB} to the total infrared luminosity only, which we obtain by subtraction \tilde{L}_{AGN} from \tilde{L}_{TIR} . From Eq. 4.2 we obtain the corresponding mean $\langle R(60, 100) \rangle$ for the \tilde{L}_{SB} of the generated source. Then, we calculate the spread in the $L - T$ relation and generate a random value of $R(60, 100)$, following the gaussian distribution calculated by Chapman et al. (2003b) (see their Eq. 6) and centered on $\langle R(60, 100) \rangle$. Finally, we rescale to the correct \tilde{L}_{SB} the Dale & Helou (2002) library SED for the $R(60, 100)$, which was obtained from the gaussian distribution implementing the spread in the $L - T$ relation.

To obtain the final SED, we add the two spectra derived for the AGN and starbursts parts. Fig. 4.12 shows examples of SEDs with different L_{TIR} and different AGN contributions. Because the model takes into account both the average relation and its dispersion, it permits a wide range of combinations of values for L_{TIR} and AGN fraction.

4.3.3 Model parameters

In this section we describe the algorithm to model coherently the number counts in different bands. An evolutionary model needs some basic “ingredients”:

- the spectral energy distributions, already described in §4.3.2, depending on L_{TIR} , $R(60, 100)$ and AGN content
- a cosmological model describing the accessible volume in a survey solid angle as a function of redshift. This is now well constrained from WMAP results (Spergel et al. 2007)
- a luminosity function at $z = 0$, e.g. the IRAS luminosity function (Sanders et al. 2003)
- the evolution functions for density and luminosity evolution.

The solid angle observed (and therefore the number density of the sources) is geometrically defined by the assumed Universe model. The predicted number of sources in a given redshift interval $(z - 0.5 dz, z + 0.5 dz)$ and in a given infrared luminosity interval $(L - 0.5 dL, L + 0.5 dL)$ is given by

$$dN(L, z) = g(z) \phi(L/f(z)) \frac{dV}{dz} dL dz \quad (4.3)$$

where ϕ is the local luminosity function and $f(z)$ and $g(z)$ are respectively the luminosity evolution function and the density evolution function.

The comoving volume is $V = (A/3)D_M^3$, where A is the sky coverage in steradians and D_M is the comoving distance:

$$D_M = \frac{c}{H_0} \int_0^z (\Omega_M(1+z)^3 + \Omega_\Lambda)^{-\frac{1}{2}} dz' \quad (4.4)$$

4.3 The model: number counts and redshift distributions of infrared sources

in a flat Λ cosmology. A concordance cosmology of $H_0 = 75 \text{ km s}^{-1} \text{ Mpc}^{-1}$, $\Omega_M = 0.3$, $\Omega_\Lambda = 0.7$ is assumed.

The luminosity function assumed at $z = 0$ is a power law parametrization of IRAS galaxies. As explained by Sanders et al. (2003), L_{TIR} was calculated using the fluxes of all four IRAS bands (Sanders & Mirabel 1996). The LF was computed using the $1/V_{\text{max}}$ method (Schmidt 1968). The ‘‘double power-law’’ shape of the LF for IRAS bright galaxies is similar to that derived earlier (Soifer et al. 1987), except for improved statistics at both low and high infrared luminosities, plus the decreased influence of the Virgo cluster due to the larger survey area. In the model the best fit power-laws are used, $\phi(L) \propto L^\alpha$, with $\alpha = -0.6$ and $\alpha = -2.2$ below and above $L_{\text{TIR}} \sim 10^{10.5} L_\odot$ respectively (see Sanders et al. 2003, Fig. 12).

Observational evidences demonstrate an evolution for infrared galaxies (see § 4.3.1). The amount of observed star formation shows that a large component of the infrared population has evolved to the present epoch. Possible scenarios are density evolution, where, due to merging/interactions, galaxies were more numerous in the past, or luminosity evolution, where, due to enhanced star formation, galaxies were more luminous in the past. These two schemes of evolution capture in a way that is practical for computational aspects what in principle is a more general evolution of the luminosity function with redshift. In general, some evolution is needed for all populations of active sources (e.g. QSOs, radio galaxies and starburst galaxies) in order to model extragalactic source counts successfully. One of the ways to model luminosity and/or density evolution is using a simple power law. This assumption is motivated by similar evolutionary models at radio and X-ray wavelengths (Boyle et al. 1988; Benn et al. 1993; Condon 1994). Similar evolution has also been observed in optically selected starburst galaxies (Lilly et al. 1996) and in the submillimeter emission from radio loud galaxies observed at $850 \mu\text{m}$ by SCUBA (Archibald et al. 2001).

Our model assumes power law luminosity, $f(z)$, and density, $g(z)$, evolutions. The following functional forms are adopted:

$$f(z) = \begin{cases} (1+z)^{n_1} & (z < z_1) \\ (1+z)^{n_2} & (z \geq z_1) \end{cases} \quad (4.5)$$

$$g(z) = \begin{cases} (1+z)^{m_1} & (z < z_2) \\ (1+z)^{m_2} & (z \geq z_2) \end{cases} \quad (4.6)$$

The algorithm calculates the number of sources predicted in each redshift bin (see Eq. 4.3), introducing a poissonian scattering to the expected value. Then, a value \tilde{L}_{TIR} is associated to each source, by Monte-Carlo extraction, according to the luminosity function calculated for the redshift of the source. \tilde{L}_{TIR} is then split into two parts: the fraction due to AGN contribution (\tilde{L}_{AGN}), calculated following Eq. 4.1, and the remaining part associated to starbursts (\tilde{L}_{SB}). The SED is thus ‘‘built’’ (see § 4.3.2) adding a scaled AGN template (NGC1068) of luminosity \tilde{L}_{AGN} with the starburst template corresponding to \tilde{L}_{SB} , after the application of a scatter in the $L - T$ relation, and scaled to the appropriate luminosity distance. The sources’

4 A backward evolution model for infrared surveys

flux densities in different bands are then calculated by convolving the redshifted SED with the bandpasses of the filters. In this way, we effectively simulate a virtual sky for a given evolution model. For each source, we know not only the flux densities for several bands and the L_{TIR} , but also the temperature of the dust and the $L_{\text{SB}}/L_{\text{AGN}}$ ratio. The latter information, in particular, allows us to follow the co-evolution of starbursts and accretion, exploring photometric indicators to select different populations of infrared sources.

4.4 Results and comparisons with available surveys

Backward evolution models for the infrared spectral range include a significant number of tunable parameters, and using the proper observational constraints to adjust these parameters is the key to the successful use of such models. Traditionally, the first quantities to fit are the total IR/submm background as measured by COBE (CIB), and the number counts at mid-IR to submillimeter wavelengths. With improving identification and follow up of SCUBA, ISO and *Spitzer* sources, redshift distributions of different IR-selected populations become increasingly available as another powerful constraint. We are now about to enter the next level of physical characterization including determination of full rest frame far-IR SEDs, a field that will get a big boost with *Herschel*, and better disentangling the role of star formation and AGN in high redshift infrared galaxies. The model presented here is designed to allow comparison with this new type of constraints on SED and AGN content. By implicitly coupling AGN evolution to infrared galaxy evolution, this model is also amenable to comparison with AGN surveys at other wavelengths, making use of assumptions on AGN SEDs and obscuration.

The most relevant results of the last years are related to surveys carried out by SCUBA and *Spitzer*. Thus, we will compare our results with the data available for these instruments. Hereafter, we will use number counts from Papovich et al. (2004) and Shupe et al. (2008) for the $24\mu\text{m}$ sources, Frayer et al. (2006) for the $70\mu\text{m}$ and $160\mu\text{m}$ sources, Coppin et al. (2006) for the $850\mu\text{m}$ sources. Redshift distributions are from Wuyts et al. (2008) ($24\mu\text{m}$ sources) and Chapman et al. (2005) ($850\mu\text{m}$ sources). Some of the models simulated are also compared with the CIB measurements (Fixsen et al. 1998; Lagache et al. 2000; Renault et al. 2001; Miville-Deschênes et al. 2002; Lagache et al. 2003). All the simulations are run on a field of view of 3 deg^2 , in order to be comparable with the main infrared surveys and sufficiently sample the high luminosity end. The redshift range covered is $0 \leq z \leq 8$. In the plots of the redshift distributions (see Fig. 4.13–Fig. 4.16), the available data have been appropriately scaled in order to be comparable with the simulations.

In order to find the best set of parameters ($n_1, n_2, z_1, m_1, m_2, z_2$) fitting available data we have run simulations on small fields of view, changing slightly each parameter “by hand”. Changing the parameters one by one allows to understand how and how much each parameter influences the final results: we have used this approach to have full control on the simulation and to know the role and the weight of each parameter. An optimization using

4.4 Results and comparisons with available surveys

Table 4.4. Evolution models

Model	Description	n_1	n_2	z_1	m_1	m_2	z_2
M1	SB	3.0	0.0	2.0	1.0	0.0	2.0
M2	SB+AGN	3.0	0.0	2.0	1.0	0.0	2.0
M3	SB+AGN	3.4	-1.0	2.0	1.0	-1.5	1.0
M4	SB+AGN+ $L-T$ evolution	3.4	-1.0	2.0	1.0	-1.5	1.0
M5	SB+“cut” AGN+ $L-T$ evolution	3.4	-1.0	2.0	1.0	-1.5	1.0

a χ^2 minimization would need a large computing power and will be done only in the future, to tune the solution found with the first method. During the optimization process, we have considered differently the several constraints given from current surveys, depending on their reliability: first, we have tried to reproduce the most accurate measurements and only later we have looked after the fit of the less constrained results. For example, SHADES (Coppin et al. 2006) has made accurate measurements of the number counts at $850\mu\text{m}$ down to faint fluxes ($\sim 2\text{mJy}$) and *Spitzer* has provided very sensitive measurements with minimum uncertainties of the number counts at $24\mu\text{m}$, either with observations on large scales (49deg^2 , Shupe et al. 2008) or very deep, up to fluxes $\sim 0.1\text{mJy}$ (Papovich et al. 2004). On the other hand, the redshift distribution of submillimeter galaxies is not well constrained at high z . In fact, the radio-selected sample of Chapman et al. (2005) is biased towards $z \lesssim 3$ because of the radio flux limit, and there are several clues of galaxies at $z \sim 4$ (Valiante et al. 2007; Knudsen et al. 2008). The redshift distribution of $24\mu\text{m}$ sources is obtained mainly by photometric redshifts (Wuyts et al. 2008), with all the uncertainties introduced by the choice of the SED, and the surveys at 70 and $160\mu\text{m}$ (Frayer et al. 2006) are still rather shallow.

Below, we present a summary of the optimization process, showing the main steps followed to obtain the best parameters set $(n_1, n_2, z_1, m_1, m_2, z_2)$. A summary of the parameters for all the models discussed are shown in Tab. 4.4.

4.4.1 Pure starbursts SEDs

As a starting point, we compare the observations with a model considering only the starburst part of the SED, including its scatter in the $L-T$ relation (model M1). The submillimeter galaxies are starburst dominated, so we look for the best parameter set reproducing at least the $850\mu\text{m}$ number counts. We assume a strong evolution in luminosity ($n_1 = 3, n_2 = 0$) and a less strong evolution in density ($m_1 = 1, m_2 = 0$), with $z_1 = z_2 = 2$. The results are shown in Fig. 4.13. The $850\mu\text{m}$ counts are well reproduced. However, all the other counts are underestimated: using this evolutionary model, there is still room to introduce an SED

4 A backward evolution model for infrared surveys

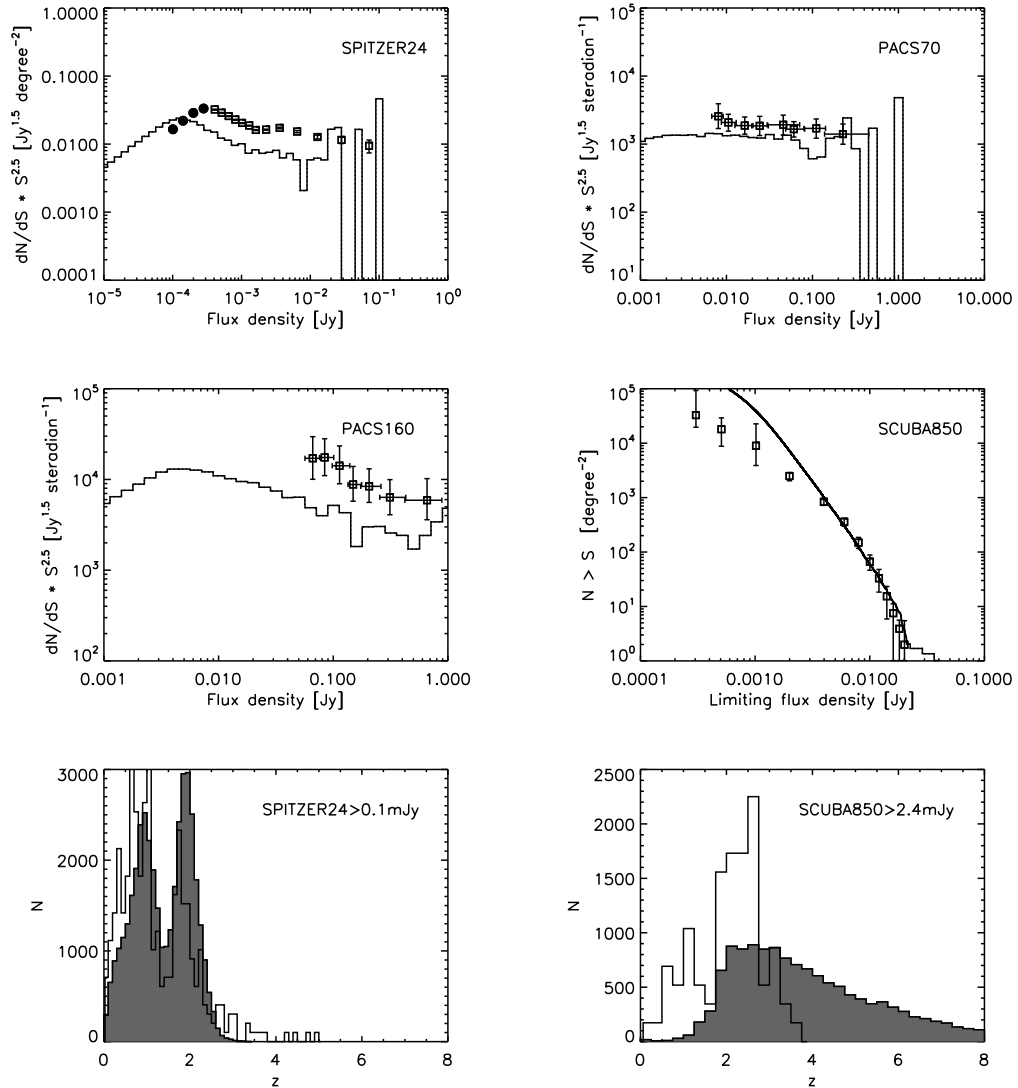


Figure 4.13: Number counts at 24, 70, 160, 850 μm and redshift distributions at 24 and 850 μm , considering evolutions with $n_1 = 3$, $n_2 = 0$, $m_1 = 1$, $m_2 = 0$, $z_1 = z_2 = 2$, without AGN contribution (M1, solid lines). Data are from Papovich et al. (2004) (filled circles) and Shupe et al. (2008) (open squares) for the 24 μm number counts, Frayer et al. (2006) (70 μm and 160 μm counts), Coppin et al. (2006) (850 μm counts), Wuyts et al. (2008) (24 μm redshifts) and Chapman et al. (2005) (850 μm redshifts). Matching the observations references, euclidean normalized differential counts are shown at 24, 70, 160 μm , while integrated counts are shown at 850 μm . Redshifts data (open histograms) have been scaled in order to be comparable with simulations (filled histograms).

4.4 Results and comparisons with available surveys

taking into account also the AGN contribution. The redshift distribution at $24\mu\text{m}$ is quite well reproduced, while at $850\mu\text{m}$ the modeled redshift distribution shows a strong excess at high redshifts. Adding the AGN part, we can be confident that the submillimeter distribution will not change too much, but we should not expect the same trend in the mid-IR, because in that band the AGN contribution can be significant, in particular at high redshifts.

4.4.2 Adding the AGN contribution

In this second step, we build SEDs as described in § 4.3.2. In particular, we determine the AGN contribution following Eq. 4.1. As calculated in § 4.2, we assume a gaussian distribution in each infrared luminosity bin (see Tab. 4.3). Moreover, we assume a luminosity L_* beyond which the contribution of the AGN does not increase any more, but keeps constant with respect to L_{TIR} . Such a value evolves with the redshift: as shown in § 4.2, the contribution of the AGN seems to follow different relations in the local and distant Universe. We take into account this different behavior assuming $\log(L_*/L_\odot) = 12.8$ for $z < 0.5$ and $\log(L_*/L_\odot) = 12.3$ for $z \geq 0.5$. The results, assuming the same evolution applied previously, are shown in Fig. 4.14 (M2). Compared to model M1, the $24\mu\text{m}$ number counts are now better reproduced, even if the shape of the peak is slightly different. The redshift distribution at $24\mu\text{m}$ has become worse: the AGN contribution has introduced a large excess at $z \sim 2$. The parameter set used up to now is no more acceptable and we have to explore the parameter space further, in order to reproduce all the observations.

Comparing different kinds of evolution, we learn that we need a strong luminosity evolution in order to reproduce the number counts at $24\mu\text{m}$ and the $850\mu\text{m}$, but this always introduces an overprediction of the $24\mu\text{m}$ $z \sim 2$ sources. On the other side, with a strong density evolution we obtain a redshift distribution at $24\mu\text{m}$ that is very similar to the observed one, but we completely lose the peak in the $24\mu\text{m}$ number counts. We note, moreover, that a shift of the peak of the density evolution, z_2 , towards lower redshifts, causes a change in the shape of the redshift distribution at $24\mu\text{m}$, reducing the number of the $z \sim 2$ sources, without changing the $24\mu\text{m}$ number counts. Last, if we want to reduce the number of high redshift $850\mu\text{m}$ sources, we need a luminosity evolution peaking at z_1 and then dropping down (n_2 has to be negative). Fig. 4.15 shows number counts and redshift distributions for a model with $n_1 = 3.4$, $n_2 = -1$, $z_1 = 2$, $m_1 = 1$, $m_2 = -1.5$ and $z_2 = 1$ (M3). Data at $24\mu\text{m}$ are well reproduced, in particular the predicted peak of the number counts has now the same shape of the measurements even if it is slightly lower, while at $850\mu\text{m}$ the simulation underpredicts the integral number counts but reproduces the redshift distribution.

In this simulation, the starburst part of the SED still does not vary from the local to the distant universe. This last point is in contradiction to recent works already mentioned in § 4.3.2, showing that submillimeter galaxies, even being as luminous as local “HYLIRGs”, have dust temperatures typical of less luminous local galaxies (ULIRGs) (Chapman et al. 2005; Pope et al. 2006; Valiante et al. 2007). Pope et al. (2006), in particular, needed to modify the “classical” SED model of Chary & Elbaz (2001) increasing the cold component

4 A backward evolution model for infrared surveys

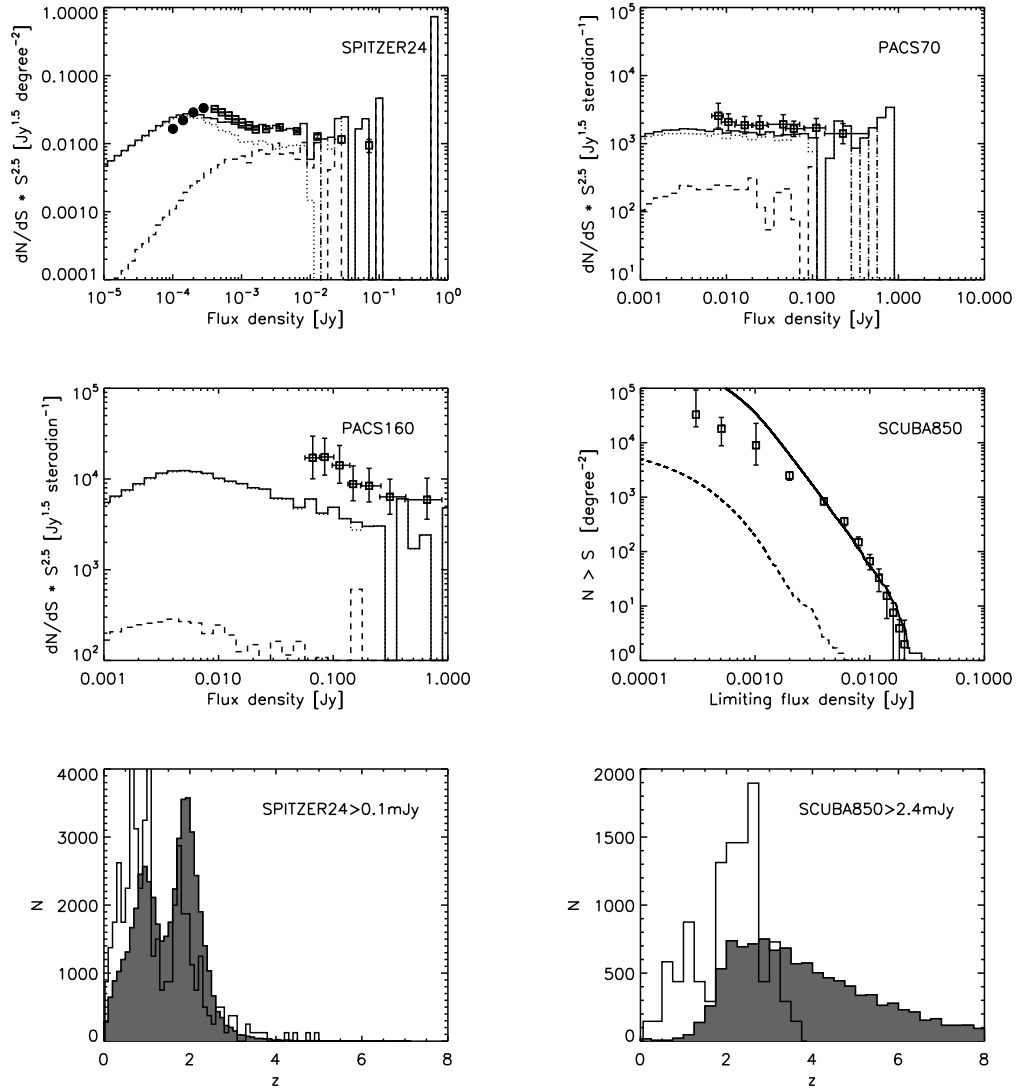


Figure 4.14: Same as Fig. 4.13, but now with AGN contribution (M2). AGN-dominated galaxies ($L_{\text{AGN}}/L_{\text{SB}} \geq 1$) are represented with dashed line, while starburst dominated galaxies ($L_{\text{AGN}}/L_{\text{SB}} < 1$) are in dotted line.

of the dust, in order to fit the SEDs of the submillimeter galaxies in the GOODS-N field.

We then include in our model a simple evolution in the $L - T$ relation. We assume that, at

4.4 Results and comparisons with available surveys

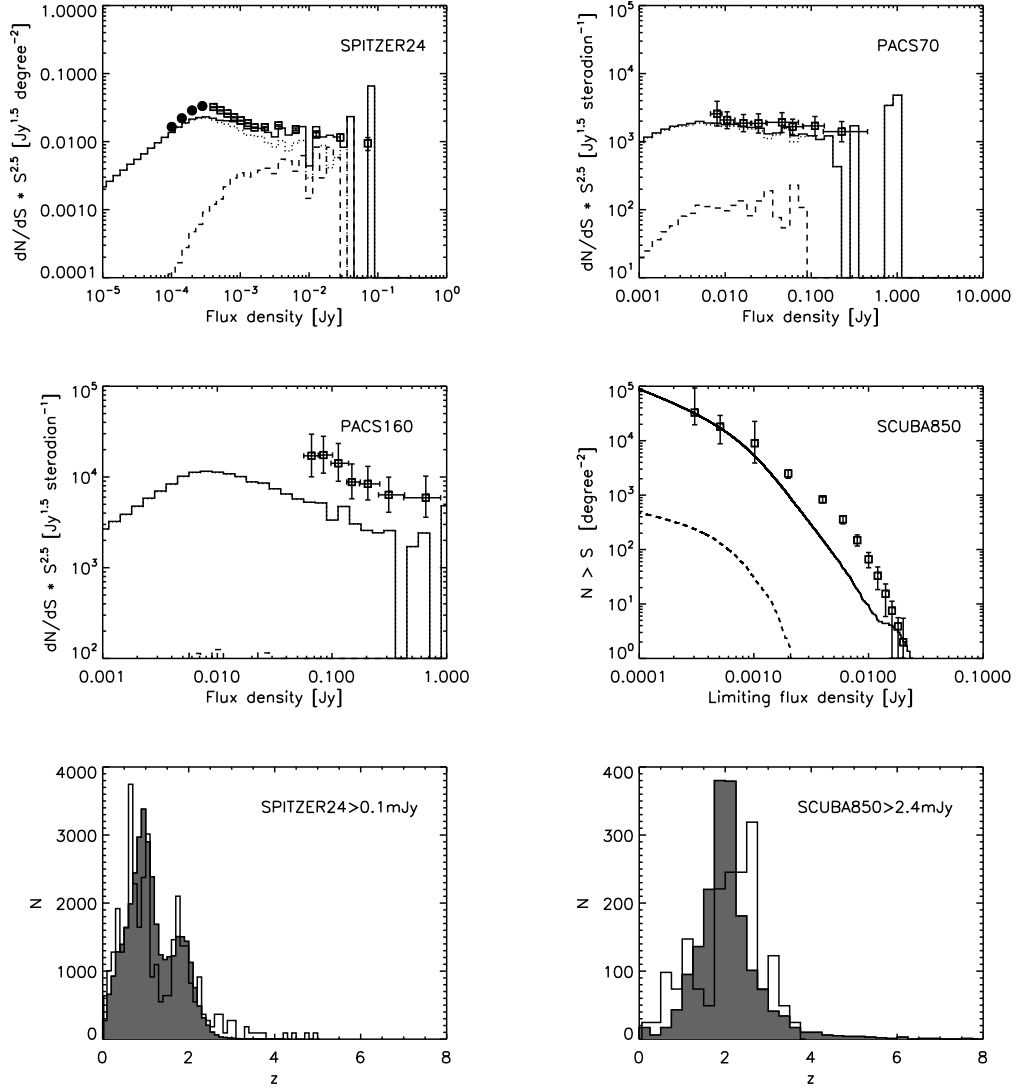


Figure 4.15: Number counts at 24, 70, 160, 850 μm and redshift distributions at 24 and 850 μm , considering evolutions with $n_1 = 3.4$, $n_2 = -1$, $z_1 = 2$, $m_1 = 1$, $m_2 = -1.5$ and $z_2 = 1$, with AGN contribution (M3). Symbols are like in Fig. 4.14. Data are like in Fig. 4.13.

high redshifts ($z \geq 0.5$), Eq. 4.2 is shifted towards colder temperatures:

$$R(60, 100) = C_* \times \left(1 + \frac{10 \times L_*}{L_{\text{TIR}}}\right)^{-\delta} \times \left(1 + \frac{L_{\text{TIR}}}{10 \times L_*}\right)^{\gamma} \quad (4.7)$$

4 A backward evolution model for infrared surveys

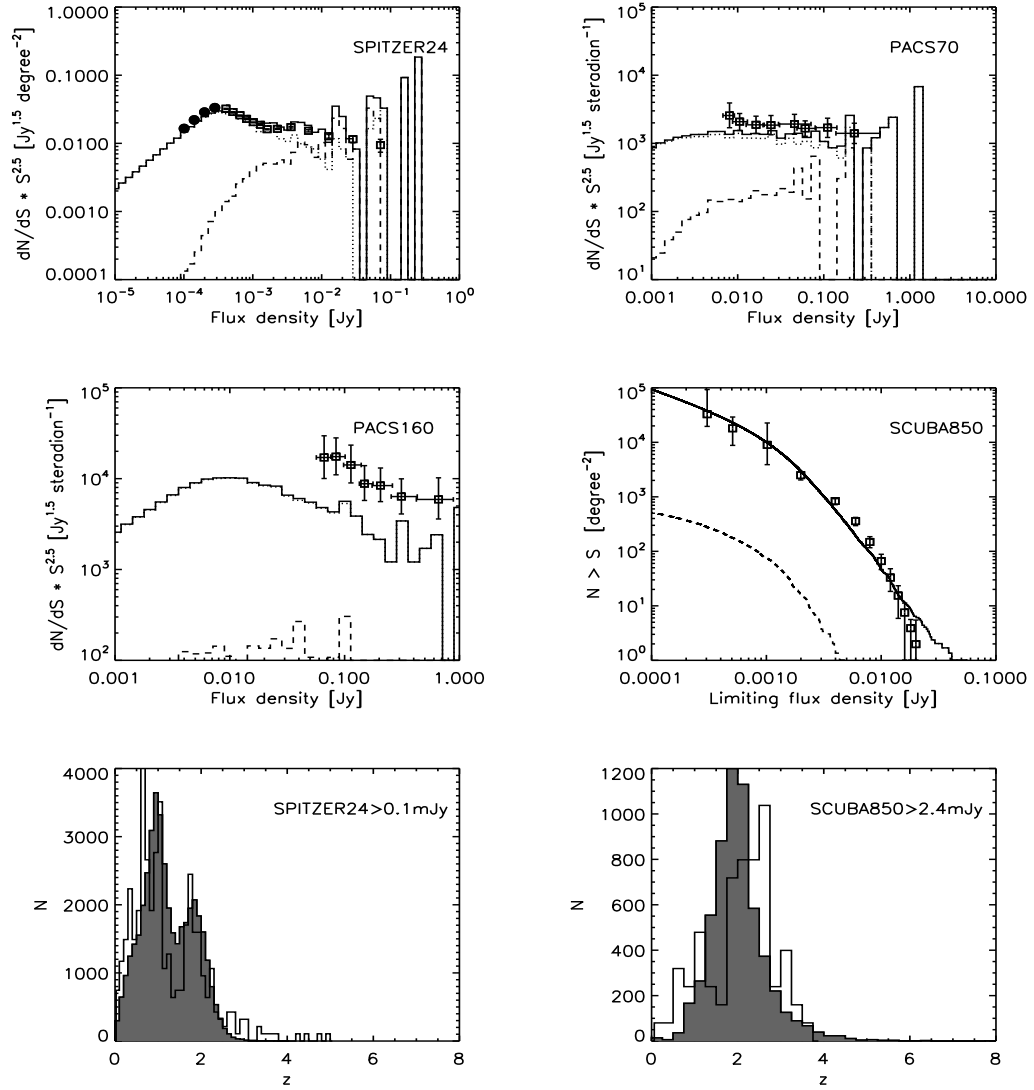


Figure 4.16: Same as Fig. 4.15, assuming an *evolution in the $L - T$ relation (M4)*.

with all the parameters as in Eq. 4.2. This evolution is consistent with the observations cited above. Fig. 4.16 shows number counts and redshift distributions for this new model with $n_1 = 3.4$, $n_2 = -1$, $z_1 = 2$, $m_1 = 1$, $m_2 = -1.5$ and $z_2 = 1$ (M4). All the submillimeter measurements are now well reproduced, with perhaps some excess in the number counts at strong fluxes, together with the mid-IR data, whose number counts have improved and redshift distribution has not felt the effect of the new SEDs.

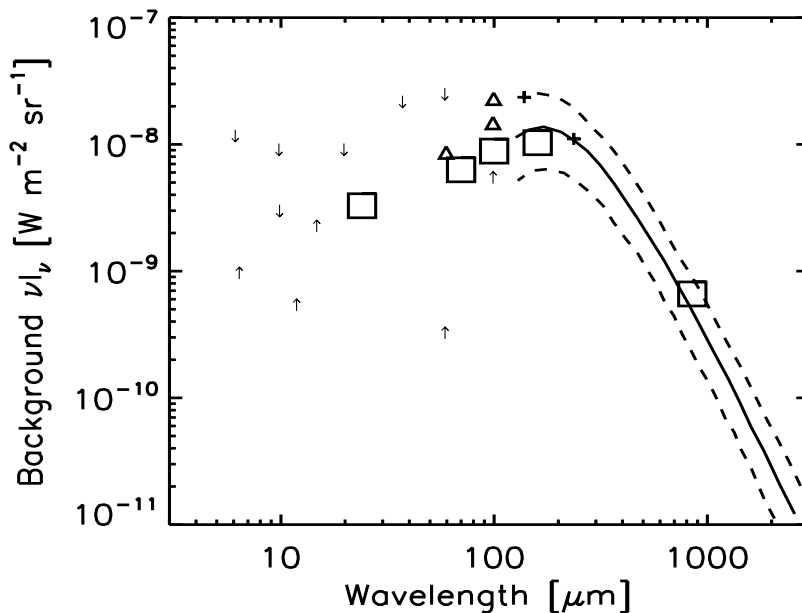


Figure 4.17: Cosmic background from mid-IR to millimeter wavelengths for model M4. The CIB derived from the models at 24, 70, 100, 160 and 850 μm is shown by big open squares. The analytic form of the CIB at the FIRAS wavelengths is from Fixsen et al. (1998) (solid and dashed lines). Measurements are at DIRBE wavebands (140 and 240 μm , plus signs, Lagache et al. 2000), at 100 μm (triangles, Lagache et al. 2000; Renault et al. 2001) and at 60 μm (triangles, Miville-Deschênes et al. 2002). See Lagache et al. (2003) for references about the limits at shorter wavelengths.

Even if the peak of the 24 μm number counts is well reproduced by the model M4, there is still some excess in the number counts at strong fluxes, where AGN dominate, but where the statistic of the predictions is low and the model cannot be very accurate. We compare the number of AGN predicted by our model with the number of sources expected adopting QSO luminosity functions. We select only the brightest 24 μm sources ($f_{24} \geq 5$ mJy) and consider only the AGN-dominated sources ($L_{\text{AGN}}/L_{\text{SB}} \geq 1$). With the exception of some local and faint objects, all the sources selected in this way are highly luminous, distant AGN. Applying a simple bolometric correction, $L_{\text{BOL}} \sim 10V_{\text{L}}$ at mid-IR rest wavelengths, we can calculate the expected number of QSOs for the same L_{BOL} and z ranges of our subsample. We integrate the luminosity function of Hopkins et al. (2007) (“full” model, with pure luminosity evolution and bright- and faint-end slopes evolving with redshift) for $10^{12.2} \leq L_{\text{BOL}} \leq 10^{14.5} L_{\odot}$ and $0.1 \leq z \leq 2.3$. The number of the sources selected from our simulation does not exceed the expected number given by the bolometric luminosity function. Nevertheless, we already

4 A backward evolution model for infrared surveys

pointed out that the high part of the $\nu L_6(\text{AGN})/L_{\text{TIR}}$ distribution is not well constrained (see § 4.2.4). In particular, the hypothesis of the gaussian distribution could be wrong: it was assumed following the principle of the minimization of the free parameters, but a different kind of distribution, for example an asymmetric distribution with a cut-off at high luminosities, cannot be excluded.

As an experiment, in order to reduce the number of luminous AGN, we change the assumed gaussian distribution introducing a cut for large values of $\nu L_{6\mu\text{m}}/L_{\text{TIR}}$: we reject all values of $\nu L_{6\mu\text{m}}/L_{\text{TIR}}$ more than 3σ away from its expected value. The results, again using the same parameters ($n_1 = 3.4$, $n_2 = -1$, $z_1 = 2$, $m_1 = 1$, $m_2 = -1.5$, $z_2 = 1$, model M5), do not change too much with respect to M4, so we do not show them here.

We can consider M4 our best-fit model: all the number counts are well reproduced (within a factor $\lesssim 2$), together with the redshift distributions. There is only one exception: the $160\mu\text{m}$ number counts are largely underestimated. We will discuss this issue in § 4.7.

A further constraint on our evolutionary model comes from the comparison with the current CIB measurements. Our model predictions for the CIB are derived by summing up the flux densities of all sources for the bands in question. Fig 4.17 shows the predicted CIB intensity at specific wavelengths together with the comparison with present observations for the model M4: it agrees with all the available measurements and limits.

4.5 Star formation history

Much attention has been attracted since Madau et al. (1996) related source counts and redshift distributions obtained from deep UV/optical surveys to the star formation/metal production history of the universe. Since then the so-called *Madau diagram* has been revised many times through various improvements, including (1) the corrections for the effect of dust extinction on UV/optical luminosities (e.g. Steidel et al. 1999), (2) results from less extinction-sensitive Balmer line surveys (e.g. Yan et al. 1999), and (3) results from submillimeter SCUBA surveys (e.g. Chapman et al. 2005).

Adopting the conversion factor of Kennicutt (1998),

$$\text{SFR} [\text{M}_\odot \text{yr}^{-1}] = 4.5 \cdot 10^{-44} \times L_{\text{TIR}} [\text{erg s}^{-1}], \quad (4.8)$$

we can convert the cosmic luminosity density evolution of our model to a SFR curve. In the calculation, we take into account only the fraction on infrared luminosity due to star formation (L_{SB}). In Fig. 4.18 the results of the simulation using model M4 are compared with the survey data already shown in Fig. 1.2. The model is in very good agreement with the observations for the full redshift range. In particular, for $z \gtrsim 4$, the model results are similar to the results from SCUBA surveys, while it is slightly lower than the measurements obtained from the UV/optical surveys. This does not surprise, since the model itself is constrained by the infrared/submillimeter data.

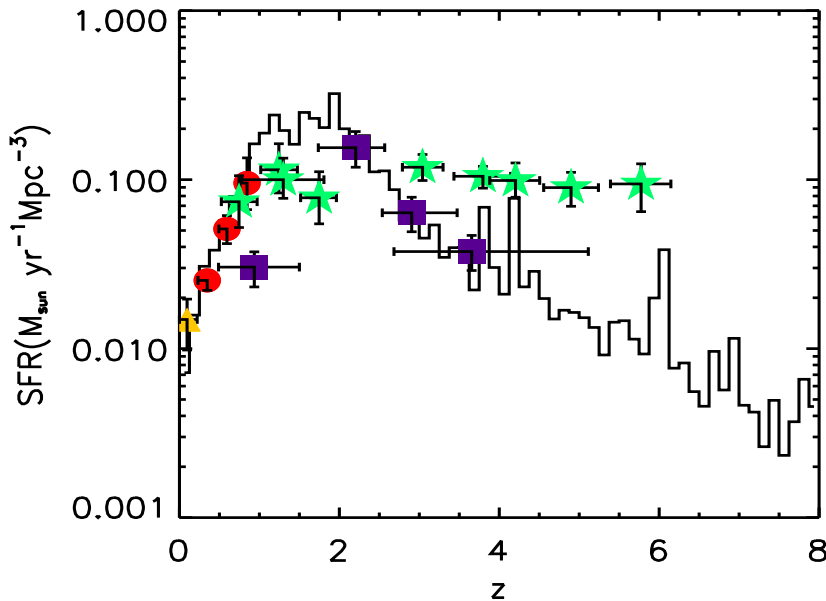


Figure 4.18: Histogram showing the SFR evolution of the model M4 compared with the observational results already shown in Fig. 1.2. *Yellow triangle:* radio surveys; *red circles:* mid-IR surveys; *green stars* UV and optical surveys, corrected for dust extinction; *violet squares:* SMGs corrected for completeness. See Chapman et al. (2005) for a full list of references.

4.6 AGN contribution to infrared emission

As discussed earlier, LIRGs and ULIRGs, with their huge infrared luminosities, correspond to an extremely active phase of dust enshrouded star formation and/or AGN activity. They become an increasingly significant population at high redshift, representing an important phase in the buildup of massive galaxy bulges and in the growth of their central supermassive black holes. To understand these processes, it is essential to separate the contribution of AGN and starburst to the infrared luminosity of LIRGs and ULIRGs.

Recent works have shown how the IRAC color-color diagram and the MIPS 24 to $8\mu\text{m}$ color can be used to identify AGN-dominated sources (Lacy et al. 2004; Sajina et al. 2005; Stern et al. 2005; Yan et al. 2004; Brand et al. 2006). Brand et al. (2006), in particular, have demonstrated how the 24 to $8\mu\text{m}$ flux ratio ($\zeta \equiv \log[vf_{nu}(24\mu\text{m})/vf_{\nu}(8\mu\text{m})]$) can be used to disentangle the contribution of AGN and starbursts to the total reprocessed mid-IR ($\sim 5 - 25\mu\text{m}$) emission as a function of the $24\mu\text{m}$ flux. We use this study as a first example of how to confront our model with observations that constraint the AGN content of high- z

4 A backward evolution model for infrared surveys

sources.

Nevertheless, a photometric study of this type is subject to several caveats. Many broad emission- and absorption-line features are known to be present in the mid-IR spectrum of ULIRGs (e.g. Houck et al. 2005; Yan et al. 2005), and this may affect ζ as function of redshift. For example, at $1.1 \lesssim z \lesssim 1.7$, the $24\mu\text{m}$ observed emission can be strongly attenuated by the silicate absorption feature at $9.7\mu\text{m}$. It is also possible that an AGN could be heavily embedded in large amounts of cooler dust and could remain undetected in the $8\mu\text{m}$ band even though it dominates the bolometric infrared emission. In practice: on one side, the galaxies, which in Brand et al. (2006) are classified as “AGN-dominated”, do host an AGN, but it is not necessary the dominant source powering the infrared emission; on the other side, objects that are known to be dominated by AGN in the mid-IR, like NGC1068, do not present the color ($\zeta \sim 0$) that is considered “typical” for AGN-dominated sources in the Brand et al. (2006) study.

Obtaining mid-IR spectroscopy of complete unbiased $24\mu\text{m}$ selected samples of infrared sources will be important in putting more constraints on the AGN contribution to the total infrared emission and in characterization of the $24\mu\text{m}$ selected population. At the moment, there are three different observing programs with IRS that will be well suited for this task, but no results have been published yet. The *Spitzer* GO-2 program PID 20629 (PI L.Yan) will observe 159 sources from the First Look Survey (FLS) with $f_{24} > 0.9\text{mJy}$ and will estimate the relative frequencies of AGN, starburst and composite systems, thus deriving the true obscured star formation density. The *Spitzer* GO-3 program PID 30431 (PI L.Yan) will extend the previous sample to fainter objects ($0.15 < f_{24} < 0.5\text{mJy}$), thus to higher redshift. The proposed observations, in combination with brighter samples from previous IRS surveys, will allow to trace the evolution of AGN/SB ratio, strength of PAH emission and mid-IR opacities as a function of L_{TIR} and z . Last, the *Spitzer* GO-4 program PID 40539 (PI G.Helou) will obtain IRS spectroscopy of a flux-limited sample of galaxies with $5 < f_{24} < 100\text{mJy}$: this sample bridges the gap between the pre-*Spitzer* objects such as nearby spirals and ULIRGs, and the much fainter and more distant sources pursued in most IRS follow-up work to date.

The models developed in this thesis allows to predict the fraction of AGN-dominated sources as a function of the mid-IR flux. In particular, it is possible to distinguish between sources dominated by AGN at $24\mu\text{m}$ and sources AGN-dominated with respect to the total infrared luminosity. This distinction is important when comparing the results of the simulation with the observations: the information about f_{24} will be useful in comparison with the results from the upcoming IRS observations cited above, while the predictions related to L_{TIR} will be confronted with *Herschel* results.

Fig. 4.19a shows the fraction of all sources whose mid-IR emission is dominated by AGN ($f_{24\text{AGN}}/f_{24\text{SB}} > 1$) as a function of the $24\mu\text{m}$ flux density for model M4 (*solid histogram*) and M5 (*dashed histogram*). The trend and the values obtained are similar to those measured by Brand et al. (2006) (*open squares*), even if the measurements have to be compared carefully for the reasons explained above. Our predictions will be easily compared instead with

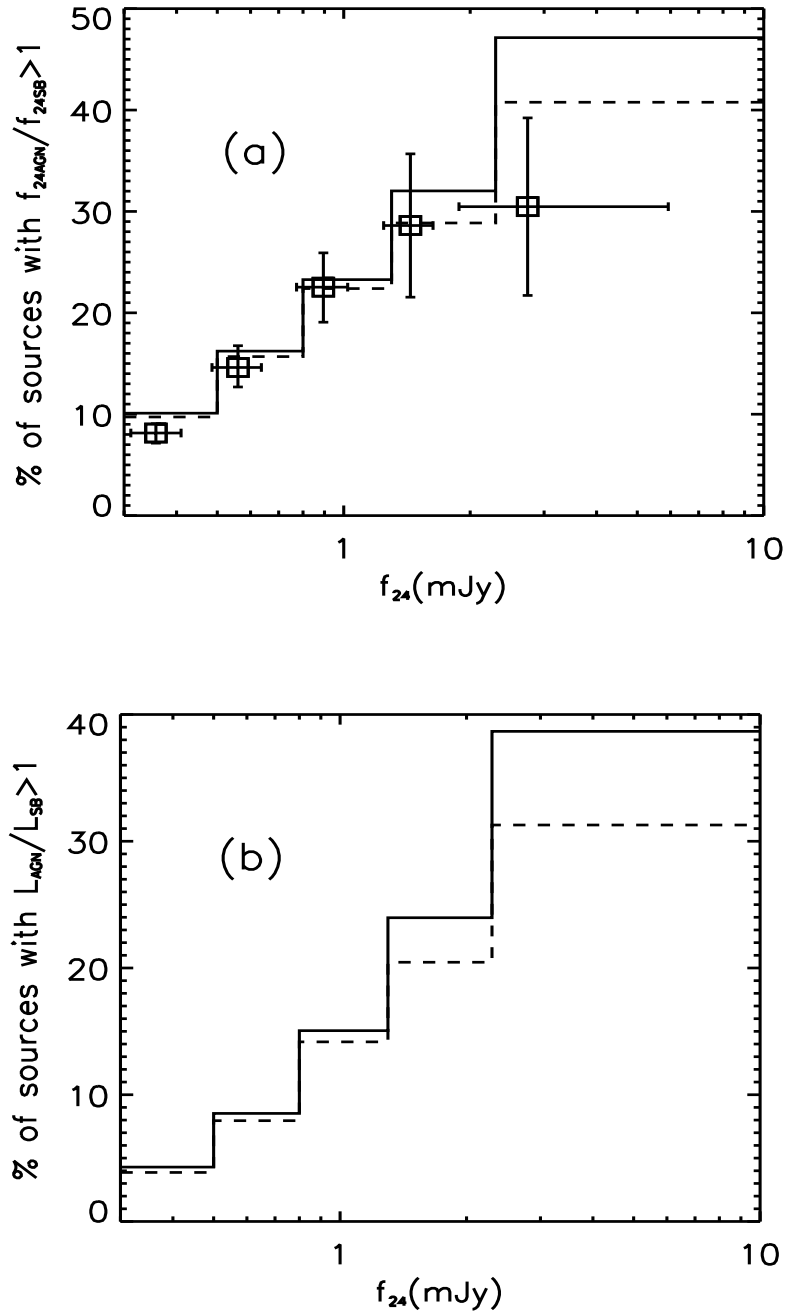


Figure 4.19: Fraction of all sources whose mid-IR emission (a) and total infrared emission (b) are dominated by AGN as a function of f_{24} for model M4 (solid histogram) and M5 (dashed histogram). Redshift range of the sources is $0 \leq z \leq 8$. Open squares represent the results from Brand et al. (2006).

4 A backward evolution model for infrared surveys

the upcoming IRS observations, that will help us to put more constraints on the modeled AGN contribution. In fact, the AGN fraction of model M5, where the AGN contribution has been slightly modified, is a bit lower compared to model M4: only more constraints coming from mid-IR spectroscopic observations can discriminate between the two models M4 and M5. Fig. 4.19b shows the fraction of all sources whose total infrared emission is dominated by AGN ($L_{\text{AGN}}/L_{\text{SB}} > 1$) as a function of the $24\mu\text{m}$ flux density for the two models M4 and M5. As expected, the values of the fraction are lower, because the AGN starts to dominate the mid-IR part of the SED before being dominant in the entire infrared range (see e.g. Fig. 4.12).

4.7 Open issues

Our best-fit model M4 is able to reproduce most of the measurements available. Nevertheless, there are still some issues that need a deeper analysis and discussion and will be dealt with in further studies.

The first point concerns the $160\mu\text{m}$ number counts. None of our models was able to reproduce the number counts at $160\mu\text{m}$, underestimated by a factor of ~ 5 . The ISOPHOT serendipity survey has revealed a population of nearby cold galaxies (Stickel et al. 1998, 2000), under-represented in the $60\mu\text{m}$ IRAS sample. These objects are often associated with bright optical spiral galaxies, and their far-IR colors ($f_{170}/f_{100} \sim 1.3$) indicate a rising spectrum beyond $100\mu\text{m}$, similar to that seen for example in the Milky Way galactic ridge (Serra et al. 1978). Lagache et al. (2003) implemented this class of objects (hereafter “cold galaxies”) in their evolutionary model: cold galaxies dominate the $z = 0$ luminosity function at low luminosities and become less important at higher redshifts, because their evolution is passive and short ($n_1 = 1, n_2 = 0, z_1 = 0.4$). Their contribution to the high luminosity part of the luminosity function is still substantial up to $L_{\text{TIR}} \sim 10^{12} L_{\odot}$, while at larger luminosities it is quite small. Lagache et al. (2003) show that the fraction of cold galaxies can contribute to the total number counts up to $\sim 50\%$ at $170\mu\text{m}$ in the flux range where a comparison with measurements is possible ($0.1 - 1.0\text{mJy}$, see their Fig. 9). The modifications added later to the model have not changed the number counts at $160\mu\text{m}$ (Lagache et al. 2004, their Fig. 4). We can conclude that probably the scatter in the $L - T$ relation calculated by Chapman et al. (2003b) and implemented in our simulations needs some corrections in order to take into account the cold galaxies population. The lack of these corrections can explain why we underestimate the $160\mu\text{m}$ number counts. An important constraint on such a future change of the adopted $L - T$ relation and its scatter will be the $850\mu\text{m}$ counts. The $160\mu\text{m}$ counts need to be increased without creating excess $850\mu\text{m}$ counts. This may support a mostly local change.

The second point regards the excess of bright sources in the $850\mu\text{m}$ number counts. This excess is probably due to the different statistics in the observed and simulated fields. In fact, the simulated field of view is 3deg^2 , 6 times larger than the SHADES field, which the data

4.8 Prediction for multiband Herschel surveys

points refer to. The same model (M4) applied to a smaller field of view (0.5 deg^2 , same as SHADES) reproduces perfectly the observations. Nevertheless, only submillimeter observations on larger scales (SCUBA2 surveys) will be able to constrain the bright end of the distribution.

The third point regards the distribution of the AGN contribution and the fraction of AGN-dominated sources. We already pointed out that the models M4 and M5 predict similar $24\mu\text{m}$ number counts, but different amount of AGN-dominated sources. Galaxies at $z \sim 2$ presenting a “mid-IR excess” have redder $K - 5.8\mu\text{m}$ colors than normal galaxies: this is evidence for an AGN contribution to the mid-IR continuum due to warm dust. The presence of Compton-thick AGN is confirmed by the stacked *Chandra* X-ray data (Daddi et al. 2007). The sky density and the volume density of this population of obscured AGN agree reasonably well with those predicted by the background synthesis models of Gilli et al. (2007). In order to discriminate between our best models, M4 and M5, we need to compare the AGN-dominated sources predicted with upcoming observations with IRS. This will introduce a further constraint, in addition with the bonds already used to the total number counts, and it will make the final model able to reproduce the co-evolution of AGN and starburst in more detail.

4.8 Prediction for multiband Herschel surveys

In this section, we will show predictions using the best-fit model M4. We will concentrate on future surveys with *Herschel*, which will be launched in early 2009, in particular on the PEP survey (see § 1.2.2). All three PACS bands ($70, 100, 160\mu\text{m}$) are considered. Predicted number counts at 70 and $160\mu\text{m}$ are already shown in Fig. 4.16 and compared with the currently available data at those wavebands.

In Fig. 4.20*top* the predicted euclidean normalized differential number counts at $100\mu\text{m}$ are plotted. While at $70\mu\text{m}$ the AGN-dominated sources can give a non-negligible contribution to the total number counts, in particular for $f_{70} \gtrsim 50 \text{ mJy}$, at $100\mu\text{m}$, as well as at $160\mu\text{m}$, the number counts are exclusively dominated by the starburst component.

Fig. 4.20*bottom* shows predicted redshift distributions for the deep ($f_{100} > 1.5 \text{ mJy}$) and large ($f_{160} > 8 \text{ mJy}$) PEP fields. The deep ($10' \times 15'$) and the large ($85' \times 85'$) fields are centered respectively on the GOODS-S and on the COSMOS fields, in order to have the maximum availability of multi-wavelength data and follow up opportunities. The chosen fields are infact fully covered in several of the following: deep X-ray surveys, UV/optical/near-IR/IRAC imaging, HST imaging, *Spitzer* mid-IR surveys, submillimeter surveys and radio mapping. The predicted distributions show a prominent peak at $z \sim 1$ and a secondary bump at $z \sim 2$. Both the surveys will observe sources up to $z \sim 3$, allowing a consistent step forward in the study of the cosmic evolution of dusty star formation and of the infrared luminosity function, as well as in the determination of the overall SEDs of active galaxies.

4 A backward evolution model for infrared surveys

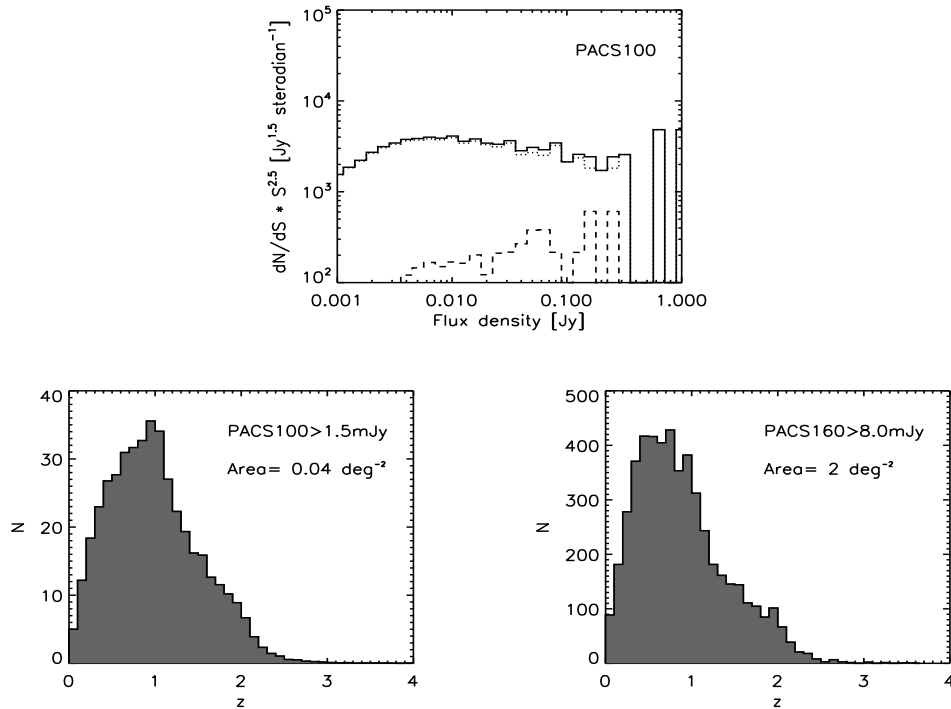


Figure 4.20: Prediction using the best-fit model M4 for the upcoming PEP surveys. *Top:* euclidean normalized differential number counts at $100\mu\text{m}$ (*solid line*). AGN-dominated galaxies ($L_{\text{AGN}}/L_{\text{SB}} \geq 1$) are represented with dashed line, while starburst dominated galaxies ($L_{\text{AGN}}/L_{\text{SB}} < 1$) are shown as dotted line. *Bottom-left:* redshift distributions of PEP survey in the deep field ($10' \times 15'$, $f_{100} > 1.5\text{mJy}$). *Bottom-right:* redshift distributions of PEP survey in the large field ($85' \times 85'$, $f_{160} > 8\text{mJy}$).

4.9 Conclusions

The aim of this work has been to find a “backward evolution” model that can viably fit the galaxy source counts from the mid-IR to submillimeter wavelengths whilst not violating the constraints set by the CIB measurements. SCUBA and *Spitzer* surveys have discovered high redshift sources showing clear differences in their nature: submillimeter sources are mainly starburst-powered (e.g. Tacconi et al. 2006; Valiante et al. 2007), while the brightest $24\mu\text{m}$ sources show typically AGN features both in the mid-IR and in the stacked X-rays spectra (e.g. Yan et al. 2007; Daddi et al. 2007). Are we seeing a representation of two stages of galaxy evolution of the same population or different evolutionary paths of separate populations?

The model developed here has demonstrated that it is possible to reproduce the existing measurements considering only one population of objects, where the contribution between starbursts and AGN varies with the redshifts and the luminosities. Parameterized $(n_1, n_2, z_1, m_1, m_2, z_2)$ luminosity evolution function, $f(z)$, and density evolution function, $g(z)$, are adopted. The best-fit results are $n_1 = 3.4, n_2 = -1, z_1 = 2, m_1 = 1, m_2 = -1.5, z_2 = 1$. The luminosity evolution is mainly constrained by number counts at 24 and 850 μm , while the density evolution is strongly influenced by the 24 μm redshift distribution.

Furthermore, this is the first evolution model using an evolving SED both in the starbursts and in the AGN part. This evolution is needed in order to reproduce simultaneously the number counts in the mid-IR and in the submillimeter and has already been observed in the most recent observations of submillimeter galaxies made with *Spitzer* (Pope et al. 2006; this thesis).

There are still three aspects under analysis. (1) The number counts at 160 μm are not reproduced by our current model. We probably have to implement more cold and local sources, as made by Lagache et al. (2003), changing the spread in the $L - T$ relation calculated by Chapman et al. (2003b). (2) The predicted number counts at 850 μm present too many bright sources. These luminous objects have never been observed, but this is probably due to the small field (0.5 deg^2) of the current submillimeter surveys. (3) The best fit to the data is given by the model M4. Nevertheless, also the model M5, where the AGN contribution is implemented in a slightly different way, is able to reproduce the observations. The difference between the two models is in the fraction of AGN dominated sources as a function of the 24 μm flux density. Only forthcoming mid-IR spectroscopic observations will be able to discriminate between model M4 and M5.

Of course, in order to develop a well constrained model of high redshift SEDs, more measurements at far-IR and submillimeter wavelengths are needed, in particular to characterize the peak of the dust emission at $z \sim 2$. This is exactly one of the main aims of the *Herschel* surveys.

Finally, prediction related to the PEP survey are presented: in two of the three PACS wavebands, the number counts will be dominated by the starburst component. Both the deep and the large fields will observe sources up to $z \sim 3$. PEP will quantify the total energetics of the obscured stages in black-hole evolution, as well as of the star formation, in their phase of maximum activity.

4 A backward evolution model for infrared surveys

5

Conclusions

In this work, we have analyzed and discussed the nature and evolution of infrared high redshift galaxies, both using mid-infrared observations and developing a “backward evolution” model to carry out numerical simulations.

We have presented *Spitzer* mid-infrared spectra of a sample of 13 submillimeter galaxies. For nine of them, we have unambiguous detections of PAH spectral features and/or mid-infrared continua that allow us to constrain energy sources in these objects and to determine, in three cases for the first time, their redshifts. The IRS detections alone have a median $z \sim 2.7$. Plausibly, the four IRS non-detections lie at higher redshifts (≥ 3.6), giving a median $z \sim 2.8$ for the full set of 13. Although our sample is small, this result may indicate an *extension to higher redshift of the SMG redshift distribution* relative to radio-preselected samples with optical redshifts. In the majority of cases, the detection of PAH emission and the weakness of AGN continua indicate that *these galaxies are mainly starburst-powered*. This result agrees with previous X-ray, optical and SED studies that indicate only a small AGN contribution to the infrared luminosity compared to heating from star-formation activity. Our work extends these studies by also constraining the role of highly obscured AGN. The SED properties of our galaxies are in agreement with the *SMGs being scaled-up versions of the compact star-forming regions in local ULIRGs*. The existence of star formation dominated systems at infrared luminosities in excess of $10^{13} L_{\odot}$ is unique to the high redshift universe. The presence of high luminosity starbursts in SMGs may be related to their higher gas fractions (Greve et al. 2005; Tacconi et al. 2006). Mid-infrared spectroscopy with IRS, together with ancillary observations from the optical through radio wavelengths, can play a central role in understanding the nature of submillimeter galaxies and can be a powerful tool for probing the earliest and most dramatic stage of the evolution of galaxies.

5 Conclusions

In order to constrain the AGN contribution to infrared galaxies over a larger range of luminosities than previously, we have applied spectral decomposition techniques to a large sample of *Spitzer* IRS spectra of ULIRGs and LIRGs with $L_{\text{TIR}} > 10^{11} L_{\odot}$ to isolate the AGN $6\mu\text{m}$ continua. The distribution of $\nu L_{6\text{AGN}}/L_{\text{TIR}}$ depends on L_{TIR} . Even if the mean value of the detections does not vary significantly, the number of the detections increases with increasing luminosity, indicating a change in the intrinsic distribution. Monte-Carlo simulations show that *the contribution to the infrared luminosity due to AGN actually increases with the luminosity*. The best fit, $\nu L_{6\mu\text{m}}/L_{\text{TIR}} \propto L_{\text{TIR}}^{\alpha}$, gives $\alpha = 1.4 \pm 0.6$. *The relation does not hold any more at high redshifts.*

We developed a “backward evolution” model that can viably fit the galaxy source counts from the mid-infrared to submillimeter wavelengths whilst not violating the constraints set by the CIB measurements, SCUBA and *Spitzer* surveys. The model developed here reproduces the existing measurements considering only one population of objects, where the contribution between starbursts and AGN varies with the redshifts and the luminosities. Parameterized $(n_1, n_2, z_1, m_1, m_2, z_2)$ luminosity evolution function, $f(z)$, and density evolution function, $g(z)$, are adopted. *This is the first evolution model using an evolving SED both in the starbursts and in the AGN part.* This evolution is necessary in order to reproduce simultaneously the number counts in the mid-infrared and in the submillimeter and has already been observed in the most recent observations of submillimeter galaxies. There are still two aspects under analysis: the number counts at $160\mu\text{m}$ are not reproduced by our current model and the total amount of AGN dominated sources could be not consistent with the Compton-thick sources observed in the mid-infrared.

In order to develop a well constrained model of high redshift SEDs, more measurements at far-infrared and submillimeter wavelengths are needed, in particular to characterize the peak of the dust emission at $z \sim 2$. More measurements at far-infrared will enable a detailed study of the evolution of the infrared luminosity function and luminosity–temperature relation with redshift, expanding on the results based on mid-infrared or submillimeter surveys and suppressing the associated uncertainties due to extrapolation of the infrared SEDs. This is exactly one of the main aims of the *Herschel* surveys.

References

- Adelberger, K.L., Steidel, C.C., Pettini, M., Shapley, A.E., Reddy, N.A., Erb, D.K. 2005, *ApJ*, 619, 697
- Alexander, D.M., et al. 2003, *AJ*, 125, 383
- Alexander, D.M., Smail, I., Bauer, F.E., Chapman, S.C., Blain, A.W., Brandt, W.N., Ivison, R.J. 2005, *Nature*, 434, 738
- Alexander, D.M., Bauer, F.E., Chapman, S.C., Smail, I., Blain, A.W., Brandt, W.N., Ivison, R.J. 2005, *ApJ*, 632, 736
- Archibald, E.N., Dunlop, J.S., Hughes, D.H., Rawlings, S., Eales, S.A., Ivison, R.J. 2001, *MNRAS*, 323, 417
- Aretxaga, I., Hughes, D.H., Chapin, E.L., Gaztañaga, E., Dunlop, J.S., Ivison, R.J. 2003, *MNRAS*, 342, 759
- Aretxaga, I. et al. 2007, *MNRAS*, 379, 1571
- Armus, L., et al. 2007, *ApJ*, 656, 148
- Aussel, H., Cesarsky, C.J., Elbaz, D., Starck, J.L. 1999, *A&A*, 342, 313
- Barger, A.J., Cowie, L.L., Sanders, D.B., Fulton, E., Taniguchi, Y., Sato, Y., Kawara, K., Okuda, H. 1998, *Nature*, 394, 248
- Barger, A.J., Cowie, L.L., Smail, I.R., Ivison, R.J., Blain, A.W., Kneib, J.-P. 1999, *AJ*, 117, 2656
- Baugh, C.M., Benson, A.J., Cole, S., Frenk, C.S., Lacey, C.G. 2003, in *The Mass of Galaxies at Low and High Redshift*, ed. R.Bender & A.Renzini, (New York: Springer), 91
- Baugh, C.M., Lacey, C.G., Frenk, C.S., Granato, G.L., Silva, L., Bressan, A., Benson, A.J., Cole, S. 2005, *MNRAS*, 356, 1191
- Baugh, C.M., 2006, *RPPh*, 69, 3101

References

- Bautz, M.W., Malm, M.R., Baganoff, F.K., Ricker, G.R., Canizares, C.R., Brandt, W.N., Hornschemeier, A.E., Garmire, G.P. 2000, *ApJ*, 543, L119
- Benn, C.R., Rowan-Robinson, M., McMahon, R.G., Broadhurst, T.J., Lawrence, A. 1993, *MNRAS*, 263, 98
- Bergstrom, L. 2000, *RPPh*, 63, 793
- Bertoldi, F., et al. 2000, *A&A*, 360, 92
- Blain, A.W., Smail, I., Ivison, R.J., Kneib, J.-P., Frayer, D.T., 2002, *PhR*, 369, 111
- Blain, A.W., Chapman, S.C., Smail, I., Ivison, R. 2004, *ApJ*, 611, 725
- Blumenthal, G.R., Faber, S.M., Primack, J.R., Rees, M.J. 1984, *Nature*, 311, 517
- Borys, C., Smail, I., Chapman, S.C., Blain, A.W., Alexander, D.M., Ivison, R.J. 2005, *ApJ*, 635, 853
- Boulanger, F., Boissel, P., Cesarsky, D., Ryter, C. 1998, *A&A*, 339, 194
- Bower, R.G., Benson, A.J., Malbon, R., Helly, J.C., Frenk, C.S., Baugh, C.M., Cole, S., Lacey, C.G. 2006, *MNRAS*, 370, 645
- Boyle, N., Shanks, T., Peterson, B.A. 1988, *MNRAS*, 235, 935
- Braito, V. et al. 2004, *A&A*, 420, 79
- Brand, K., et al. 2006, *ApJ*, 644, 143
- Brand, K., et al. 2008, *ApJ*, 673, 119
- Brandl, B.R., et al. 2006, *ApJ*, 653, 1129
- Carilli, C.L., Yun, M.S. 2000, *ApJ*, 530, 618
- Carroll, S.M. 2004, *AIPC*, 743, 16
- Carroll, S.M., Sawicki, I., Silvestri, A., Trodden, M. 2006, *NJPh*, 8, 323
- Chapman, S.C., Blain, A.W., Ivison, R.J., Smail, I.R. 2003, *Nature*, 422, 695
- Chapman, S.C., Helou, G., Lewis, G.F., Dale, D.A. 2003, *ApJ*, 588, 186
- Chapman, S.C., Windhorst, R., Odewahn, S., Yan, H., Conselice, C. 2003, *ApJ*, 599, 92
- Chapman, S.C., Blain, A.W., Smail, I., Ivison, R.J. 2005, *ApJ*, 622, 772
- Charmandaris V., et al. 2004, *ApJS*, 154, 142

- Chary, R., Elbaz, D. 2001, ApJ, 556, 562
- Cimatti A., et al. 2004, Nature, 430, 184
- Colbert, J.W., et al. 1999, ApJ, 511, 721
- Cole, S. et al. 2005, MNRAS, 362, 505
- Colless, M. et al. 2001, MNRAS, 328, 1039
- Condon, J.J 1994, ApJ, 287, 461
- Conselice, C.J., Chapman, S.C., Windhorst, R.A. 2003, ApJ, 596, L5
- Coppin, K., et al. 2006, MNRAS, 372, 1621
- Cowie, L.L., Barger, A., Kneib, J.-P. 2002, AJ, 123, 2197
- Crenshaw D.M., Peterson, B.M., Korista, K.T., Wagner, R.M., Aufdenberg, J.P. 1991, AJ, 101, 1202
- Daddi, E. et al. 2005, ApJ, 631, L13
- Daddi, E., et al. 2007, ApJ, 670, 173
- Dale, D.A., Helou, G., Contursi, A., Silbermann, N.A., Kolhatkar, S. 2001, ApJ, 549, 215
- Dale, D., Helou, G. 2002, ApJ, 576, 159
- Dale, D., et al. 2006, ApJ, 646, 161
- Dannerbauer, H., Lehnert, M.D., Lutz, D., Tacconi, L., Bertoldi, F., Carilli, C., Genzel, R., Menten, K. 2002, ApJ, 573, 473
- Dannerbauer, H., Lehnert, M.D., Lutz, D., Tacconi, L., Bertoldi, F., Carilli, C., Genzel, R., Menten, K. 2004, ApJ, 606, 664
- Dannerbauer, H. 2004, PhD Thesis, Ludwig-Maximilians-Universität München
- Davis, M., Efstathiou, G., Frenk, C.S., White, S.D.M. 1985, ApJ, 292, 371
- de Bernardis, P. et al. 2000, Nature, 404, 955
- Deffayet, C., Dvali, G., Gabadadze, G. 2002, PhR, 65, 4023
- Della Ceca, R., et al. 2002, ApJ, 581, L9
- Desai, V., et al. 2006, ApJ, 641, 133

References

- Desai, V., et al. 2007, *ApJ*, 669, 810
- Downes, D., et al. 1999, *A&A*, 347, 809
- Draine, B.T. 2003, *ARA&A*, 41, 241
- Dunlop, J.S., et al. 2004, *MNRAS*, 350, 769
- Eales, S., Bertoldi, F., Ivison, R., Carilli, C., Dunne, L., Owen, F. 2003, *MNRAS*, 344, 169
- Efstathiou, A., Hough, J.H., Young, S. 1995, *MNRAS*, 277, 1134
- Efstathiou, A., Rowan-Robinson, M., Siebenmorgen, R. 2000, *MNRAS*, 313, 734
- Egami, E., et al. 2004, *ApJS*, 154, 130
- Elbaz, D., Cesarsky, C.J., Chanial, P., Aussel, H., Franceschini, A., Fadda, D., Chary, R.R. 2002, *A&A*, 384, 848
- Ellis, R.S. 1997, *ARA&A*, 35, 389
- Elvis, M., et al. 1994, *ApJS*, 95, 1
- Engelbracht, C.W., Gordon, K.D., Rieke, G.H., Werner M.W., Dale, D.A., Latter, W.B. 2005, *ApJ*, 628, L29
- Farrah, D., Afonso, J., Efstathiou, A., Rowan-Robinson, M., Fox, M., Clements, D. 2003, *MNRAS*, 343, 585
- Ferguson, H.C., Dickinson, M., Williams, R. 2000, *ARA&A*, 38, 667
- Ferrarese, L., Merritt, D. 2000, *ApJ*, 549, 215
- Fixsen, D.J., Dwek, E., Mather, J.C., Bennett, C.L., Shafer, R.A. 1998, *ApJ*, 508, 123
- Förster Schreiber, N., Sauvage, M., Charmandaris, V., Laurent, O., Gallais, P., Mirabel, I.F., Vigroux, L. 2003, *A&A*, 399, 833
- Franceschini, A., Danese, L., de Zotti, G., Xu, C. 1988, *MNRAS*, 233, 175
- Franceschini, A., Andreani, P., Danese, L. 1998, *MNRAS*, 296, 709
- Franceschini, A. et al. 2003, *MNRAS*, 343, 1181
- Frayser, D.T., Ivison, R.J., Scoville, N.Z., Yun, M., Evans, A.S., Smail, I., Blain, A.W., Kneib, J.-P. 1998, *ApJ*, 506, L7
- Frayser, D.T., et al. 1999, *ApJ*, 514, L13

- Frayser, D.T., Smail, I., Ivison, R.J., Scoville, N.Z. 2000, *AJ*, 120, 1668
- Frayser, D.T. et al. 2006, *ApJ*, 131, 250
- Fukugita, M., Hogan, C.J., Peebles, P.J.E. 1998, *ApJ*, 503, 518
- Gebhardt, K., et al. 2000, *ApJ*, 539, L13
- Genzel, R., et al. 1998, *ApJ*, 498, 579
- Genzel, R., Cesarsky, C. 2000, *ARA&A*, 38, 761
- Genzel, R., Baker, A.J., Tacconi, L.J., Lutz, D., Cox, P., Guilloteau, S., Omont, A. 2003, *ApJ*, 584, 633
- Gilli, R., Comastri, A., Hasinger, G., 2007 *A&A*, 463, 79
- Gispert, R., Lagache, G., Puget, J.L. 2000, *A&A*, 360, 1
- Greve, T.R., et al. 2005, *MNRAS*, 359, 1165
- Gruppioni, C., Pozzi, F., Lari, C., Oliver, S., Rodighiero, G. 2005, *ApJ*, 318, 9
- Guiderdoni, B., Hivon, E., Bouchet, F.R., Maffei, B. 1998, *MNRAS*, 295, 877
- Haas, M., Klaas, U., Müller, S.A.H., Chini, R., Coulson, I. 2001, *A&A*, 367, L9
- Hanany, S. et al. 2000, *ApJ*, 545, L5
- Hao, L., et al. 2005, *ApJ*, 625, L75
- Hauser, M.G., Dwek, E. 2001, *ARA&A*, 39, 249
- Helou, G., Soifer, T., Rowan-Robinson, M., 1985, *ApJ*, 298, L7
- Higdon, S.J.U., et al. 2004, *PASP*, 116, 975
- Hinshaw, G. et al. 2003, *ApJS*, 148, 135
- Hinshaw, G. et al. 2007, *ApJS*, 170, 288
- Holland, W., et al. 1999, *MNRAS*, 303, 659
- Hopkins, P.F., Richards, G.T., Hernquist, L. 2007, *ApJ*, 654, 731
- Horst, H., Gandhi, P., Smette, A., Duschl, W.J. 2008, *A&A*, 479, 389
- Houck, J.R., et al. 2004, *ApJS*, 154, 18

References

- Houck, J.R., et al. 2005, *ApJ*, 622, L105
- Hughes, D.H., et al. 1998, *Nature*, 394, 241
- Imanishi, M., Dudley, C.C., Maiolino, R., Maloney, P.R., Nakagawa, T., Risaliti, G. 2007, *ApJS*, 171, 72
- Iverson, R.J., Smail, I., Le Borgne, J.-F., Blain, A.W., Kneib, J.-P., Bézecourt, J., Kerr, T.H., Davies, J.K. 1998, *MNRAS*, 298, 583
- Iverson, R.J., et al. 2002, *MNRAS*, 337, 1
- Iverson, R.J., et al. 2004, *ApJS*, 154, 124
- Iwasawa, K., Sanders, D.B., Evans, A.S., Trentham, N., Miniutti, G., Spoon, H.W.W. 2005, *MNRAS*, 357, 565
- Jarvis, M. J., Rawlings, S., Eales, S., Blundell, K.M., Bunker, A. J., Croft, S., McLure, R.J., Willott, C.J. 2001, *MNRAS*, 326, 1585
- Jones, W.C. et al. 2006, *ApJ*, 647, 823
- Kauffmann, G., Colberg, J.M., Diaferio, A., White, S.D.M. 1999, *MNRAS*, 303, 188
- Kennicutt, R.C. 1998, *ARA&A*, 36, 189
- Kessler, M., et al. 1996, *A&A*, 315, L27
- Klaas, U., et al. 2001, *A&A*, 379, 823
- Knudsen, K.K., Kneib, J.P., Egami, E. 2006, in *Infrared Diagnostic of Galaxy Evolution*, ed. R.Chary, astro-ph/0604073
- Knudsen, K.K., Kneib, J.P., Egami, E. 2008, *ASPC*, 381, 371
- Kovács, A., Chapman, S.C., Dowell, C.D., Blain, A.W., Iverson, R.J., Smail, I., Phillips, T.G. 2006, *ApJ*, 650, 592
- Krabbe, A., Boeker, T., Maiolino, R. 2001, *ApJ*, 557, 626
- Kreysa, E., et al. 1998, *SPIE*, 3357, 319
- Lacy, M., et al. 2004, *ApJS*, 154, 166
- Lagache, G., Puget, J.L. 2000, *A&A*, 355, 17
- Lagache, G., Dole, H., Puget, J.L. 2003, *MNRAS*, 338, 555

- Lagache, G., et al. 2004, *ApJS*, 154, 112
- Lagache G., Puget, J.L., Dole, H. 2005, *ARA&A*, 43, 727
- Laurent, O., Mirabel, I.F., Charmandaris, V., Gallais, P., Madden, S.C., Sauvage, M., Vigroux, L., Cesarsky, C. 2000, *A&A*, 359, 887
- Ledlow, M.J., Smail, I., Owen, F.N., Keel, W.C., Ivison, R.J., Morrison, G.E. 2002, *ApJ*, 577, L79
- Le Floc'h, E. et al. 2005, *ApJ*, 632, 169
- Lilly, S.J., Le Fevre, O., Hammer, F., Crampton, D. 1996, *ApJ*, 460, 1L
- Lilly, S.J., Eales, S.A., Gear, W.K.P., Hammer, F., Le Fèvre, O., Crampton, B., Bond, J.R., Dunne, L. 1999, *ApJ*, 518, 641
- Lutz, D., Spoon, H.W.W, Rigopoulou, D., Moorwood, A.F.M., Genzel, R. 1998, *ApJ*, 505, L103
- Lutz, D., Maiolino, R., Spoon, H.W.W., Moorwood, A.F.M. 2004, *A&A*, 418, 465
- Lutz, D., Valiante, E., Sturm, E., Genzel, R., Tacconi, L.J., Lehnert, M.D., Sternberg, A., Baker, A.J. 2005, *ApJ*, 625, L83
- Lutz, D., Yan, L., Armus, L., Helou, G., Tacconi, L.J., Genzel, R., Baker, A.J. 2005, *ApJ*, 632, L13
- Lutz, D., et al. 2007, *ApJ*, 661, 25L
- Madau, P., Ferguson, H.C., Dickinson, M.E., Giavalisco, M., Steidel, C.C., Fruchter, A. 1996, *MNRAS*, 283, 1388
- Maiolino, R., et al. 2003, *MNRAS*, 344, 59L
- Martínez-Sansigre, A., Rawlings, S., Lacy, M., Fadda, D., Marleau, F.R., Simpson, C., Willott, C.J., Jarvis, M.J. 2005, *Nature*, 436, 666
- Matsuhara, H. et al. 2000, *A&A*, 361, 407
- Menéndez-Delmestre, K., et al. 2007, *ApJ*, 655, 65L
- Miville-Deschênes, M.A., Lagache, G., Puget, J.L. 2002, *A&A*, 393, 749
- Nagashima, M., Lacey, C.G., Baugh, C.M., Frenk, C.S., Cole, S. 2005, *MNRAS*, 358, 1247
- Nagashima, M., Lacey, C.G., Okamoto, T., Baugh, C.M., Frenk, C.S., Cole, S. 2005, *MNRAS*, 363, L31

References

- Nardini, E., Risaliti, G., Salvati, M., Sani, E., Imanishi, M., Marconi, A., Maiolino, R. 2008, MNRAS, 385, 130L
- Neri, R., et al. 2003, ApJ, 597, L113
- Oliver S.J. et al. 2000, MNRAS, 316, 749
- Padmanabhan, N. et al. 2007, MNRAS, 378, 852
- Papovich, C. et al. 2004, ApJS, 154, 70
- Pearson, C.P. & Rowan-Robinson, M. 1996, MNRAS, 283, 174
- Peebles, P.J.E. 1982, ApJ, 263, L1
- Persic, M., Salucci, P. 1992, MNRAS, 258, 14
- Percival, W.J. et al. 2001, MNRAS, 327, 1297
- Percival, W.J. et al. 2007, ApJ, 657, 645
- Pérez-González, P.G. et al. 2005, ApJ, 630, 82
- Perlmutter, S. et al. 1999, ApJ, 517, 565
- Poglitsch, A., et al. 2006, SPIE, 6265, 8
- Pope, A.C., et al. 2004, ApJ, 607, 655
- Pope, A., Borys, C., Scott, D., Conselice, C., Dickinson, M., Mobasher, B. 2005, MNRAS, 358, 149
- Pope, A., et al. 2006, MNRAS, 370, 1185
- Pope, A., et al. 2008, ApJ, 675, 1171
- Ptak, A., Heckman, T., Levenson, N.A., Weaver, K., Strickland, D. 2003, ApJ, 592, 782
- Puget, J.L., Abergel, A., Bernard, J.P., Boulanger, F., Burton, W.B., Desert, F.X., Hartmann, D. 1996, A&A, 308, L5
- Renault, C., Barrau, A., Lagache, G., Puget, J.L. 2001, A&A, 371, 771
- Riess, A.G. et al. 1998, AJ, 116, 1009
- Riess, A.G. et al. 2004, ApJ, 607, 665
- Rigopoulou, D., Spoon, H.W.W., Genzel, R., Lutz, D., Moorwood, A.F.M., Tran, Q.D. 1999, AJ, 118, 2625

- Risaliti, G., Gilli, R., Maiolino, R., Salvati, M. 2000, *A&A*, 357, 13
- Rowan-Robinson, M. 1992, *MNRAS*, 258, 787
- Rowan-Robinson, M. 2001, *ApJ*, 549, 745
- Sajina, A., Lacy, M., Scott, D. 2005, *ApJ*, 621, 256
- Sanchez, A.G., Baugh, C.M., Percival, W.J., Peacock, J.A., Padilla, N., Cole, S., Frenk, C.S., Norberg, P. 2006, *MNRAS*, 366, 189
- Sanders, D.B., Soifer, B.T., Elias, J.H., Madore, B.F., Matthews, K., Neugebauer, G., Scoville, N.Z. 1988, *ApJ*, 325, 74
- Sanders, D.B., Mirabel, I.F. 1996, *ARA&A*, 34, 749
- Sanders, D.B., Mazzarella, J.M., Kim, D.-C., Surace, J.A., Soifer, B.T. 2003, *AJ*, 126, 1607
- Saunders, W., Rowan-Robinson, M., Lawrence, A., Efstathiou, G., Kaiser, N., Ellis, R.S., Frenk, C.S. 1990, *MNRAS*, 242, 318
- Schmidt, M. 1968, *ApJ*, 151, 393
- Schweitzer, M., et al. 2006, *ApJ*, 649, 79
- Serra, G., Puget, J.L., Ryter, C.E., Wijnbergen, J.J. 1978, *ApJ*, 222, 21
- Severgnini, P., Risaliti, G., Marconi, A., Maiolino, R., Salvati, M. 2001, *A&A*, 368, 44
- Shupe, D.L., et al. 2008, *AJ*, 135, 1050
- Siebenmorgen, R., Haas, M., Krügel, E., Schulz, B. 2005, *A&A*, 436, L5
- Smail, I., Ivison, R.J., Blain, A.W. 1997, *ApJ*, 490, L5
- Smail, I., Ivison, R.J., Owen, F.N., Blain, A.W., Kneib, J.-P. 2000, *ApJ*, 528, 612
- Smail, I., Ivison, R.J., Blain, A.W., Kneib, J.-P. 2002, *MNRAS*, 331, 495
- Smail, I., Chapman, S.C., Blain, A.W., Ivison, R.J. 2004, *AJ*, 616, 71
- Smith, J.D.T, et al. 2007, *ApJ*, 656, 770
- Smoot, G.F. et al. 1992, *ApJ*, 396, L1
- Soifer, B.T., Sanders, D.B., Madore, B.F., Neugebauer, G., Danielson, G.E., Elias, J.H., Lonsdale, C.J., Rice, W.L. 1987, *ApJ*, 320, 238
- Spergel, D.N. et al. 2007, *ApJS*, 170, 377

References

- Spoon, H.W.W., Keane, J.V., Tielens, A.G.G.M., Lutz,D., Moorwood, A.F.M. 2001, A&A, 365, L353
- Spoon, H.W.W., et al. 2004, ApJS, 154, 184
- Stern, D., et al. 2005, ApJ, 631, 163
- Steidel, C.C., Giavalisco, M., Pettini, M., Dickinson, M., Adelberger, K.L. 1996, ApJ, 492, L17
- Steidel, C.C., Adelberger, K.L., Giavalisco, Dickinson, M., M., Pettini, M. 1999, ApJ, 519, 1
- Stickel, M., et al. 1998, A&A, 336, 116
- Stickel, M., et al. 2000, A&A, 359, 865
- Sturm, E., Lutz, D., Tran, D., Feuchtgruber, H., Genzel, R., Kunze, D., Moorwood, A.F.M., Thornley, M.D. 2000, A&A, 358, 481
- Sturm, E., et al. 2005, ApJ, 629, L21
- Swinbank, A.M., Smail, I., Chapman, S.C., Blain, A.W., Ivison, R.J., Keel, W.C. 2004, ApJ, 617, 64
- Tacconi, L.J., et al. 2006, ApJ, 640, 228
- Tacconi, L.J., et al. 2008, ApJ, 680, 246
- Takeuchi, T.T., Ishii, T.T., Hirashita, H., Yoshikawa, K., Matsuhara, H., Kawara, K., Okuda, H. 2001, PASJ, 53, 37
- Tecza, M., et al. 2004, ApJ, 605, L109
- Tegmark, M. et al. 2004, ApJ, 606, 702
- Tegmark, M. et al. 2006, PhRD, 74, 12, 123507
- Teng, Stacy H., Wilson, A.S., Veilleux, S., Young, A.J., Sanders, D.B., Nagar, N.M. 2005, ApJ, 633, 664
- Teplitz, H.I., et al. 2005, AAS, 207, #52.08
- Thomas, D., Maraston, C., Bender, R., Mendes de Oliveria, C. 2005, ApJ, 621, 673
- Tran, Q.D., et al. 2001, ApJ, 552, 527
- Tremaine, S. et al. 2002, ApJ, 574, 740

- Tremonti, C.A. et al. 2004, ApJ, 613, 898
- Valiante, E., Lutz, D., Sturm, E., Genzel, R., Tacconi, L.J., Lehnert, A., Baker, A.J. 2007, ApJ, 660, 1060
- Veilleux, S., Kim, D.-C., Sanders, D.B. 1999, ApJ, 522, 113
- Voss, H., Bertoldi, F., Carilli, C., Owen, F., Lutz, D., Holdaway, M., Ledlow, M., Menten, K. 2006, A&A, 448, 823
- Weedman, D.W., et al. 2005, ApJ, 633, 706
- Weedman, D.W., Le Floch, E., Higdon, S.J.U., Higdon, J.L., Houck, J.R. 2006, ApJ, 638, 613
- Werner, M.W. et al. 2004, ApJS, 154, 1
- Williams, R.E. et al. 1996, AJ, 112, 1335
- Wuyts, S., Labbe, I., Förster Schreiber, N.M., Franx, M., Rudnick, G., Brammer, G.B., van Dokkum, P.G. 2008, ApJ, 682, 985
- Xu, C. et al. 1998, ApJ, 508, 576
- Xu, C. 2000, ApJ, 541, 134
- Xu, C., Lonsdale, C.J., Shupe, D.L., O'Linger, J., Masci, F. 2001, ApJ, 562, 179
- Yan, L., McCarthy, P.J., Freudling, W., Teplitz, H.I., Malumuth, E.M., Weymann, R.J., Malkan, M.A. 1999, ApJ, 519, L47
- Yan L. et al. 2004, ApJS, 154, 60
- Yan, L., et al. 2005, ApJ, 628, 604
- Yan, L., et al. 2007, ApJ, 658, 778
- York, D. et al. 2000, AJ, 120, 1579

References

Curriculum vitae

First name: Elisabetta
Last name: Valiante
Born: Giulianova(TE)-Italy, on February 7th 1980
Citizenship: Italian
E-mail: valiante@mpe.mpg.de

Education

Sept.2004 - to date	PhD at MPE Thesis Title: “High-redshift infrared galaxies: mid-IR properties and evolutionary models”	Garching, Germany
Sept.1998 - Sept.2003 25 Sept.2003	Universita’ “La Sapienza” Graduated in Physics with distinction (110/110) Thesis Title: “The OLIMPO Experiment: design of cryogenic optics”	Rome, Italy
Sept.1993 - July 1998 14 July 1998	Liceo Scientifico “A.Einstein” Graduated with distinction (57/60)	Teramo, Italy

Conferences and Schools

9-11 July 2007	From IRAS to Herschel/Planck: Cosmology from Infrared to Submm Surveys	London, England
24-29 March 2007	The Origin of Galaxies: Exploring Galaxy Evolution with new Generation of Infrared-Millimeter Facilities	Obergurgl, Austria
12-14 April 2006	Francesco Melchiorri - Memorial Conference	Rome, Italy
9-13 October 2006	At the Edge of the Universe: latest results from the deepest astronomical surveys	Sintra, Portugal
19-28 July 2005	Dark Energy and Dark Matter in the Universe - Summer School	Alpbach, Austria
Sept.2004 - to date	IMPRS - International Max Planck Research School on Astrophysics	Garching, Germany

Publications

Lutz, D. et al. 2008, ApJ, accepted (arXiv:0805.2669)

Lutz, D., et al. 2007, ApJ, 661, 25L

Valiante, E., et al. 2007, ApJ, 660, 1060

Fassbender, R., et al. 2006, SPIE, 6266, 90

Masi, S., et al. 2005, ESASP, 590, 581

Lutz, D., et al. 2005, ApJ, 625, 83L

Masi, S., et al. 2003, ESASP, 530, 557

Languages: English(fluent), Italian(native), German(basic)

Technical experience

- Extended experience with SMART and SPICE, the data reduction and analysis softwares for IRS-*Spitzer* data
- Use of ZEMAX, a software for optical system design
- Use of Auto-CAD, a CAD software application for 2D and 3D design and drafting
- Knowledge of IDL, Java, VisualBasic, XML, SQL